UC Berkeley

UC Berkeley Electronic Theses and Dissertations

Title

Multiscale Biophysical Dynamics of Integrin Mechanosensing and Cell Adhesion in silico

Permalink

https://escholarship.org/uc/item/2v6761bd

Author

Montes, Andre

Publication Date

2024

Peer reviewed|Thesis/dissertation

Multiscale Biophysical Dynamics of Integrin Mechanosensing and Cell Adhesion in silico

By

Andre Montes

A dissertation submitted in partial satisfaction of the

requirements for the degree of

Doctor of Philosophy

in

Engineering-Mechanical Engineering

in the

Graduate Division

of the

University of California, Berkeley

Committee in charge:

Professor Mohammad R.K. Mofrad, Co-chair
Professor Grace D. O'Connell, Co-chair
Professor Kevin E. Healy
Professor Tarek I. Zohdi

Spring 2024

Abstract

Multiscale Biophysical Dynamics of Integrin Mechanosensing and Cell Adhesion in silico

by

Andre Montes

Doctor of Philosophy in Engineering-Mechanical Engineering

University of California, Berkeley

Professor Mohammad R.K. Mofrad, Co-chair

Professor Grace D. O'Connell, Co-chair

Cells intricately sense mechanical forces from their surroundings, driving biophysical and biochemical activities. This phenomenon, known as mechanosensing, can occur at the cell-matrix interface. Here, mechanical forces resulting from cellular motion, such as migration or matrix stretching, are exchanged in part by the integrin receptor and its ligand, fibronectin. Upregulation of the $\alpha_5\beta_1$ integrin-fibronectin bond is associated with uncontrolled cell metastasis. Therefore, the molecular mechanisms of this bond are of interest to control cell behavior and limit cancer cell spreading. This bond operates through catch bond dynamics, wherein the bond lifetime paradoxically increases with greater force. However, the mechanism sustaining the characteristic catch bond dynamics of the integrin-fibronectin bond remains unclear. The work presented here leveraged multiscale biophysical simulations to uncover the molecular mechanisms underpinning integrin-fibronectin's catch bond dynamics in the context of cell adhesion. This study integrated molecular dynamics simulations and finite element models to propose that fibronectin sites reinforce cell adhesion through enhanced binding properties and a mechanosensitive mechanism. This work sheds light on the mechanosensitive nature of cell-matrix interactions while contributing to our understanding of multiscale cellular behaviors in physiological and pathological environments.

To all those invisible forces that guide our lives

Contents

List of Figures

List of Tables

Acknowledgments

"How lucky I am to have something that makes saying goodbye so hard"
- The Internet says it's by Winnie the Pooh (A.A. Milne), but I also can't find reliable source material!

Chapter 1

Introduction

1.1 Biophysical Cell Dynamics in Cancer

A range of physiological processes and human diseases rely on the dynamics of biological cells. One critical case is cancer, which causes 690K deaths per year in the US [2] and an estimated 9.9M deaths per year worldwide [40]. Cancerous tumors have consistently been shown to undergo biophysical alterations that promote cancer cell survival, spread, and metastasis [124]. As a collection of cancer cells begin to form a tumor, solid stresses are generated due to tumor growth [119]. In parallel, a network of proteins and molecules that surround the cell known as the extracellular matrix (ECM), stiffens [106]. ECM fibers, which were originally randomly assorted, become aligned to promote highly directional and expedited cancer cell invasion [39, 45]. During metastasis, malignant cancer cells break from their primary tumor, then migrate along through the aligned ECM fibers and across the dense, protein-rich basement membrane [124, 119, 53, 43]. Cancer cells can subsequently wedge between endothelial cells during intravasation, penetrate a blood vessel's wall, and circulate the body [124, 53, 43]. The cancer cell can attach to the endothelium at a downstream capillary, exit the blood vessel after extravasation, then establish itself in a new tumor site and promote the growth of new blood vessels to feed itself [124, 99]. Throughout the metastatic cascade, cells in the cancer milieu sense and exert forces as they traverse, and even remodel, microenvironments with diverse biophysical properties [124].

1.2 Cell-Matrix Adhesion as a Target for Cancer

One proposed idea to impede metastasis has been to target cell-matrix adhesions, the macromolecular entities that adhere the cell and the ECM [56]. Cell-matrix adhesions are assembled during mesenchymal migration and help tether the cell to its outside environment [11]. This adhesive contact transmits and triggers biophysical and biochemical signals across the membrane [53]. The formation of cell-matrix adhesions can be initiated through the activation of integrin. Integrins are heterodimers [104, 53], meaning that they are formed

by the dimerization of two distinct polypeptide chains. In mammals, there are 24 known combinations of noncovalently bonded α (18 types) and β (8 types) subunits [53], serving often similar, yet at times distinct cell-matrix functions and signaling. Regardless, integrins are receptors that can bind to proteins inside the cell (cytoplasmic) and outside the cell (extracellular). Due to its characteristic bidirectional binding property, integrin can transmit signals from the cytoplasmic end to the extracellular end (inside-out signaling) or vice versa (outside-in signaling) [90, 53]. An example of inside-out signaling is the binding of the cytoplasmic protein talin to integrin's tail domain. Upon binding, the tails of integrin separate and integrin's conformation transitions from a bent, low-affinity state to an extended, high-affinity state [71, 120]. The extended state of integrin more readily binds to ECM proteins than the bent state due to the extended state's heightened binding affinity [71, 120]. Alternatively, an example of outside-in signaling is when an ECM ligand such as collagen, fibronetin, or vitronectin binds to integrin and facilitates an aggregation of cytoskeletal components to bolster resistance to extracellular tension [58]. In whichever way integrin achieves binding, once integrin is bound to its corresponding ECM ligand, force can be transduced through integrin due to matrix stretching or cell contraction. Subsequently, more integrins are recruited alongside adaptor proteins like paxillin, α-actinin, vinculin, and kindlin to further anchor the cell [50]. Through a complex cytoplasmic signaling, integrins group together to resist contractile forces imposed by the cytoskeleton or the ECM. As integrin clusters grow to micrometer-size assemblies, they become known as focal adhesions [50].

While many integrins can form focal adhesions, two subtypes have historically garnered some interest to target cancer, $\alpha_V\beta_3$ and $\alpha_5\beta_1$ due to their increased expression during metastasis. Although both integrin subtypes can form focal adhesions, only $\alpha_5\beta_1$ has been demonstrated to develop into fibrillar adhesions, which are key in shaping the ECM around a tumor [87, 49]. Fibroblasts in normal tissue deposit fibronectin (FN) via fibrillar adhesions in a randomized manner. However, fibroblasts in a tumor microenvironment, which are termed cancer-associated fibroblasts, use $\alpha_5\beta_1$ integrins within fibrillar adhesions to deposit FN in an aligned pattern (Fig. 1.1). The increased fiber organization stiffens the ECM and hastens the migration speed of accompanying cancer cells. In essence, cancer-associated fibroblasts, pave the way for expedited cancer cell migration via $\alpha_5\beta_1$ integrin-mediated fibrillar adhesions. On the other hand, $\alpha_V\beta_3$ integrin has been proven to be involved in tumor angiogenesis (i.e., the creation of new blood vessels), promoting nutrient transport to the tumor. Therefore, both $\alpha_V\beta_3$ and $\alpha_5\beta_1$ are well-positioned as therapeutic targets for cancer.

While inhibitors of $\alpha_V\beta_3$ and $\alpha_5\beta_1$ integrins have shown promising results in the wet lab setting for treating cancer, the clinical outcomes have so far failed to demonstrate efficacy. For example, cilengitide (Merck KGaA), which inhibits both $\alpha_V\beta_3$ and $\alpha_5\beta_1$, has been tested in 30 clinical trials [120]. While treatment has consistently been shown to be safe, there has been little to no improvement in patient outcomes. Reasons for the lack of efficacy have been surmised. These include redundant and compensatory mechanisms that still allow for tumor growth and metastasis, or off-target effects. Therefore, the interest in integrin inhibitors as an anti-cancer therapy has slowly diminished. Nevertheless, close to 30 clinical trials assessing integrin targeting treatments in various cancers are currently recruiting or active as of 2024

[clinicaltrials.gov]. In a broader biological context, integrins not only aid in the migration of cancer cells as mentioned, but also contribute to the migration of fibroblasts in connective tissues [101], chondrocytes in cartilage [74], and even T-cells in our immune system when they are in confined spaces [18]. Therefore, integrins have remained a promising protein to study in the hopes of addressing myriad diseases in addition to cancer.
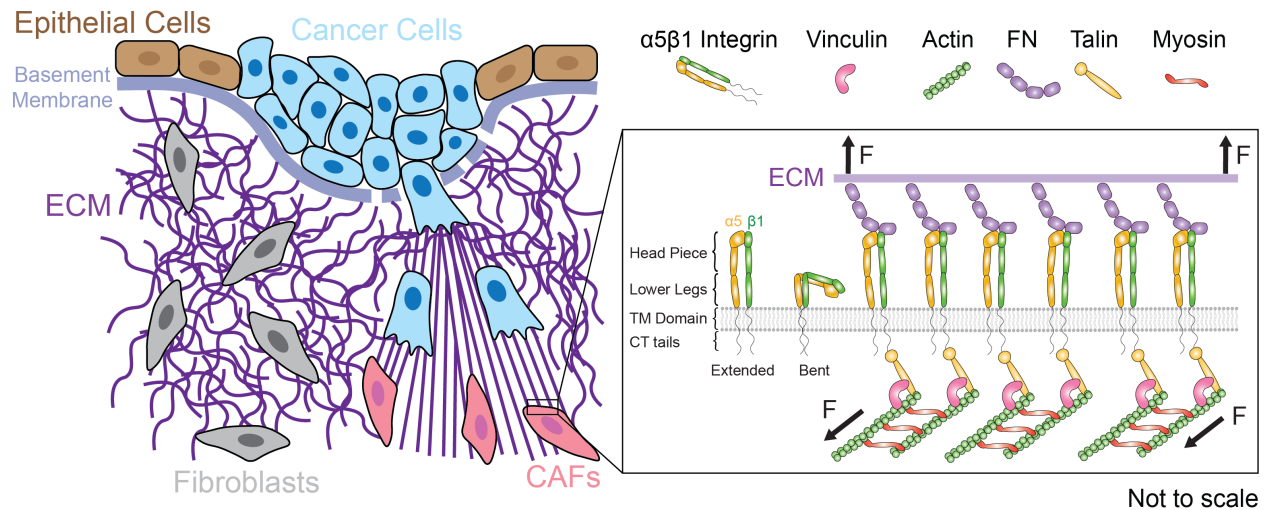
Figure 1.1: Left: Cancer cells initially grouped in a small tumor in the epithelium break through the basement membrane and migrate through the ECM along aligned fibers deposited by cancer-associated fibroblasts (CAFs). Normal fibroblasts deposit cell in a randomized assortment. Inset: Simplified schematic of the initial formation of a focal adhesion. $\alpha_5\beta_1$ integrins along the cell membrane can found in extended and bent states. Integrins span across the cell membrane and are anchored by various cytoplasmic proteins. Force can be transmitted through the macromolecular group due to cell contraction or matrix stretching. TM: Transmembrane. CT: Cytoplasmic. F: Force.

1.3 Integrin Mechanosensing in Cell Adhesion

As well-studied as integrins have been in biological and clinical research fields, there remains many open questions regarding the biophysics of integrin, which may prove fruitful for drug discovery. Integrins sense and resist mechanical forces as cells engage with and move through the ECM. These mechanical forces translate into biochemical actions. The translation from a mechanical force to a biochemical effect is termed mechanotransduction; and the ability to *sense* a mechanical force is coined *mechanosensing*. As discussed, the degree of force at integrin directly influences integrin engagement, focal adhesion maturation, and fibrillar

adhesion activation. How integrin precisely senses force has been of noteworthy interest since revealing this mechanism could prove necessary for finely tailoring drug candidates or designing novel biomaterials with tunable cell dynamics.

This dissertation studies the interaction between $\alpha_5\beta_1$ integrin and it's binding partner, FN because modulating this bond may be useful for concurrently inhibiting cancer cell migration and tuning ECM remodeling. In situ measurements using techniques such as atomic force microscropy (AFM), traction force microscopy, and fluorescence resonance energy transfer (FRET) have quantified $\alpha_5\beta_1$ integrin's mechanosensitivity. $\alpha_5\beta_1$-FN integrin rupture forces have been measured up to around 39-57pN in cells [69, 140] and between 69-120pN when isolated in vitro [78]. Though, cells in a gel environment actively withstand between 1-7pN [128, 20]. In these experiments, binding between integrin and FN is key. The RGD (arginine-glycine-aspartic acid) and synergy site binding domains can be alternatively or mutually targeted via FN or a synthetic peptide. RGD binding alone is sufficient to create a bond, though synergy site binding is essential for $\alpha_5\beta_1$ integrin's peculiar *catch bond* behavior [44]. In a catch bond, the bond lifetime increases with respect to increasing forces, contrary to most bonds that decrease in lifetime with rising forces. It is hypothesized that the catch bond dynamics of $\alpha_5\beta_1$ integrin are essential for the assembly of focal adhesion since severing the catch bond via a synergy site mutation at FN decreases cell adhesion strength. However, the exact mechanism that gives rise to $\alpha_5\beta_1$ integrin's catch bond dynamics remains elusive.

One clue that may provide insight into $\alpha_5\beta_1$ integrin's unique FN-binding dynamics and its role in maintaining cell adhesion stability is its biochemical structure. Cryogenic Electron Microscopy (cryo-EM) has been used to determine the atomic-level structure of $\alpha_5\beta_1$ integrin and propose how it may bind to FN [127, 116]. Cryo-EM has estimated that $\alpha_5\beta_1$ integrin is composed of a head piece, the lower legs, a transmembrane domain, and cytoplasmic tail (Fig. 1.1: inset) [116]. Binding to FN occurs at the head piece, with the RGD domain on FN positioning itself into a pocket between the α_5 and β_1 heads and the synergy site binding to the α_5 head. Using cryo-EM, Schumacher et al. found that the activation of $\alpha_5\beta_1$ may follow a distinct path from other integrins like $\alpha_V\beta_3$ [116]. Specifically, FN can bind to integrin when integrin is in a half-bent conformation, provided that the integrin is primed by manganese ions [116, 127]. This is contrary to the model of $\alpha_V\beta_3$ activation, where an open, extended conformation precedes binding [116]. How these binding modalities and conformational changes facilitate integrin activation, focal adhesion maturation, and cell adhesion remains unclear. Cryo-EM has proven effective at elucidating key structural components of proteins, including $\alpha_5\beta_1$ integrin, at close to 0.3nm resolutions. However, to achieve the atomic level of detail, samples must be flash frozen, meaning that the high-resolution dynamics cannot be visualized experimentally. Therefore, molecular dynamics (MD) simulations are a useful modeling technique for overcoming this barrier and gaining potential insights into the hidden mechanisms of integrin dynamics at the atomic scale, especially when subjected to external forces.

1.4   MD Simulations to Study Integrin Mechanosensing

MD simulations use basic physics principles to model complex atomistic interactions. Many academic resources describe and develop the fundamentals of MD [15, 3, 42, 75]. Here, we provide a brief primer to build an intuition for the fundamental process behind MD.

For an all-atom system, each atom is characterized as a particle within a Cartesian coordinate system. Each particle i has a position vector $\mathbf{r}_i$. For a system with N particles, $i = 1, 2, \cdots N$. Atoms that are adjacent to i as denoted as $\mathbf{r}_j$, $j \neq i$. We can use Newtonian mechanics to describe the motion of the system:

$$m_i \frac{\partial^2 \mathbf{r}_i}{\partial t^2} = \mathbf{F}_i, \quad i = 1, 2, \cdots N, \tag{1.1}$$

where m_i is the mass of particle i, $\mathbf{F}_i$ is the force on particle i from adjacent particles $j = 1, 2, \cdots \neq i, N$. The forces between neighboring atoms due to bonded and non-bonded interactions are modeled by a force field, V by the equation:

$$\mathbf{F_i} = -\frac{\partial V}{\partial \mathbf{r_i}}. \tag{1.2}$$

It then follows that:

$$\mathbf{F_i} = m_i \frac{\partial^2 \mathbf{r}_i}{\partial t^2} = -\frac{\partial V}{\partial \mathbf{r_i}}. \tag{1.3}$$

The force field, V is composed of the non-bonded and bonded interactions between nearby particles,

$$V = V_{bonded} + V_{non-bonded}. \tag{1.4}$$

The bonded terms include the potential energies due to bond length (V_{bond}), bond angle (V_{angle}), dihedral or torsion angle ($V_{torsion}$), and improper dihedral angle ($V_{improper}$). The non-bonded terms include energetic potential due to van der Waals forces (V_{vdW}) and coulombic forces (V_{coul}).

$$V_{bonded} = V_{bond} + V_{angle} + V_{torsion} + V_{improper} \tag{1.5}$$
$$V_{non-bonded} = V_{vdW} + V_{coul} \tag{1.6}$$

MD simulations require force fields that have been parameterized from experimental data, *ab initio* and semi-empirical quantum mechanical calculations. Popular force fields for MD simulations of biomolecules include, but are not limited to, AMBER, CHARMM, and GROMOS. Once the force field is defined, the simulation can be initiated by assigning velocities to each particle, i based on the Maxwell-Boltzmann distribution at a known temperature, T.

$$p(v_i) = \sqrt{\frac{m_i}{2\pi k_B T}} \exp -\frac{m_i \dot{r}_i^2}{2 k_B T} \tag{1.7}$$

where k_B is the Boltzmann's constant. To solve for the new positions and velocities, a numerical integrator like the leap-frog integrator is used.

$$\dot{\mathbf{r}}(t + \frac{1}{2}\Delta t) = \dot{\mathbf{r}}_{\mathbf{i}}(t - \frac{1}{2}\Delta t) + \frac{\Delta t}{m}\mathbf{F}(t) \tag{1.8}$$

$$\mathbf{r}(t + \Delta t) = \mathbf{r}(t) + \dot{\mathbf{r}}(t + \frac{1}{2}\Delta t)\Delta t \tag{1.9}$$

The new positions can be saved in a new trajectory. In summary, most MD simulations follow a standard algorithm as follows:

1. Define initial conditions (force field, positions, initial velocities)

2. For time, $t = 0$ to a determined final simulation time, $t = t_{final}$

    a) Compute per-particle forces via equation (1.3)

    b) Update particle positions and velocities using numerical integration methods (i.e., solving for $\mathbf{r}_{\mathbf{i}}$ and $\dot{\mathbf{r}}_{\mathbf{i}}$ in equation (1.3))

    c) Output positions, velocities, and other quantities as desired.

3. Post-processing and trajectory analysis.

The large computational cost of MD simulations stems from the small timesteps, around 2fs, that are necessary to ensure a stable simulation, free of large energies and particle collisions. To ensure a stable system prior to running a production MD simulation, preparatory steps are performed. A typical workflow requires system preparation, energy minimization, and equilibration before the production run. System preparation involves selecting which atoms will be included in the simulation, selecting the force field, and dimensioning the boundary box. Energy minimization ensures that the system is initiated from a local energy minimum to reduce the probability that the system would experience large energies and collisions on the first timestep. Equilibration refers to an MD simulation that relaxes the system to a more stable and probable state in some thermodynamic ensemble. Equilibration is associated with a flattening of some computed property, such as root-mean-square-deviation (RMSD) or certain system energies, over time. After equilibration is complete, the production MD run is conducted to test any conditions of interest. Additional discussion, resources, and details of running MD simulations can be found in Braun et al. [15]

Due to the recent boost in computational power, MD simulations have sparked an interest to explore the potential dynamics underlying integrin binding, activation, and mechanosensing. Simulations by Nagae et al. investigated the docking between $\alpha_5\beta_1$ integrin and FN and predicted that D154 in α_5 and R1379 in FN to be major interacting pairs [95]. These results were confirmed by mutation studies that leveraged a solid-phase binding assay and surface plasmon resonance analysis to measure binding affinity when D154 was perturbed. Further, the simulations suggested a noticeable change in the β_1 integrin structure after binding to the RGD domain of FN. Their simulations, coupled with experimental mutation studies,

implied that binding could potentially induce some conformational changes key for integrin activation (i.e., the transition from low-affinty bent state to high-affinity extended state). On the cytoplasmic end, the reinforcement mechanism of proteins like kindlin and talin have been investigated using steered MD simulations. In *steered* MD simulations an external force or velocity condition is applied on chosen areas of the protein. These simulations are useful when aiming to accelerate reaction processes or testing the effect of forces on the chemical structure of proteins. In Ji et al.'s study, Talin was found to interact more strongly with the β_1 integrin cytoplasmic tail domain when pulled with a tensile force mimicking mechanical signaling [67]. Multiple studies have recently used steered MD simulations to induce integrin activation in silico to overcome the extensive sampling needed to explore the energy landscape across multiple states [90, 32, 13, 36, 23, 73]. These simulations have generated potential intermediate states during integrin activation and point to new mechanosignaling pathways. While these studies have been essential to advancing our understanding of integrin mechanosensing, a steered MD study on the effect of mechanical forces on the $\alpha_5\beta_1$-FN complex is needed. We hypothesize that tensile forces induce conformational changes in FN critical for maintaining the ECM while simultaneously transducing biophysical and biochemical signals to the cell via $\alpha_5\beta_1$ integrin.

1.5 Multiscale Modeling of Cell Adhesion

To effectively track the biophysical and biochemical effects of integrin mechanosignaling across the cell, researchers have used multiscale modeling. These methods allow for simulations across greater timescales (milliseconds to seconds) than afforded by MD (nanoseconds to microseconds). Prevailing methods to simulate integrin mechanotransduction include stochastic particle-based simulations and the finite element (FE) method [12]. These models are termed *multiscale* because they incorporate the binding kinetics derived from molecular interactions (nanometer scale), but manifest on the cell (micrometer scale).

Stochastic particle-based simulations approximate integrins and surrounding proteins as particles and employ Brownian Dynamics to estimate their motions throughout the cell. For example, the ligand binding affinity of β_1 is greater than β_3 integrin, and based on modeling by Bidone et al., this difference can lead to a dichotomy in adhesive functions, where β_1 more readily transmits traction stress and engages the actin within the cytoskeleton and β_3 tends to cluster while lacking a strong connection to the cytoskeleton [14]. The forces on the integrins was driven by the flow of actin filaments, but did not consider the effects of substrate stiffness. Oakes et al. leveraged a similar framework, but modeled the ECM as an elastic substrate [101]. More recently, Cheng et al. developed a model that included a first order Hill function that related the number of clustered integrins with a substrate spring constant to mimic the common observation that larger ECM stiffness correlates with greater integrin expression and clustering [25].

While stochastic models are needed to elucidate potential changes in integrin binding events and as a testing platform for in vitro studies of integrin, the cell mechanics are often

neglected. The computational coupling of cell mechanics with adhesion kinetics is pivotal to creating the next generation of treatments because changes in cell mechanosignaling due to morphology influences diseases such as cancer and wound healing. To this end, FE models that integrate adhesion kinetics have come to light. Zeng et al. built a soft matter model of the cell that recapitulated the cell's ECM rigidity sensing by spreading further on stiffer ECMs, as seen by in vitro experiments [143]. Additionally, Guo et al. showed that the addition of nonlinear viscoelastic parameters to the adhesion kinetics produces more realistic ECM mechanical behavior under stretching [52] Current advancements in multiscale modeling have shed light on adhesion kinetics and cell mechanics across scales. However, it remains a challenge to connect the nanoscale protein dynamics of the tertiary structure of integrin with microscale dynamics at the cell-matrix boundary via parameter values [12]. If we can address this need, we can better develop and test novel therapeutics or biomaterials in silico to mitigate diseases like cancer that exhibit altered chemical and mechanical environments.

1.6 Dissertation Structure and Scope

This dissertation addresses the stated challenges in cell adhesion mechanobiology that benefit from the use of computer simulations to understand biophysical mechanisms governing health. Specifically, we conducted three studies using steered MD simulations or the FE method to improve our understanding of the biophysical dynamics of $\alpha_5\beta_1$ integrin mechanosensing and cell adhesion. We aimed to test how mechanical forces may play a role in inducing structural changes in $\alpha_5\beta_1$-FN that propagate to new cell-matrix adhesion dynamics across the cell body. This work is split into three chapters. The first focuses on the molecular interactions in $\alpha_5\beta_1$-FN, the second discusses a cell-matrix adhesion interface model, and the third connects the first two studies across the molecular and cell scales.

- **Chapter 2: Molecular Mechanism of $\alpha_5\beta_1$ Mechanosensing**
  This study examines the $\alpha_5\beta_1$-FN complex under applied velocity using steered MD simulations. We provide evidence for a unique mechanism by which the RGD and synergy site binding domains in FN collaborate to impose an allosteric shift in the head domain of $\alpha_5\beta_1$ that would not be present if only RGD was bound. We shed light on the importance of maintaining the two binding sites to reinforce cell adhesion while revisiting potential force-dependent mechanisms for FN unfolding and assembly.

- **Chapter 3: Dynamic $\alpha_5\beta_1$-FN Adhesion Collaboration**
  This study aimed to show the role FN's synergy site has on whole-cell adhesion dynamics during cell contraction that may go unseen in traction force microscopy and FRET-based experiments. Specifically, we analyzed the short-term force transmission across $\alpha_5\beta_1$-FN bonds with and without FN synergy site mutagenesis. We propose a mechanism by which integrin binding inhibition may not result in reduced per-integrin force capacity.

- **Chapter 4: Bridging Simulations of $\alpha_5\beta_1$-FN Across Scales**
  Finally, we attempted to connect the nanoscale protein dynamics of $\alpha_5\beta_1$-FN with its corresponding whole-cell adhesion dynamics. To do so, we utilized the force-extension characterization from the steered MD simulations from the study in Chapter 2 and integrated it into the whole-cell adhesion interface model developed in Chapter 3. We discuss the implications and limitations of this computational framework and how it may be improved with robust parameterization and experimental validation.

Chapter 5 concludes the dissertation with a commentary on how the three studies fit within the greater field of cell mechanobiology. We outline key next steps for advancing the present work on cell adhesion dynamics and integrin mechanosensing to advance medicinal efforts that address cancer.

Chapter 2

Molecular Mechanism of $\alpha_5\beta_1$ Mechanosensing

2.1 Introduction

Adhesion bonds enable cells to interact dynamically with their surrounding environment, orchestrating the regulation of essential cellular processes such as proliferation, differentiation, and apoptosis [29, 5, 77, 63, 110]. Integrins are transmembrane, heterodimeric proteins that play an important role in cell adhesion by tethering the inside and outside of the cell via binding partners in the extracellular matrix (ECM) [28]. $\alpha_5\beta_1$ integrin is one of 24 integrin heterodimers present in mammals [63] and mediates cell-tissue homeostasis by binding to its primary ligand, fibronectin (FN) [113, 60]. $\alpha_5\beta_1$ and FN are linked together at the RGD (Arg-Gly-Asp) motif and stabilized by the eight-amino-acid-long DRVPHSRN synergy site on FN [10], allowing extracellular and cytoplasmic forces to be transmitted across the cell membrane. The accumulation of $\alpha_5\beta_1$-FN bonds form the basis for nascent cell adhesion and cell motion. Beyond $\alpha_5\beta_1$-FN's role in maintaining cell-tissue homeostasis, it has been implicated as a potential therapeutic target for cancer [57, 145, 19]. For example, dysfunctional and overexpressed integrin bonds are markers of uninhibited cancer cell migration [116, 71]. As such, numerous antagonists have been developed to attenuate integrin bonds, aiming to impede the invasion of multiple cancer cell types. Despite considerable efforts, these antagonists have faced challenges, demonstrating limited success in effectively preventing cancer cell invasion. [112, 27]. Therefore, a better understanding of the biophysical nature of the $\alpha_5\beta_1$-FN bond is needed to reveal mechanisms that can be exploited to target metastasis.

$\alpha_5\beta_1$ integrin creates a catch bond with FN [72, 122, 10], which is a type of bond that increases in lifetime with greater applied force. The $\alpha_5\beta_1$-FN catch bond allows for strong adhesion at the leading edge of a migrating cell and a steady release of the bond at the cell's trailing end. Catch bonds have inspired development of synthetic catch bonds for manufacturing resilient materials [30, 31, 142]. However, the mechanisms involved in the $\alpha_5\beta_1$-FN catch bond's ability to maintain its characteristic strength is unknown. Understanding

the underlying mechanism of $\alpha_5\beta_1$-FN catch bond resilience could identify structural protein characteristics that can be targeted to arrest cancer cells through substrate or protein modifications. Moreover, structural dynamics that enable catch bond behavior may inspire development of resistant nanomaterials with self strengthening properties.

Ideally, the $\alpha_5\beta_1$-FN catch bond could be imaged while an applied force is applied with a single-molecule testing setup (e.g., optical trap or magnetic tweezers). However, current atomic-resolution molecular imaging techniques, like cryo-EM and x-ray crystallography, require immobilizing the protein, making visualization of *in situ* structural changes of $\alpha_5\beta_1$-FN challenging. In light of these experimental limitations, molecular dynamics (MD) simulations have been used to visualize protein conformational changes over time [73, 91].

Given $\alpha_5\beta_1$-FN's critical role in mechanosensing via its elusive catch bond dynamics, we used MD simulations to visualize the motion of $\alpha_5\beta_1$-FN when acted on by an external load. We introduce a "pivot-clip" mechanism to model the $\alpha_5\beta_1$-FN's catch bond-like behavior, where the RGD motif acts as a stable pivot for FN about β_1 integrin and the synergy site acts as a reinforcing clip connecting FN to α_5. Past experiments demonstrated that mutating the synergy site diminishes catch bond behavior and weakens whole-cell and single molecule adhesion to $\alpha_5\beta_1$ [122, 44]. Even so, a lack of the synergy site does not significantly limit cell traction on a 2D substrate under minimal contractility [20]. To explain how the synergy site may promote $\alpha_5\beta_1$-FN binding while maintaining cell traction, we developed a 2D finite element (FE) model of the adhesive interface in Chapter 3. Based on our MD and FE simulations, we present a theory that the synergy site in FN reinforces cell adhesion via stronger binding affinity and a mechanosensitive pivot-clip mechanism.
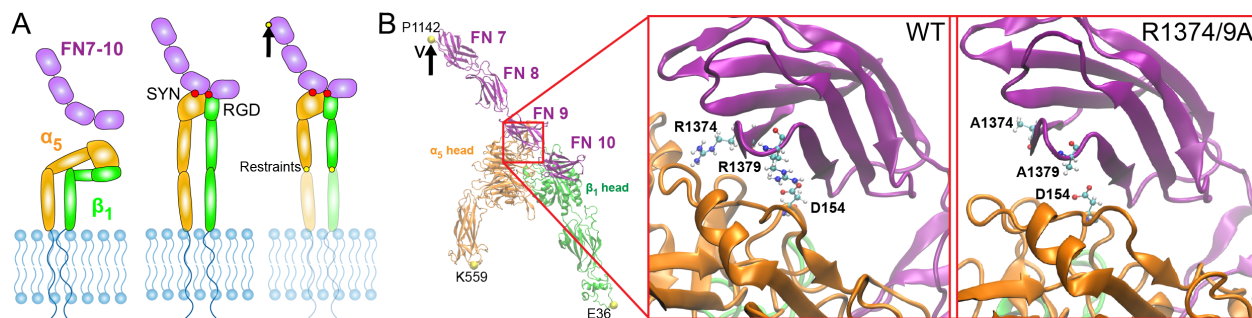
Figure 2.1: A) Schematics of $\alpha_5\beta_1$ integrin in its bent-closed, inactive state with FN fragment 7-10 unbounded (left), extended-active state in complex with FN (middle), and under an applied load (right). B) The Cryo-EM structure of $\alpha_5\beta_1$-FN with the individual integrin heads and FN fragments labeled. The MD simulations applied a velocity to the P1142 residue while restraining K559 and E36. Zoomed in region shows wildtype synergy site with R1374 and R1379 (left) and double mutated R1374/9A synergy site (right). D154 binds to R1379 and is shown as a reference. SYN: synergy site. RGD: arg-gly-asp.

2.2 Materials and Methods

Steered Molecular Dynamics Simulations

Constant velocity, all-atom steered MD simulations of the ectoplasmic $\alpha_5\beta_1$-FN complex were run in GROMACS 2020.4 [1]. The 7NWL crystal structure file of the $\alpha_5\beta_1$-FN complex with the TS2/16 Fv-clasp was downloaded from the protein data bank. The $\alpha_5\beta_1$ integrin head domain and the FN type III fragment 7-10 were isolated using PyMOL [115]. We used MODELLER 10.4 [138] to impose a virtual R1374/9A double mutation, switching the arginine residues in positions 1374 and 1379 in FN to alanine (Figure 2.1B).

Wildtype and mutated structures were solvated in a TIP3P water box (18nm x 45nm x 19nm) with 0.15mM NaCl. Energy was minimized for 15k steps with the steepest gradient descent algorithm, followed by an equilibration sequence of a 1ns NVT simulation at 310K followed by a 10ns NPT simulation at 1 bar and 310K, per physiological conditions. Equilibration was verified by ensuring that the RMSD of the fully unrestrained complexes (Figure S1) were within 0.3nm resolution of cryoEM.

The K559 and E36 residues at the proximal ends of the integrin headpieces were then restrained. P1142 at the distal end of the FN fragment was pulled at 10 and 1nm/ns using a 50kJ/mol/nm spring with an umbrella potential for 3ns and 20ns, respectively. The steered MD simulations used a 2fs timestep. We visualized the crystal structures and MD simulation trajectories using Visual Molecular Dynamics (VMD) 1.9.4a [62]. All parameters for the MD simulations are available in the supplementary materials (Table S1). The force and extension at $\alpha_5\beta_1$-FN's center-of-mass (COM) were derived directly from the output files from Gromacs. The extension was measured as the displacement of the $\alpha_5\beta_1$-FN's center-of-mass with respect to the first simulation frame. The radius of gyration of the α_5 and β_1 heads was measured using the built-in Gromacs function, gmx gyrate. Distances between key bonds at R1374 and R1379 were calculated by averaging the distance between atom pairs that could form hydrogen bonds using the VMD bond select and graph tool. We used a distance cutoff of 0.35nm (3.5 Angstrom) and donor-hydrogen-acceptor angle cutoff of 30 in VMD to detect hydrogen bonds.

Synergy Site Departure Energy

To calculate the energy required for the synergy site to depart from α_5, we used in-house Python code to integrate the force and COM extension data from the beginning of the simulation to the time of the force peak just before the rapid increase in extension rate. Since the force-extension data is non-monotonic, we first fitted a piece-wise linear function over the force-extension data before integrating with trapezoid rule.
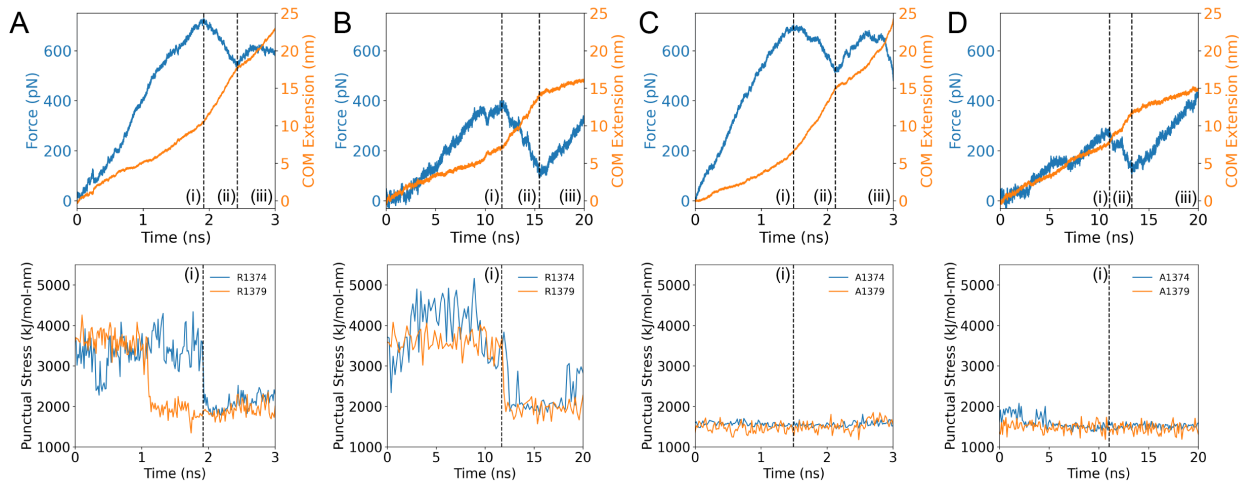
Figure 2.2: Force and COM extension over time plotted over punctual stress at R1374/1379 of the synergy site for A) 10nm/ns wildtype $\alpha_5\beta_1$-FN, B) 1nm/ns wildtype $\alpha_5\beta_1$-FN, C) 10nm/ns R1374/9A $\alpha_5\beta_1$-FN, and D) 1nm/ns R1374/9A $\alpha_5\beta_1$-FN. Positions (i), (ii), and (iii) correspond to the time at the peak force, local minimum, and final frame, respectively.

Force Distribution Analysis

Time-resolved force distribution analysis (trFDA) was used to measure the punctual stresses based on the Coulombic interactions at all residues across all simulation time steps [26]. The punctual stress is the absolute value of scalar pairwise forces exerted on each residue. Normally, stress would be in units of energy. However, the developers of punctual stress defined it as "force on a dimensionless point" which uses units of force (kJ/mol-nm). We opted to use this definition of punctual stress to remain consistent with past studies. Parameters for the trFDA are available in Table 2.1.

Table 2.1: Time resolved Force Distribution Analysis Parameter Settings

Parameter	Setting
Pairwise forces	Summed
Pairwise groups	Protein
Residue based calculation	Punctual Stress
Pairwise force type	Coulombic interactions only

Long-term NPT Equilibration Simulations

Longer term stability of the $\alpha_5\beta_1$-FN complex after synergy site mutagenesis was tested with two 250ns NPT simulations of $\alpha_5\beta_1$-FN9-10: one wildtype and one R1374/9A mutant.

The 7NWL pdb file was truncated from $\alpha_5\beta_1$-FN7-10 to $\alpha_5\beta_1$-FN9-10. A R1374/9A double mutation was again induced in silico via MODELLER 10.4 [138]. The system contained $\approx$ 1.3M atoms in a 15nm x 30nm x 30nm box after solvation. NaCl concentration was kept at 0.15mM. The 250ns NPT simulation was preceded by a 15k step energy minimization and 1ns NVT as described previously. 100kJ/mol-nm^2 restraints were placed on residues D603, E445, and D1328 (Figure 2.7A) in the x and y directions, representing the remaining structures of integrin and FN while limiting periodic box crossing. No other restraints were placed. We used GROMACS 2020.4 [1] to measure backbone RMSDs, nonbonded energies, axes of inertia, distances, and hydrogen bonds. Axes of inertia were used to calculate angles by taking the inverse cosine of the dot product of a unit vector pair. Measurements were tested for normality with the Kolmogorov-Smirnov test. Since all data was non-normal, the wildtype and mutant trajectories were compared using the Wilcoxon signed rank test ($\alpha = 0.05$).

Extensional Stiffness of α_5 and β_1 headpieces

Extensional stiffnesses of α_5 and β_1 headpieces were determined independently using 100ns NPT simulations. The 7NWL pdb file was isolated to either the α_5 head ($\approx$ 438K atoms in a 16.5nm x 16.5nm x 16.5nm box post solvation) or β_1 head ($\approx$ 463K atoms in a 16.8nm x 16.8nm x 16.8nm box post solvation). Again, energy minimization for 15k steps and a 1ns NVT as previously described were run in GROMACS prior to the 100ns NPT simulation. Extensional stiffness, k, for each molecule was calculated using:

$$k = \frac{k_B T}{< (L(t)- < L(t) >_{\Delta t})^2 >_{\Delta t}},\tag{2.1}$$

where $k_B T$ is Boltzmann's constant, $T = 310K$, $L(t)$ is the length of the reaction coordinate at time, t, and $<>$ denotes the time average [130]. For α_5, the center-of-mass distance between D154 (synergy site binding residue) and D603 (connects to lower integrin legs) in α_5 was chosen as the length of the reaction coordinate. Similarly for β_1, the Metal-Ion Dependent Adhesion Site (MIDAS; binds to RGD) and E445 (connects to lower integrin legs) were chosen. After the system had equilibrated, we used the latter 50ns for the extensional stiffness calculation. For each molecule, the distance data was divided into five 10ns blocks. Distances were saved every 10ps during the simulation, resulting in 1000 data points per block to calculate five k values per head. A Wilcoxon signed-rank test compared the means of the extensional stiffnesses of α_5 and β_1. The angle between the propeller and thigh in α_5 was measured as described previously.
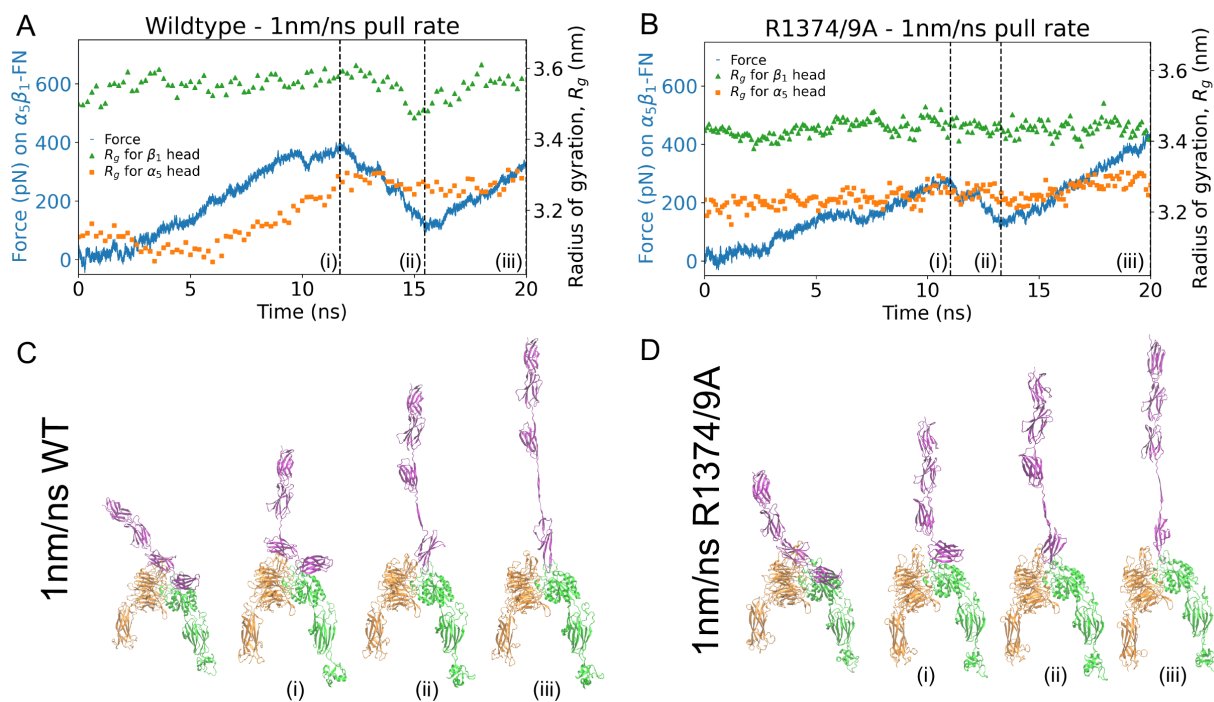
Figure 2.3: Force on $\alpha_5\beta_1$-FN and radius of gyration of α_5 and β_1 head for the 1nm/ns runs for the A) wildtype and B) mutant. Positions (i), (ii), and (iii) correspond to the time at the peak force, local minimum, and final frame. The four shown frames from the simulation correspond to the first frame, (i) peak force, (ii) local minimum, and (iii) final frame for C) wildtype and D) mutant.

2.3   Results and Discussion

FN9-α_5 disengagement coincides with synergy site deactivation

We analyzed force-extension in conjunction with punctual stress to determine the role of the synergy site in FN9-α_5 disengagement. The initial force-extension curve of the wildtype $\alpha_5\beta_1$-FN structure followed a linear response for both 10 and 1 nm/ns pull rates until peaking at 729pN and 462pN, respectively (Figure 2.2A and B). The peak forces coincided with sharp decreases in the punctual stress at the synergy site, namely at sites R1374 and R1379 in FN9. R1379 has been shown to be connected to D154 in the α_5 head via a salt bridge [116]. However, R1374 has not been previously observed to be actively linked to α_5. At both pull rates, R1374 retained higher punctual stresses than R1379, but the sequence of disengagement was dependent on the pull rate. Under the faster pull rate condition, the salt bridge was disrupted prior to a reduction in force on $\alpha_5\beta_1$-FN and punctual stress at R1374. This indicated that while the load on FN was sufficient to overcome the energetic barrier

to break the salt bridge connecting FN to α_5, persistent electrostatic interaction at R1374 enabled FN9 to remain near the α_5 head. This was not observed under the slower pull rate simulation, where we noted simultaneous punctual stress reduction in R1374 and R1379 at the peak force time point. While the punctual stresses at both residues were elevated during load ramping, synergy site engagement reduced after the force peak.

R1374 and R1379 were contributors to punctual stress at the synergy site prior to the drop in force on $\alpha_5\beta_1$-FN (Figure S2). In both pull rate conditions, the combined punctual stress at R1374/9 prior to the force peak was on average two times higher than other synergy site residues. Due to the high electrostatic activity of both sites prior to FN9 and α_5 separation, we mutated both residues (R1374/9A) to evaluate their roles in maintaining $\alpha_5\beta_1$-FN's structural response to force. At 10nm/ns, the force response of the wildtype and mutant $\alpha_5\beta_1$-FN were similar, peaking at 729pN and 704pN, respectively (Figure 2.2C). However, the punctual stresses at A1374 and A1379 were 45% and 40% lower in the mutant case than the wildtype (Figure 2.2C and D), indicating that the mutation disrupted synergy site engagement, but not necessarily reduced force transmission. Similar trends were observed in the 1nm/ns force rate condition, where the punctual stresses at A1374 and A1349 were small relative to R1374 and R1379, and the first peak force was lower in the mutant case (wildtype = 462pN, mutant = 291pN; Figure 2.2D).

Although our results appeared to conflict with the understanding that synergy site mutagenesis decreases cell adhesion strength, the relative energetic barrier required to separate the synergy site from integrin revealed closer agreement with the literature [44, 122, 72, 127, 78]. While we noticed a 171pN difference (37% less than the wildtype) in the first peak force in the 1nm/ns mutant model, we only noted a 25pN drop (3% less than the wildtype) in the 10nm/ns model. This is likely a consequence of the high pull rates used in these models that may hide molecular mechanisms. Therefore, long term simulations at slower pull rates and smaller forces are needed to overcome this limiting factor. We worked towards this goal in a later section. For now, to overcome this potential conflict with the literature, we opted to use the area under the force-extension curve (Figure 2.4) as a proxy for measuring synergy site departure energy, which would be related to the energy barrier required to pull FN9 away from α_5. We defined the *synergy site departure force* as point (i) in all simulations (Figure 2.2). Forces recorded after the *synergy site departure force* would work to unfold FN and unbind RGD. We found that the synergy site departure energies were greater in the wildtype, in line with past in vitro experiments that show greater binding affinity of $\alpha_5\beta_1$ integrin to FN in the presence of the synergy site [127, 44]. At 10nm/ns, the wildtype and mutant energies were 4012pN-nm and 2715pN-nm, respectively. At 1nm/ns, the wildype and mutant had a energies of 1529pN-nm and 883pN-nm, respectively. These values do not have any physical meaning, but enabled a comparison between the wildtype and mutant. From our current steered MD data, we cannot make claims about the effect of the synergy site on RGD binding specifically. Free energy methods such as FEP (free energy perturbation) and MMPBSA (Molecular Mechanics Poisson-Boltzmann Surface Area) would be more appropriate to study these effects computationally and are the subject of ongoing work.
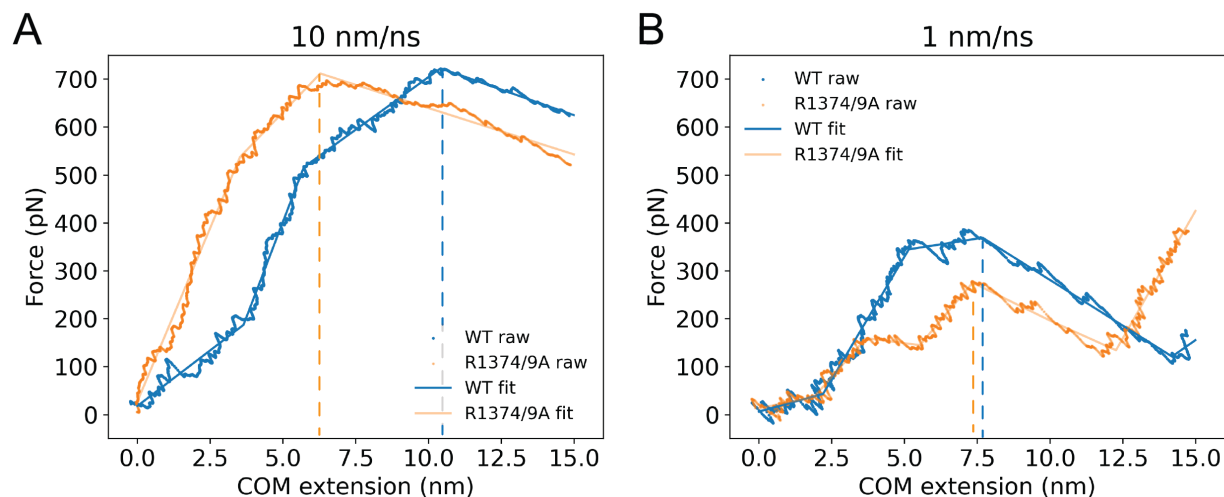
Figure 2.4: Force-extension plots for A) 10nm/ns and B) 1nm/ns pull rates. Dashed lines indicate the extension at the synergy site departure force. A moving average with a window size of 10ps was applied to the raw data for visualization purposes only. The piece-wise linear fit was performed over all points.

Punctual stress measurements provided insight into per-residue interactions at the synergy site and are substantiated by atomic-level interactions. Specifically, the formation and breakage of hydrogen bonds between α_5 and FN9 are essential for relaying force between the two. Since high punctual stresses were observed on R1374 and R1379, we tracked bonds between R1379—D154 and R1374—E124 (Figure 2.5A). At both pull rates, the R1379—D154 salt bridge was broken before the maximum force was reached, while residue R1374 remained bounded to either E124 or E81 depending on the pull rate (Figure 2.5B-C). The measured distance between R1374—E124 was within the range of a hydrogen bond (0.35nm) after the departure of the R1379—D154 bond (10nm/ns case; Figure 2.5D). At the slower pull rate, R1374 transitioned from E124 to E81, maintaining contact between FN9 and $\alpha_5\beta_1$ together with R1379—D154 (Figure 2.5E). Both bonds then released and the force on $\alpha_5\beta_1$-FN consequently dropped. The R1374/9A double mutation severed the main points of contact between FN9 and $\alpha_5\beta_1$, pushing the distance between the residues to 0.65nm, beyond the 0.35nm hydrogen bond length cutoff (Figure 2.5F).

For all test cases, the peak forces were followed by sharp increases in extension rate, suggesting a rapid conformational change of $\alpha_5\beta_1$-FN (Figure 2.2). In the case of the wildtype 10nm/ns pull rate, the measured extension rate increased from 5.10nm/ns to 14.4nm/ns. Similarly, the wildtype 1nm/ns pull rate increased in rate from 0.547nm/ns to 1.82nm/ns (Table 2.2). Notably, there was a mismatch between the input rate and measured rate. Steered MD simulations attempt to control the pull rate via a virtual spring connecting a
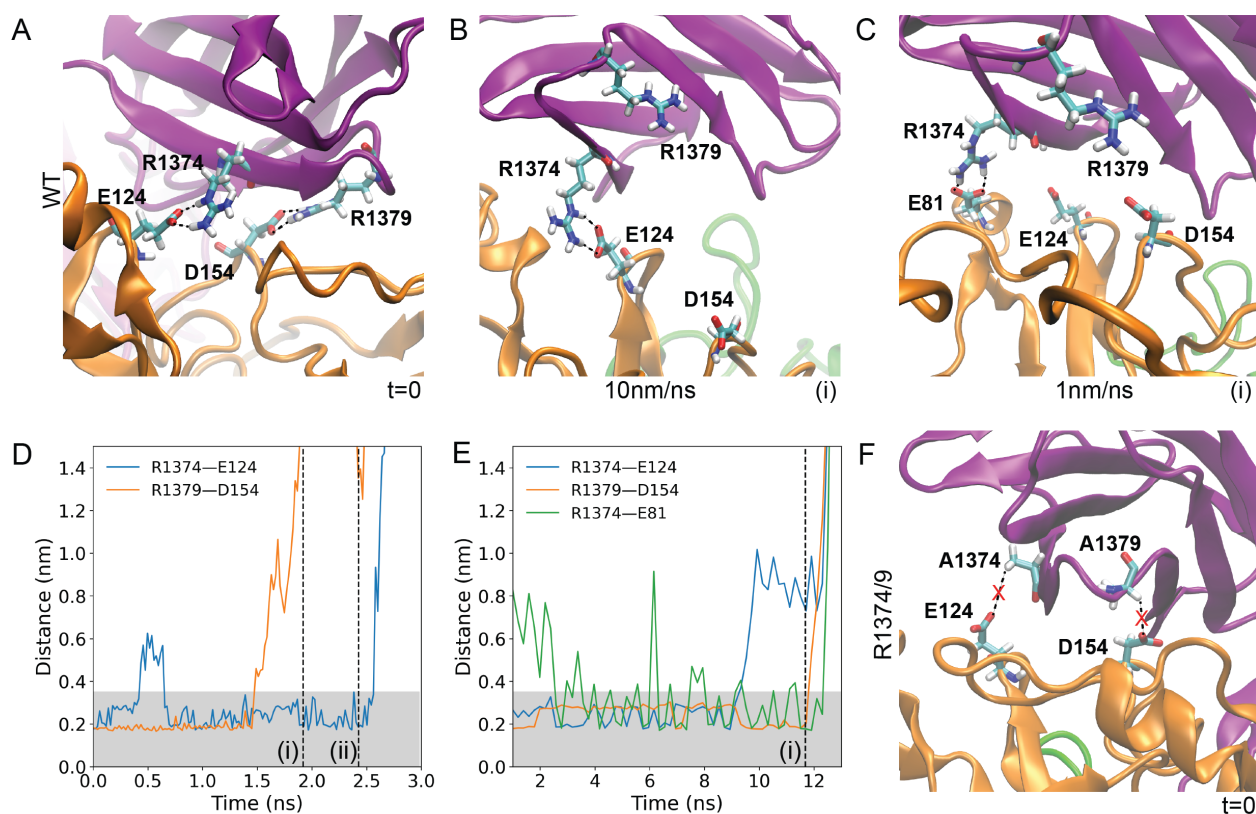
Figure 2.5: A) Interactions between R1374—E124 and R1379—D154 at the beginning of the wildtype simulations. B) At the force peak of the 10nm/ns wildtype simulation, the R1379—D154 salt bridge was broken but R1374—E124 remained. C) At the force peak of the 1nm/ns wildtype simulation, the R1379—D154 salt bridge was broken and R1374 formed a new hydrogen bond with E81. D) Distance between R1374—E124 and R1379—D154 for the 10nm/ns wildtype simulation. E) Distance between R1374—E124, R1379—D154, and R1374—E81. Shaded regions indicate 0.35nm, or the assumed approximate length for a hydrogen bond. The vertical dashed line is the time point of the force peak. F) The R1374/9A double mutation separated the A1374—E124 and A1379—D154 bonds to over 0.65nm, preventing hydrogen bond formation.

dummy atom to the pulled site. While the atom moves at a constant rate, the molecule's response depends on the virtual spring deflection and local conformational changes associated with the molecule. Therefore, it is unlikely that the input pull rate matches the measured pull rate experienced by the molecule. Further, the output extension was measured as the distance traveled by $\alpha_5\beta_1$-FN's COM, which depends on the structural behavior.

Our reported forces and pull rates are many orders of magnitude higher than what has been tested using atomic force microscopy (AFM; 1 - 15 μm/s) [78]. Given our large 1.5M

Table 2.2: Measured extension rate (nm/ns) of $\alpha_5\beta_1$-FN under load in reference to the (i) peak and (ii) valley force as seen in Figure 2A-D

	Prior to (i)	Between (i) and (ii)	After (ii)
10nm/ns wildtype	5.10	14.4	9.21
10nm/ns R1374/9A	4.17	13.2	9.15
1nm/ns wildtype	0.547	1.82	0.546
1nm/ns R1374/9A	0.705	1.63	0.562

atom system, we compromised on the simulation time scale by applying extension rates within the bounds of past steered MD simulations of integrin (0.1 - 10 nm/ns) [73, 23]. The fast extension rates contributed to simulated forces beyond what has previously been measured experimentally (single molecule rupture forces of 80-120pN) [78]. Nevertheless, the difference between the forces generated at 1 and 10 nm/ns hinted at force-dependent behavior arising from synergy site engagement. Larger conformational changes were visually noted in the α_5 head during 10nm/ns pulling compared to 1nm/ns pulling. Further, the mutants showed little to no changes in the movement of the α_5 head, suggesting that the interactions at the synergy site could work to deform α_5. Therefore, we quantified the conformational changes associated with synergy site engagement when subjected to high pull rates.

Conformational response of α_5 and β_1 was hampered by lack of synergy site engagement

We informed the differences in force and extension rates across conditions by visualizing the structural changes of $\alpha_5\beta_1$-FN under both pull rates for the wildtype and mutant cases. We used the radius of gyration to quantify conformational changes within α_5 and β_1 heads, with smaller radii indicating more compact proteins. In both wildtype runs, the α_5 head, which is connected to the synergy site on FN9, stretched further than the β_1 head, which is connected to the RGD motif on FN10. However, pull rate affected the degree of α_5 stretching. The lower 1nm/ns pull rate resulted in 0.165nm increase in α_5's radius of gyration (Figure 2.3A), compared to a 0.407nm increase in the 10nm/ns rate simulation (Figure 2.6A). Most of the α_5 head deformation resulted before the peak force and synergy site disengagement. For the respective 10nm/ns and 1nm/ns rates, 97.7% and 99.0% of the max α_5 head deformation occurred prior to the peak force, when the synergy site loosened. From the observations of $\alpha_5\beta_1$-FN's quaternary structure, we noticed the α_5 head straightening while FN9 remained connected at the synergy site (Figure 2.3C). Further, at higher forces, α_5 underwent a greater degree of stretching while FN9 unfolded (Figure 2.6C). In contrast, lower forces seemed to encourage synergy site disengagement prior to FN unfolding. Our observation suggests that $\alpha_5\beta_1$-FN's catch bond dynamics may be promoted by greater synergy site interaction in combination with α_5 extension to resist larger forces. The greater interaction may stem from the hydrogen bond electrostatics at R1374 and R1379 that bridge α_5 to FN9 (Figure 2.5).
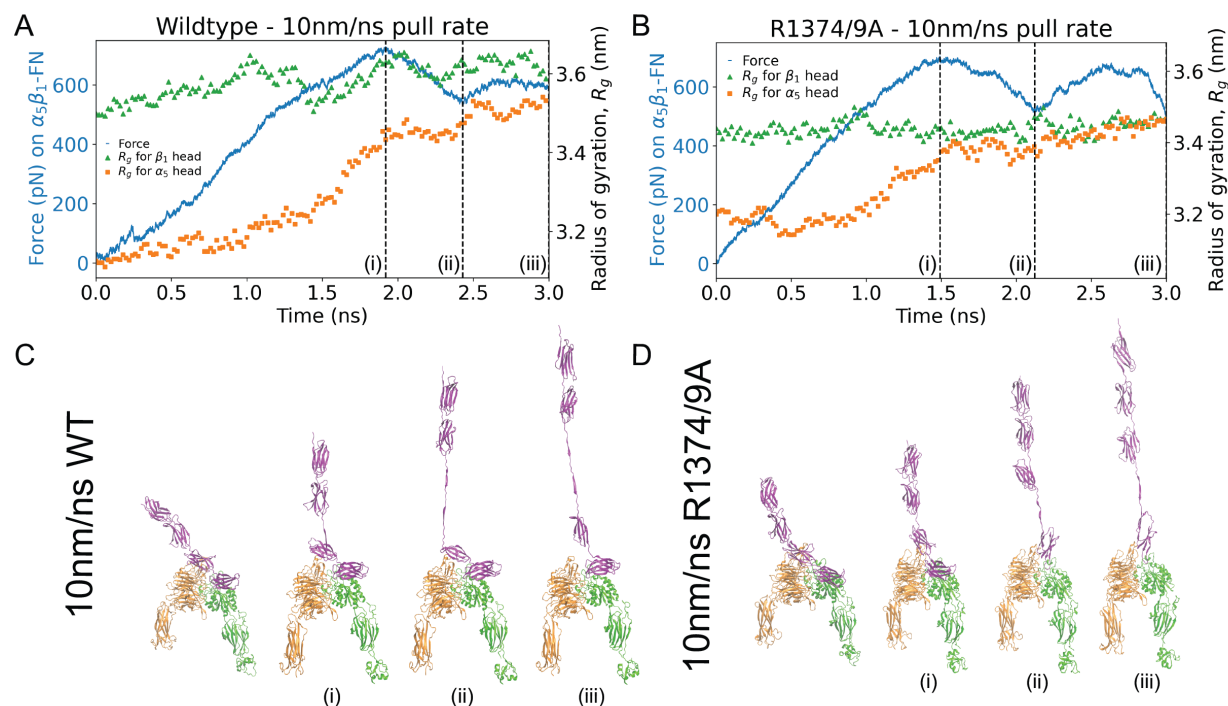
Figure 2.6: Force on $\alpha_5\beta_1$-FN and radius of gyration of α_5 and β_1 head for the 10nm/ns runs for the A) wildtype and B) mutant. Positions (i), (ii), and (iii) correspond to the time at the peak force, local minimum, and final frame. The four shown frames from the simulation correspond to the first frame, (i) peak force, (ii) local minimum, and (iii) final frame for C) wildtype and D) mutant.

We tested the degree to which the synergy site contributed to structural changes in $\alpha_5\beta_1$-FN by mutating the site (R1374/9A) and again measuring the radius of gyration of α_5 and β_1 under an external load on FN. Surprisingly, the mutant pulled at 10nm/ns still resulted in conformational changes of the α_5 head, with the radius of gyration increasing by 0.266nm. However, this was less than the 0.407nm increase observed in the wildtype (Figure 2.6B). Further, the mutant pulled at the slower 1nm/ns showed virtually no deformation of α_5 or β_1 (Figure 2.3B). Investigating the quaternary structure of the mutant revealed that FN9 was separated immediately from α_5 (Figures 2.3D and 2.6D). As the FN beta sheets stacked vertically in alignment with the pulling direction, the force increased and peaked as soon as FN10 begun to unfold. For all simulations, the β_1 head kept a more stable conformation, maintaining its radius of gyration within 0.12nm. These results are indicative of a new mechanism whereby α_5 and FN deformation patterns may be altered due to interactions at the synergy site. However, the fast pull rates are five orders of magnitude higher than even the slowest AFM pull rates, posing the question of whether these states may be realized and

more importantly, have a physical meaning. So, while our results were promising, we aimed to address the pull rate limitation by conducting longer term simulations and emphasizing our analysis on the synergy site and integrin interaction.
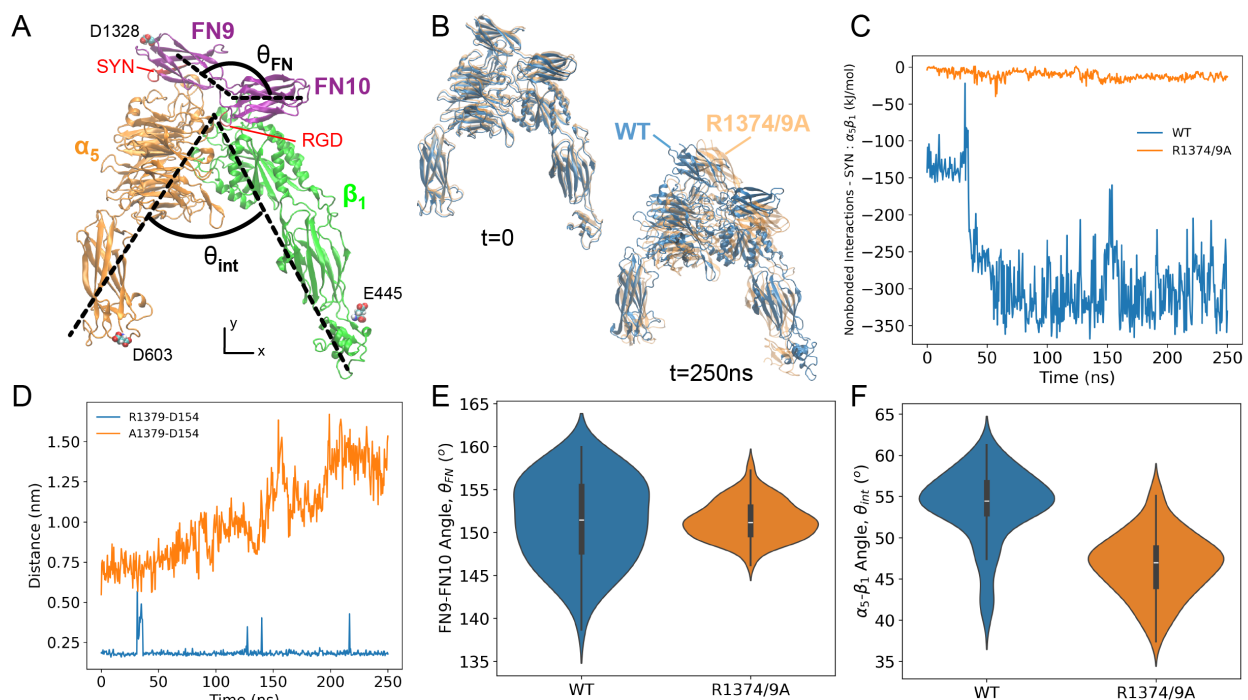
Figure 2.7: A) Cryo-EM structure $\alpha_5\beta_1$-FN9-10. Small restraints were placed on D603, E445, and D1348 in the x and y directions to mimic the respective continuing structures of integrin and FN. θ_{int} was defined the angle between the principal axes of inertia of α_5 and β_1, respectively. Similarly, θ_{FN} was defined as the angle between the principal axes of inertia of FN9 and FN10, respectively. Dashed lines are hand-drawn and indicate an approximation of the principal axes. SYN: synergy site. B) Superposition of the wildtype (blue) and mutant (orange) during the first and last frames of the respective 250ns simulations. C) Nonbounded interaction energy between the synergy site and $\alpha_5\beta_1$ integrin for wildtype and mutant. D) Minimum distance between residue 1379 (FN9) and D154 (α_5) for wildtype and mutant. E) Violin plot of FN9-10 angle for last 50ns of 250ns simulation (WT = $151.4 \pm 4.9°$, R1374/9A = $151.4 \pm 2.2°$, $p = 0.98$). F) Violin plot of $\alpha_5\beta_1$ angle for last 50ns of 250ns simulation (WT = $53.9 \pm 4.3°$, R1374/9A = $46.7 \pm 3.8°$, $p < 0.0001$).

Synergy site interactions maintained FN9 and α_5 close

We used two 250ns NPT simulations of $\alpha_5\beta_1$ integrin in complex with FN9-10 (wildtype and R1374/9A) to understand the role of the synergy site in maintaining integrin and FN
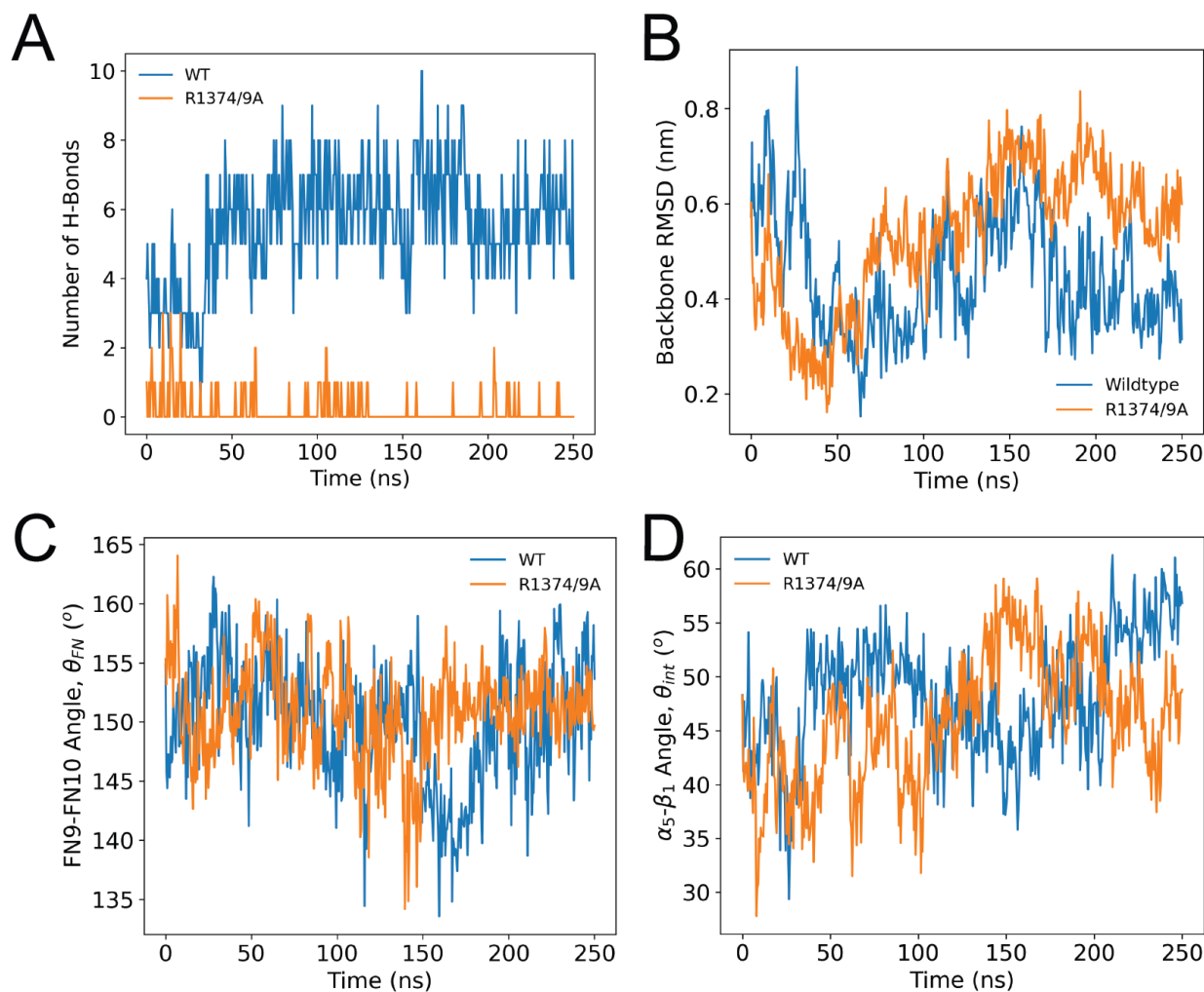
Figure 2.8: A) Number of hydrogen bonds, B) Backbone RMSD, C) FN9-FN10 Angle, and D) α-β_1 angle over the 250ns simulation of the wildtype (WT) and mutant.

conformational stability. Visual observation showed separation of mutant FN9 away from integrin as well as minor deviations to the integrin headpieces (Figure 2.7B). Therefore, we investigated the connection between FN9 and integrin. As expected, we found that the nonbonded interactions (van der waals and coulombic energies) between the synergy site and $\alpha_5\beta_1$ were greater in the wildtype structure (Figure 2.7C). These results aligned with the shorter distance between R1379 in FN9 and D154 in α_5 (Figure 2.7D) as well as the greater number of hydrogen bonds between the synergy site and α_5 (Figure 2.8A).

Lower synergy site engagement widened the gap between FN9 and α_5, but only minor structural changes in the integrin heads and FN were realized. We conducted structural

analyses using the final 50ns of the 250ns simulation. The nonbonded interactions (Figure 2.7A), the hydrogen bond count (Figure 2.8A), and backbone RMSD (Figure 2.8B) of $\alpha_5\beta_1$-FN9-10 (wildtype and mutant) leveled off at $\approx$ 200ns, suggesting system equilibration. Longer simulations would be necessary to evaluate whether the system fully equilibrated, but based on these initial trends, we enforced the latter 50ns cutoff. Since the synergy site in FN9 and RGD in FN10 are two anchoring contact points for integrin, we posited that releasing FN9 from α_5 via synergy site inhibition would increase FN9-10 flexibility. Interestingly, the means of the FN9-10 angles (θ_{FN}) in both cases was not statistically significant and variance was greater in the wildtype (Figure 2.7E), which would indicate that the wildtype FN9-10 was fluctuating to a greater degree even as the synergy site was interacting more strongly. Further, the α_5-β_1 angle (θ_{int}) in the wildtype was 7.2° larger than the mutant, pointing to a modest closing of the integrin heads in the mutant (Figure 2.7F). This closing was predominantly a result of FN9-10 rotation rather than a state transition of α_5. The propeller-thigh angle ($\theta_{\alpha5}$) was 4.7° greater in the mutant, whereas the β_1-FN10 angle ($\theta_{\beta1-FN10}$) was 12.1° lower in the mutant (Figure 2.9). FN9-10 retained its shape, with only a 0.01nm difference in radius of gyration between mutant and wildtype (Figure 2.10A-B). Additionally, there was no statistically significant difference in the radius of gyration of α_5 between mutant and wildtype (Figure 2.10C-D). The radius of gyration of β_1 in the mutant was 0.16nm smaller (Figure 2.10E-F), indicating a small amount of compression of β_1 as it interacted with FN10. The time series data of θ_{FN} (Figure 2.8C), θ_{int} (Figure 2.8D), $\theta_{\alpha5}$ (Figure 2.9B), and $\theta_{\beta1-FN10}$ (Figure 2.9D) showed overlap between mutant and wildtype throughout the entire simulation, meaning that some states may be similar to each other, but on average, the conformational measurements suggest that the synergy site locks FN9 to α_5 and prevents rotation of FN9-10.

The unlocking of FN9 due to reduced synergy site energetics did not promote appreciable changes at integrin's RGD binding location. We first measured the nonbonded interaction energies between RGD and $\alpha_5\beta_1$, including the MIDAS cation, which showed no differences in energies after, and even before the imposed 200ns cutoff (Figure 2.11A). Additionally, the number of hydrogen bonds between α_5 and RGD (Figure 2.11B) well as β_1 and RGD (Figure 2.11C) were similar between the wildtype and mutant. From this data, we assumed that RGD would be a stable location for FN to maintain binding to integrin regardless of synergy site engagement. To confirm the conformational stability at the RGD binding area, we measured the mean and minimum distances between notable interactions at this site (Figure 2.12A). These included RGD-MIDAS (Figure 2.12B-C), D227-RGD (Figure 2.12D-E), and S134-MIDAS (Figure 2.12F-G). As expected, the distances between these pairs remained small in both the wildtype and mutant. Although there were differences in the S134-MIDAS mean and minimum distance, the observed 0.05-0.75nm distance difference was not enough to decrease the absolute interaction energy at the mutant's RGD site (Figure 2.11A). The stability of the RGD binding site enabled it to behave like a pivot point for mutated FN9-10 when FN9 dislodged from the synergy site. Since our data suggests that RGD remained stable regardless of synergy site engagement, we reasoned that the additional synergy site interaction energies in the wildtype would only bolster $\alpha_5\beta_1$-FN binding. From past in vitro experiments, RGD alone is known to be sufficient to support some $\alpha_5\beta_1$ integrin binding
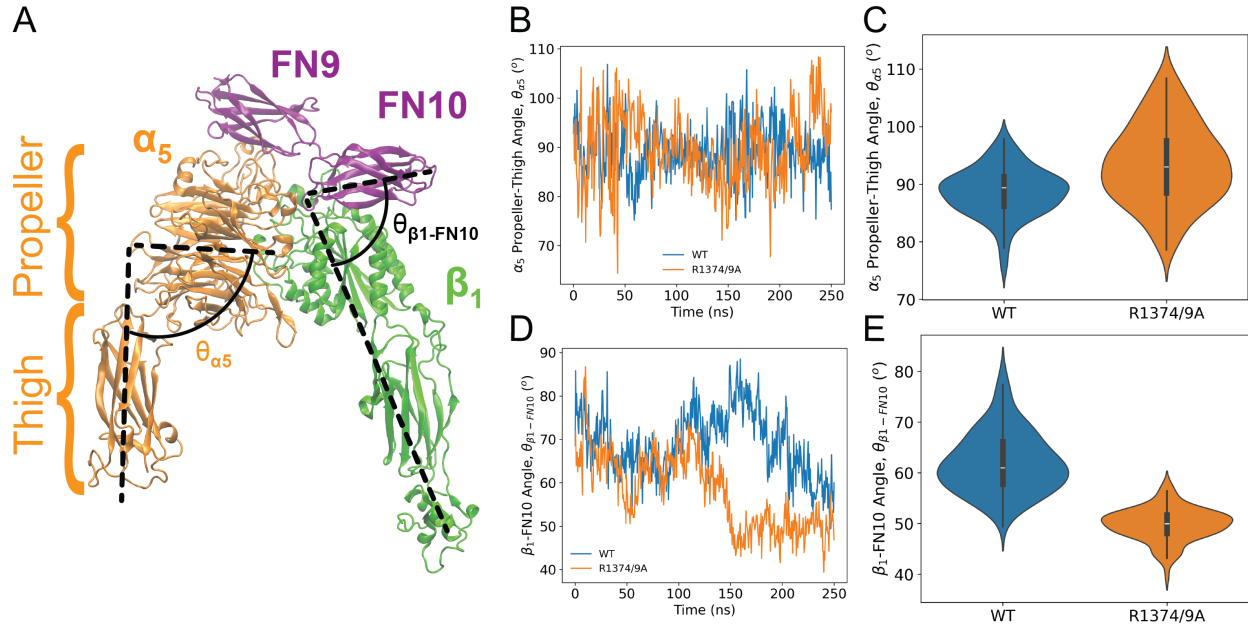
Figure 2.9: A) Cryo-EM structure of $\alpha_5\beta_1$-FN9-10 with the thigh propeller angle ($\theta_{\alpha5}$) and the β_1-FN10 angle ($\theta_{\beta1-FN10}$) labeled. B) Time series data of $\theta_{\alpha5}$. C) Violin plots of $\theta_{\alpha5}$ (WT = $88.7 \pm 4.2°$, R1374/9A = $93.4 \pm 6.8°$, $p = 0.3$). D) Time series data of $\theta_{\beta1-FN10}$. E) Violin plots of $\theta_{\beta1-FN10}$ (WT = $62.0 \pm 6.0°$, R1374/9A = $49.9 \pm 3.2°$, $p < 0.00001$).

and cell adhesion, though it has been shown that the synergy site promotes longer lasting binding and stronger cell adhesion when it binds in tandem with RGD to secure FN [28, 44]. The synergy site alone does not support cell adhesion as well as only RGD, or both RGD and the synergy site [4, 108], which may be attributed to the synergy site's lower nonbonded interaction energy (Figure 2.7C) compared to RGD (Figure 2.11A). However, as mentioned, free energy methods must be considered to include the entropic effects that we do not account for in this work.

Collectively, our observations of the 250ns NPT trajectories support the conjecture that the synergy site reinforces integrin engagement with the matrix [116, 44]. Further, our accelerated steered MD models imply that force between the synergy site and α_5 integrin head may induce conformational changes of α_5 integrin. Overall, our results highlight the importance of the synergy site clip in stabilizing and reinforcing the $\alpha_5\beta_1$-FN bond after initial catch bond formation, which has also been previously suggested experimentally [47, 128, 20, 10]. While cell adhesion can be negated altogether by an RGD deletion as demonstrated by spinning disk assays, the R1374/9A double mutation reduces cell adhesion strength by around 90% [44]. So, while adhesion could still occur, the bond strength was compromised due to the synergy site mutation, which has also been shown previously through single molecule AFM [78]. Additionally, past surface plasmon resonance binding assays measure an 11-fold decrease
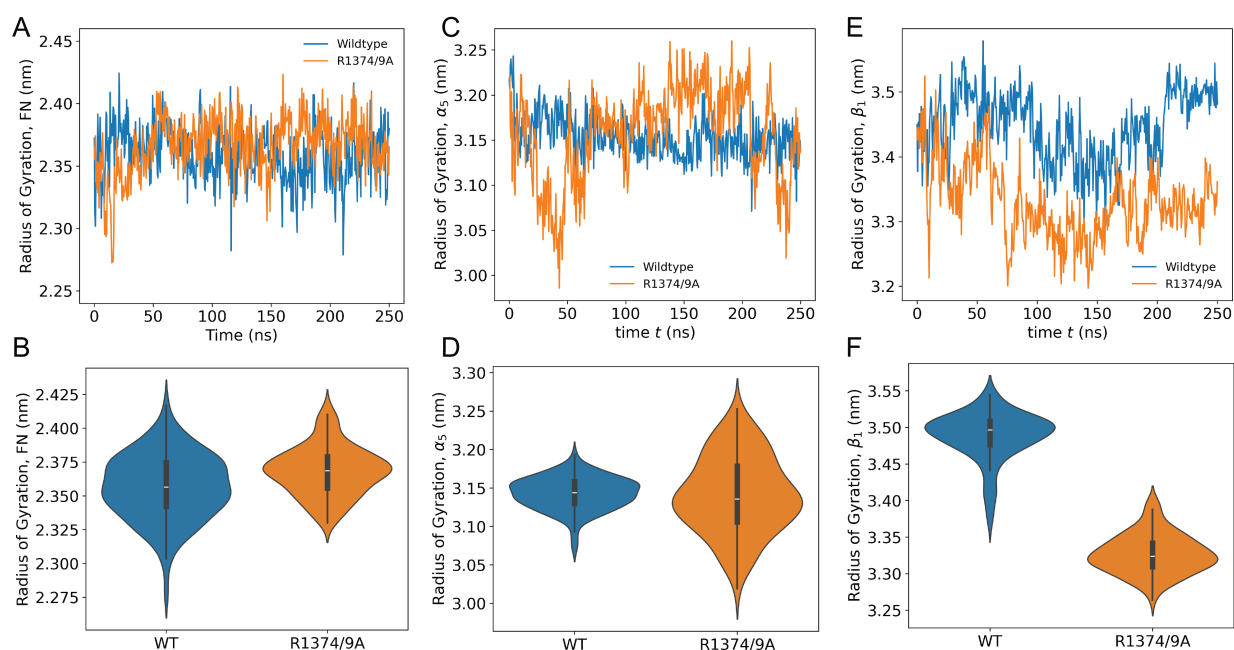
Figure 2.10: Time series data and violin plots of the radius of gyration of A-B) FN9-10 (WT = 2.36 ± 0.02nm, R1374/9A = 2.37 ± 0.02nm, $p = 0.0004$), C-D) the α_5 head (WT =3.14 ± 0.02nm, R1374/9A = 3.14 ± 0.05nm, $p = 0.73$), and E-F) the β_1 head (WT = 3.49 ± 0.03nm, R1374/9A =3.33 ± 0.03pm, $p < 0.00001$)
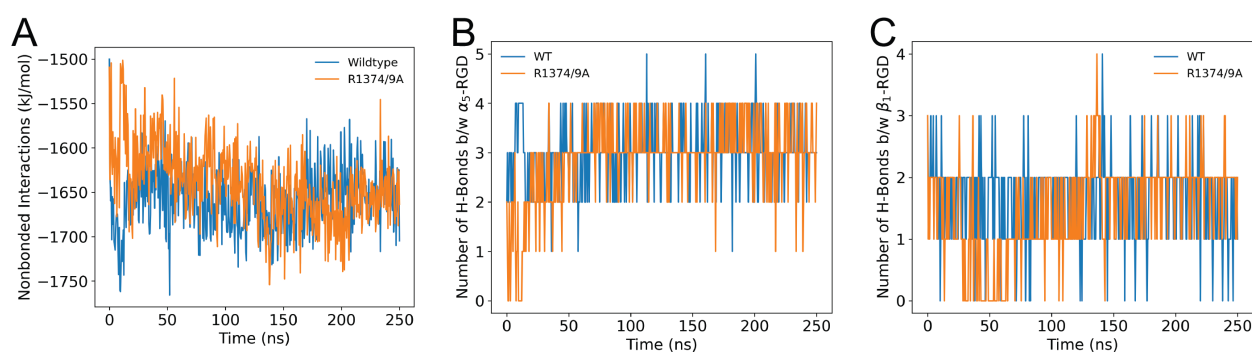
Figure 2.11: A) Nonbonded interactions at the RGD site which is the summation of the coulombic and van der waals energies for α_5-MIDAS, α_5-RGD, β_1-MIDAS, β_1-RGD, and RGD-MIDAS. B) Number of H-bonds between α_5 and RGD. C) Number of H-bonds between β_1 and RGD.
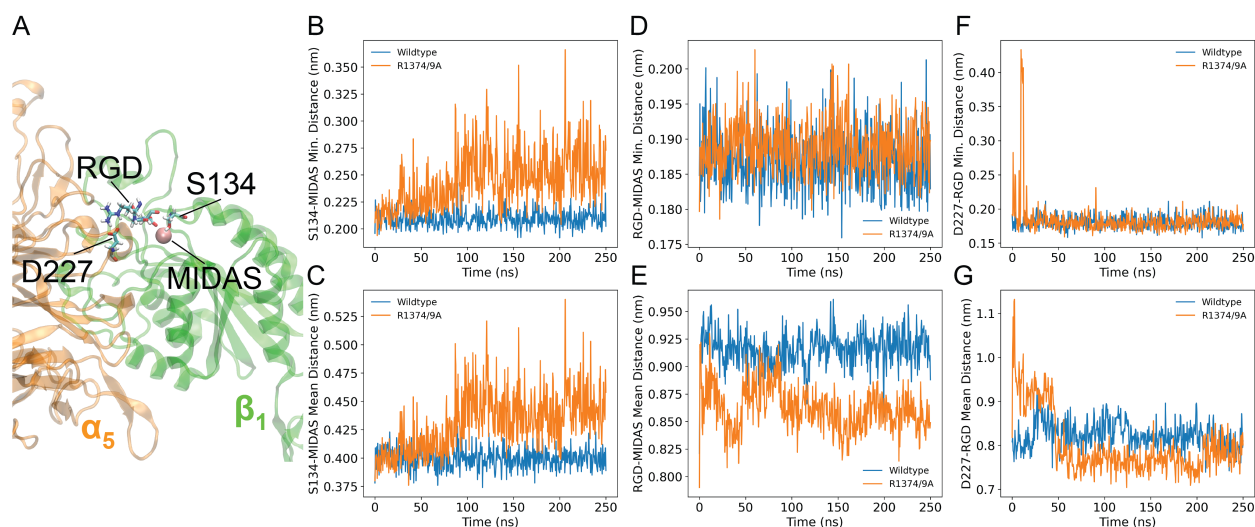
Figure 2.12: A) RGD site including key molecules such as RGD, S134, and D227, as well as the MIDAS coordination cation. Minimum and mean distances of B-C) S134-MIDAS, D-E) RGD-MIDAS, F-G) D227-RGD.

in affinity between $\alpha_5\beta_1$ and R1374A FN compared to wildtype [127]. Clearly, the role of the synergy site in maintaining a firm adhesion cannot be understated. Here, we propose how the synergy site may give rise to specific molecular states of $\alpha_5\beta_1$-FN, since it holds FN9 near α_5. Our steered MD models at a 1nm/ns pull rate showed a decrease in initial synergy site departure energy after mutagenesis, implying that there is a greater energetic barrier in breaking the synergy site than when it is inhibited. Further, the 1nm/ns wildtype model predicts that the connection between FN9-α_5 maintained by the synergy site could deform the α_5 head when loaded, which was not observed in the 1nm/ns mutant run. While our MD study highlighted the reinforcing role of the synergy site at the molecular scale, we also sought to explore how this adhesion reinforcement may dynamically manifest at the whole cell scale.

Pivot-clip mechanism of $\alpha_5\beta_1$-FN as a model for cell adhesion reinforcement

The mechanosensitive pivot-clip mechanism provides a model to consider how the $\alpha_5\beta_1$-FN catch bond reinforces cell adhesion across molecular and cell scales under cell-matrix forces (Figure 2.14). Long term NPT simulations indicated that role of the synergy site was to clip FN9 close to α_5 as evidenced by the increased separation between FN9 and α_5 in the mutant. The dislodging of FN9 did not modify the stability of the RGD site. In our steered MD simulations, for both pull rates tested in the wildtype $\alpha_5\beta_1$-FN, the unbinding of FN9-α_5

coincided with a plateauing of α_5 extension (Figures 2.3A and 2.6A). With the link between FN9-α_5 broken, FN10 was free to rotate about the RGD motif on β_1 (Figures 2.3D and 2.6D). The FN10 rotation about the RGD site was maintained in the mutant steered MD runs while diminishing the increase in radius of gyration of α_5 (Figure 2.6B and D). Based on the structural changes observed on α_5 in the steered MD simulations, the synergy site clipped the α_5 head to FN9 while the RGD motif on β_1 acted as a pivot for FN10 (Figure 2.14).

Since α_5 preferentially stretched instead of β_1, we conducted 100ns NPT simulations of each integrin head to measure each of their relative extensional stiffness. Upon confirming a stable RMSD after 50ns (Figure 2.13A), we averaged the measured α_5 and β_1 head distances over five 10ns blocks (Figure 2.13B) to quantify extensional stiffness. We measured extensional stiffnesses of 2587 pN/μm and 174548 pN/μm for the α_5 and β_1 heads, respectively (Figure 2.13C). Based on the distance fluctuations, β_1 remained more static, while α_5 seemed to oscillate. We also found that the propeller-thigh angle of α_5 decreased (Figure 2.13D), giving α_5 a more bent shape (Figure 2.13E). We reasoned that the link between the propeller and thigh grants α_5 its flexibility to stretch when force is applied, while β_1's rigidity could provide a route for forces to transmit towards cytoskeletal proteins. While it has been known that the synergy site plays a role in catch bond dynamics [44, 72], the clip engagement under force could be one mechanism by which the synergy site enables catch bond dynamics at the molecular scale. Using our pivot-clip model (Figure 2.14), forces generated at the cell-matrix interface would need to first overcome the synergy site clip energy barrier. In parallel, α_5 would resist forces by stretching prior to FN9 unclipping, also leading to a higher barrier than if the synergy site were not present. Additionally, the rigidity of β_1 could facilitate downstream mechanosignaling via talin. Namely, talin binds to the β_1 tail and has been shown to be a mechanosensitive protein that interacts with vinculin and focal adhesion kinase to promote focal adhesion maturation and nuclear localization of transcriptional coregulator, Yes-Associated Protein [146, 55, 25]. However, larger forces could also increase the probability of FN unbinding from $\alpha_5\beta_1$, especially when the additional energetic barrier from the synergy site is not present. Past assays have demonstrated that $\alpha_5\beta_1$-FN unbinding occurs with greater likelihood when the synergy site is inhibited; moreover, $\alpha_5\beta_1$-FN losing its catch bond characteristics [44, 122]. To determine the exact pathway of the force transmission across the $\alpha_5\beta_1$-FN catch bond with and without the synergy site, much longer and slower MD simulations are needed. Along those lines, more investigation is warranted to elucidate how the full structure of $\alpha_5\beta_1$ dynamically couples with mechanosensitive cytoskeletal proteins at the atomistic scale.

In the context of outside-in signaling, the $\alpha_5\beta_1$-FN pivot-clip mechanism demonstrates how the synergy site could route force via β_1 towards mechanosignaling proteins in the cytoplasm, like talin, leading to integrin clustering. According to the outside-in activation model, integrins maintain a bent-closed, low affinity state before undergoing a conformational change to an extended, active conformation upon encountering an ECM ligand (Figure 2.1A) [66, 117, 126]. In contrast, the inside-out model proposes that the adaptor protein talin would bind to the cytoplasmic tail of integrin, allowing it to activate and subsequently bind to its ligand [66, 117, 126]. While the current hypothesis states that binding between FN
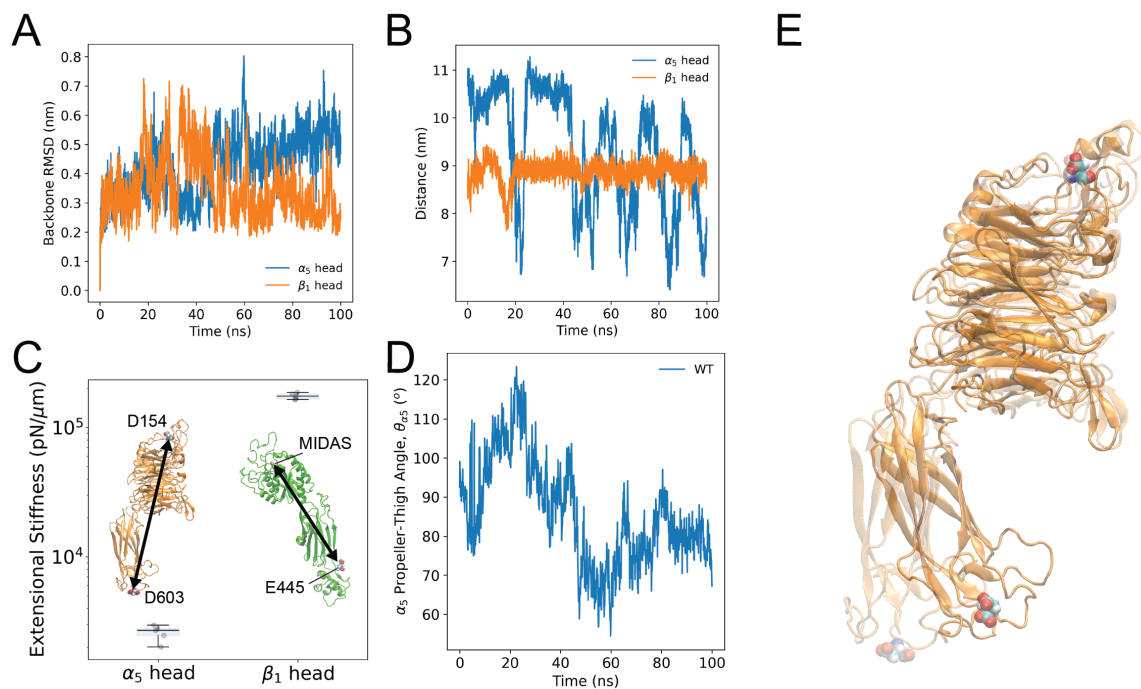
Figure 2.13: A) Backbone RMSD of independent α_5 and β_1 heads. B) Distance between D603 and D154 (α_5) and E445 and MIDAS (β_1). C) Extensional stiffnesses of α_5 and β_1 as measured by the respective reaction coordinates. D) Propeller-thigh angle on α_5. E) First (transparent) and last (opaque) frames of α_5 simulation. D603 (top) and D154 (bottom) are shown as references.

and $\alpha_5\beta_1$ triggers an opening of integrin's cytoplasmic tails leading to an accumulation of adaptor proteins that resist cell-matrix forces (Figure 2.14), further studies are needed to elucidate the mechanism behind integrin activation. Multiple steered MD models have been employed to interrogate β_3 integrin activation [36, 73, 23, 90, 123, 13], with few investigating the cytoplasmic end of β_1 integrin [67, 103]. However, to our knowledge, our approach is unique in that we model the interface between FN and the $\alpha_5\beta_1$ integrin heads, where forces are transmitted bidirectionally between the cell and its matrix.

Our study acknowledges several limitations. Firstly, we made the assumption that the proximal ends of the integrin heads were anchored by fully extended integrin legs tightly held by tails in the cell membrane. While this assumption contributed to model stability, it is worth noting that the head-leg junction has been suggested to possess greater flexibility [116]. Relaxing the constraints on the proximal ends to allow lateral movement may introduce flexibility without the added complexity of integrating the legs. Secondly, our steered MD models applied a large, vertical pulling rate. While this approach is advantageous for directly stressing the points of contact between FN and $\alpha_5\beta_1$, it could introduce biased pulling and

rotational forces that are unrealistic, which would decrease model confidence. Multiple runs and a parametric study of boundary conditions must be considered when confirming our MD simulations in future works investigating tension or other loading modalities, such as shear or torsion. Lastly, our focus was on a specific integrin subtype. The intricate nature of cell-matrix interactions involves multiple integrin subtypes and their respective ligands. Due to the prohibitive cost of molecular dynamics simulations, alternative approaches such as coarse-grained or agent-based models, capable of examining cell-matrix interactions at a broader systems level and over extended timescales, may be necessary.
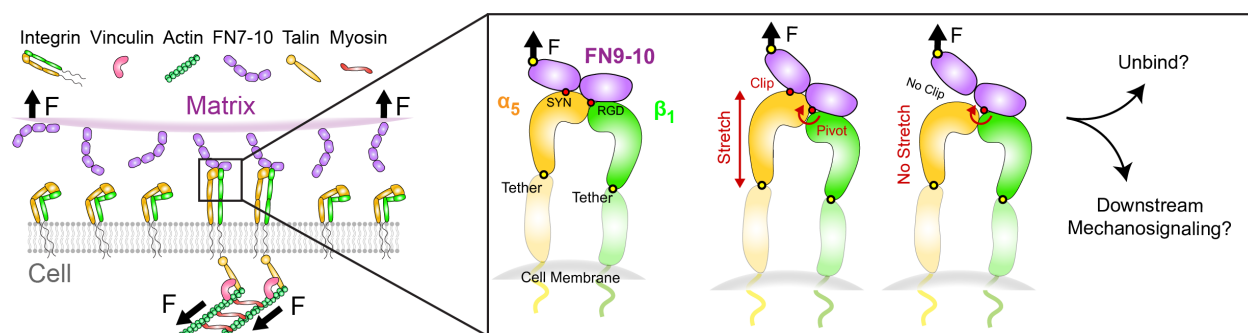
Figure 2.14: Proposed model for synergy site clip engagement leading to α_5 deformation during mechanosensing while RGD acts as a pivot for FN10. In this model, force transmits across the clip, stretching α_5. The additional energetic barrier provided by the clip could afford $\alpha_5\beta_1$-FN greater resistance to unbinding. The rigidity of β_1 relative to α_5 may allow for force transmission across the membrane and towards the mechanosensitive cytoskeletal protein, talin, leading to downstream mechanosignaling.

2.4   Conclusion

This work advances our understanding of cell mechanobiology by introducing a mechanosensitive mechanism, termed pivot-clip, by which $\alpha_5\beta_1$ integrin reinforces cell adhesion. Using MD simulations, we shed light on a biophysical connection between the cell and ECM that underpins many cellular behaviors that drive physiology and pathology. Critically, we also demonstrated binding domains that promote catch bond dynamics in the context of cell-matrix mechanosensing. Looking forward, we envision elucidating how the force-dependent, pivot-clip mechanism interacts with its surrounding machinery and how it may be transformed via novel therapeutics. As our understanding of cell adhesion progresses, we aim to develop informed approaches to target diseases that rely on transmitting forces via cell-matrix bonds.

Chapter 3

Dynamic $\alpha_5\beta_1$-FN Adhesion Collaboration

3.1 Introduction

In Chapter 2, we noted that the force transmission from $\alpha_5\beta_1$ integrin is only mildly affected after mutagenesis of the synergy site. However, past experiments demonstrated that mutating the synergy site diminishes catch bond behavior and weakens whole-cell and single molecule adhesion to $\alpha_5\beta_1$ [122, 44]. Even so, a lack of the synergy site does not significantly limit cell traction on a 2D substrate [20]. To explain how a perturbation of the synergy site may still allow $\alpha_5\beta_1$-FN binding while maintaining cell traction, we developed a 2D finite element (FE) model of the cell on a substrate. Based on these simulations, we present a working model that the synergy site in FN reinforces cell adhesion via a rebalancing of per-integrin forces due to a higher binding affinity.

3.2 Methods

Whole-cell Finite Element Model

We used a whole-cell FE model to calculate the $\alpha_5\beta_1$-FN concentration and force in a wildtype and mutant cell. We have previously modeled the cell-substrate interface using a whole-cell FE model; we refer the reader to that publication for the full set of model equations [91]. In the present work, we introduced key changes to the catch bond model. We modeled the cell as a 2D elastic disk with neo-Hookean constitutive material properties on a rigid substrate,

$$\boldsymbol{\sigma}_c^{pas} = \mu_c \mathbf{b}_c - p_c \mathbf{I}\,, \tag{3.1}$$

where σ_c^{pas} is the passive cell stress. The cell shear modulus is, μ_c=1kPa [84, 114]. The deformation was characterized by the left Cauchy-Green tensor $\mathbf{b}_c$. The pressure p_c was

computed from plane stress boundary conditions.

An isotropic active stress field was applied inside the cell to model cell contractility,

$$\boldsymbol{\sigma}_c^{act} = t_{myo}\mathbf{I}, \tag{3.2}$$

where $\boldsymbol{\sigma}_c^{act}$ is the active cell stress due to an actomyosin traction, t_{myo} in Pa [114, 22]:

$$t_{myo} = \begin{cases} 100t & 0 < t < 2 \\ 200 & 2 \le t \le 30 \end{cases} \tag{3.3}$$

where t is the simulation time.

We used an existing catch bond model of adhesion to calculate the force-dependent concentration of $\alpha_5\beta_1$-FN bonds per node in the FE mesh [52, 25, 9, 14]. The catch model assumed that the $\alpha_5\beta_1$-FN complexes behave as parallel springs that connect and disconnect to the substrate based on an association constant, K_{on} and on a force dependent dissociation constant, K_{off}, respectively.

$$K_{off} = K_a e^{\frac{f_{int}}{F_a}} + K_b e^{-\frac{f_{int}}{F_b}}, \tag{3.4}$$

where K_a, F_a, K_b, and F_b are fitted parameters (Table 3.1) adapted from Bidone et al [14] and Takagi et al [127]. f_{int} is the magnitude of the force per $\alpha_5\beta_1$-FN bond.

Table 3.1: Catch bond parameters for whole-cell finite element model

Variable	Wildtype	R1374/9A
K_{on}	$0.1\ s^{-1}$	$0.02\ s^{-1}$
K_a	$0.4\ s^{-1}$	$0.8\ s^{-1}$
K_b	$4E-7s^{-1}$	$8E-7s^{-1}$
F_a	$-25pN$	
F_b	$-15pN$	

The force vector per bond, ($\mathbf{f}_{int}$), is computed via the $\alpha_5\beta_1$-FN spring constant $k_{int} = 0.5$pN/nm [72] and the spring extension vector $\mathbf{u}_{int}$:

$$\mathbf{f}_{int} = k_{int}\mathbf{u}_{int}. \tag{3.5}$$

The force per node, $\mathbf{f}_{i,node}$ is related to the dimensionless concentration of $\alpha_5\beta_1$-FN bonds C with respect to the maximum bond density $\rho_{i,max} = 100\mu\text{m}^2$ [48], and the local adhesion area A at that node,

$$\mathbf{f}_{i,node} = C\rho_{i_{max}}A\mathbf{f}_{int}. \tag{3.6}$$

At any node, i given the previous value of the bond concentration, C, the updated bond concentration $C_{t+\Delta t}$ at each progressive time step is

$$C_{t+\Delta t} = C(1 - K_{off}\Delta t) + K_{on}\Delta t(1 - C). \tag{3.7}$$

Note that the updated eq. (3.7) is based on treating the bond kinetics in the limit of an ordinary differential equation discretized in time with an explicit Euler scheme.

The internal force balance for the cell includes the elastic cell deformation (σ_c^{pas}) and the active cell contractile stress (σ_c^{act}):

$$\nabla \cdot \boldsymbol{\sigma_c} + \mathbf{B} = \rho_c \mathbf{a}_c \,, \tag{3.8}$$

in which $\boldsymbol{\sigma_c} = \boldsymbol{\sigma_c^{pas}} + \boldsymbol{\sigma_c^{act}}$ is the total cell stress, $\mathbf{B}$ is the total body force on the cell, $\rho_c = 1000\text{kg/m}^3$ is the cell density [97] and $\mathbf{a}_c$ is the cell acceleration.

The strong form of the elastodynamic equation 3.8 has boundary conditions of the form $\boldsymbol{\sigma} \cdot n = t$ on boundary Γ_c, which includes the external forces on the circumference. Assuming 2D plane stress, the body forces on the cell arise from $\alpha_5\beta_1$-FN bond forces and viscous drag forces. The internal forces were computed through the weak form. Briefly, we multiplied equation 3.8 by test function, ν, integrated over a domain Ω_c of thickness 1μm, and applied divergence theorem to get the following weak form for the cell.

$$-\int_{\Omega_c} \boldsymbol{\sigma_c} : \delta\mathbf{d_c}\, d\Omega_c + \int_{\Gamma_c} \mathbf{t_c} \cdot \boldsymbol{\nu}\, dA_c + \int_{\Omega} \boldsymbol{\nu} \cdot \mathbf{B} = -\mathbf{R_c} + \mathbf{f_{circ}} + \mathbf{f_{body}} = \int_{\Omega_c} \rho\mathbf{a_c} \cdot \boldsymbol{\nu}\, d\Omega_c \,, \tag{3.9}$$

The $\delta\mathbf{d_c}$ is the variation of the symmetric velocity gradient, i.e. virtual work by moving each node by an independent variation ν. $\mathbf{R_c}$ is the residual (internal forces) and the external force acting at a node of the cell mesh is composed of the forces on the circumference, $\mathbf{f_{circ}}$ and the forces on the body, $\mathbf{f_{body}}$:

$$\mathbf{f_{circ}} = \mathbf{f}_\kappa + \mathbf{f}_{ac} + \mathbf{f}_A \,, \tag{3.10}$$

$$\mathbf{f_{body}} = \mathbf{f}_{i,node} + \mathbf{f}_d \,, \tag{3.11}$$

where $\mathbf{f}_{i,node}$ is the force due to $\alpha_5\beta_1$-FN at each node, $\mathbf{f}_d$ is viscous drag, $\mathbf{f}_\kappa$ is curvature regularization, $\mathbf{f}_{ac}$ is a random fluctuation at the cell boundary from actin polymerization, and $\mathbf{f}_A$ is an area penalty to counteract cell contractility.

More specifically, the viscous drag is

$$\mathbf{f}_d = -d\mathbf{u} \,, \tag{3.12}$$

where $\mathbf{u} = \mathbf{x}_{t+\Delta t} - \mathbf{x}$ is the displacement of the node and $d = 0.001\,\text{pN}/\mu\text{m}$ is a small drag coefficient. The curvature force is calculated only for nodes on the boundary. Discrete curvature κ is approximated based on twice the turning angle along the boundary curve divided by the length of the curve. Given the curvature, the force is

$$\mathbf{f}_\kappa = -k_\kappa \kappa \frac{l_b}{2}\mathbf{n} \,, \tag{3.13}$$

where **n** is the outward unit normal at the boundary and $k_\kappa = 20\text{pN}/\mu\text{m}$ is a small bending stiffness to prevent buckling and ruffling of the boundary, and l_b is the length of the edges incident at a node on the boundary. The actin polymerization fluctuation is also only at the boundary

$$\mathbf{f}_{ac} = f_{ac}\mathbf{n} \,, \tag{3.14}$$

where f_{ac} is a random force computed from sampling of a Poisson process. Specifically, an actin polymerization rate of $k_{ac} = 10\text{s}^{-1}$ was assumed [134]. The density of actin monomers near the boundary was estimated to be $\rho_{ac} \approx 100\text{monomer}/\mu\text{m}$ [41], and the individual monomer force to be 5pN [35]. To compute f_{ac}, we first determined the number of possible events at a node to be proportional to $n_{ac} = \rho_{ac}l_b/2$, where l_b is the length of the edges incident to the boundary node. Then, we performed a `for` loop over n_{ac} and for each iteration sampling a random number from $p_{ac}\,\mathcal{U}([0,1])$ and if $p_ac < k_{ac}\Delta t \exp(-k_{ac}\Delta t)$, we updated the actin force as $f_{ac} \leftarrow f_{ac} + 5\text{pN}$.

Finally, the area constraint is also only applied at the boundary nodes and it is

$$\mathbf{f}_A = -p_A(A_{tot} - A_0)\frac{l_b}{2}\mathbf{n} \,, \tag{3.15}$$

where A_{tot} is the entire area of the cell, A_0 is an attractor for the area, and the length of the curve associated with the node is l_b as before, just as the normal is also associated with the node and it is the outward unit normal as before. The strength of this constraint is imposed with the pressure parameter $p_A = 1\text{pN}/\mu\text{m}$. In reality the effects of the regularization terms is small but allows to keep the simulation stable and correspond to physically meaningful phenomena.

The mesh was updated by a dynamic explicit mesh generator, El Topo [16], during the simulation run. The explicit mid-point rule was used for time integration of the second order system of equations to update nodal velocities and positions. The triangular mesh is handled through the object `SurfTrack` part of the ElTopo library `https://github.com/tysonbrochu/eltopo`. Two `SurfTrack` objects are created, one for the cell mesh and one for the substrate mesh. The `SurfTrack` contains the nodal coordinates which we denote $\mathbf{x}_t$, the connectivity `tri_mesh`, and an additional connectivity which for every node stores the *one ring*, i.e. the nodes adjacent to a given node, which we refer to as `node_onering`. There is also a flag for nodes on the boundary of the surface. We modified the original library to also store nodal velocities, accelerations, and previous value of the strain. These vectors are named $\mathbf{v_t}$, $\mathbf{a}_t$, $\mathbf{e}_t$. For the cell mesh we also define one more vector field associated with the nodes, $\mathbf{u}_i$, that contains the displacement vector of a bond with respect to its stress-free state. Lastly, for the cell mesh we also store a scalar field C with the local integrin-bound fraction as described in the main text.

The integration is done explicitly with the midpoint rule. Given the current value of positions, velocities and accelerations, the midpoint velocity is calculated as

$$\mathbf{V}_{t+0.5\Delta t} = \mathbf{V}_t + \frac{\Delta t}{2}\mathbf{A}_t \,. \tag{3.16}$$

Then the the updated positions are computed as

$$\mathbf{X}_{t+\Delta t} = \mathbf{X}_t + \Delta t\mathbf{V}_{t+0.5\Delta t} \,. \tag{3.17}$$

Given the updated positions, the forces at the nodes are computed with the weak form. The whole-cell FE simulation ran with a time step of $50\mu s$ over the course of an assigned time of $t_{sim} = 30$s. There were a total of three simulation runs per R1374/9A mutant and wildtype catch bond condition, respectively. The three simulation bond concentration and force outputs were time-averaged per condition.

3.3   Results & Discussion

Synergy site presence led to adhesion reinforcement by recruiting $\alpha_5\beta_1$ integrin

We employed a whole-cell FE model that analyzed the adhesion interface that contained $\alpha_5\beta_1$-FN spring-like bonds under an isotropic cell contraction that drove bond extension (Figure 3.1).
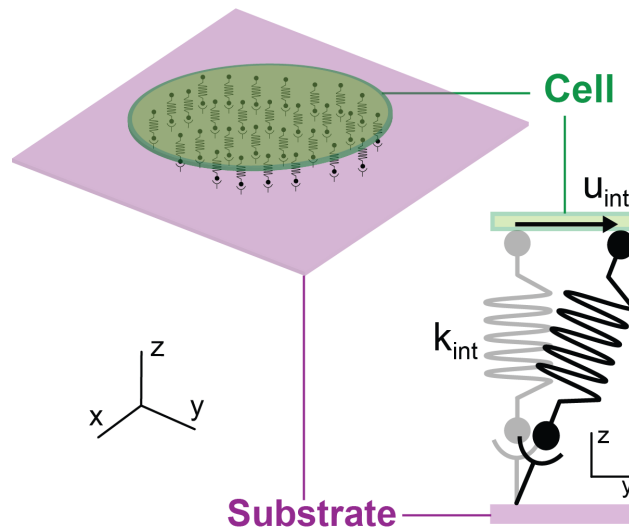
Figure 3.1: Schematic of whole-cell interface model that assumes that integrin behaves as a spring that is stretched due to cell contraction.

Our simple model demonstrated an adaptive reinforcement of collective $\alpha_5\beta_1$-FN bonds due to the stronger binding affinity afforded by the synergy site. We modified the parameters

for the $\alpha_5\beta_1$-FN binding kinetics to produce bond lifetime curves for the wildtype bond and R1374/9A mutant (Figure 3.2A). The differences in parameters between the two bond types resulted in an 11-fold decrease in $\alpha_5\beta_1$-FN bond concentration (Figure 3.2B), but no increase in equilibrium force (Figure 3.2C). The areas of high concentrations and high forces are present at the periphery of the cell during contraction (Figures 3.3 and 3.4), which has been shown by 2D Fluorescence Resonance Energy Transfer (FRET) and traction force microscopy (TFM) assays [20]. Notably, mutant bonds compensate for the lack of number of bonds by sustaining more of the cell's contractile load. The higher recruitment of wildtype bonds distributes the forces more evenly across the cell.
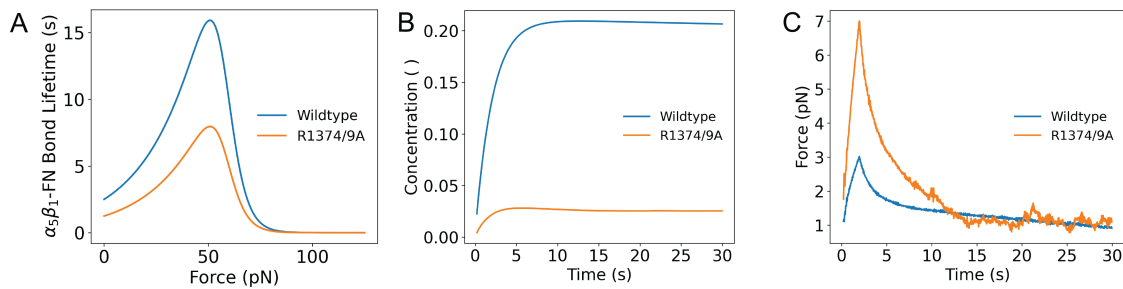
Figure 3.2: A) Catch bond model: $\alpha_5\beta_1$-FN bond lifetime versus applied force for wildtype (adapted from [14, 127]). B) Concentration over time of wildtype and mutant $\alpha_5\beta_1$-FN. C) Force over time of wildtype and mutant $\alpha_5\beta_1$-FN.

Our whole-cell FE model sheds light on the dynamic force balance at short timescales that are not as apparent experimentally. TFM of cells plated on 2D substrates have shown that cell contraction and individual bond force were not altered due to an absence of the synergy site [20, 128]. Our model used the same 200Pa cell contraction across both conditions, but showed a stark difference in how the adhesion forces are handled by the bonds. Namely, while forces eventually equalized between mutant and wildtype conditions, we observed an initial dynamic adjustment of high forces at the cell boundary for mutant bonds (Figure 3.4). Specifically, average forces measured from mutated bonds peaked at 7pN, while wildtype bonds peaked at 3pN; both average bond forces were within the previously measured 1-7pN range [20]. A body of work has shown the reduction in cell adhesion strength at the single molecule and whole cell scale due to a lack of synergy site engagement [20, 128, 44, 78]. In spite of the reduced bond strength, our work showed that the binding affinity gain due to the presence of the synergy led to a more stable, dynamic force balance across the $\alpha_5\beta_1$-FN bonds on the cell surface.
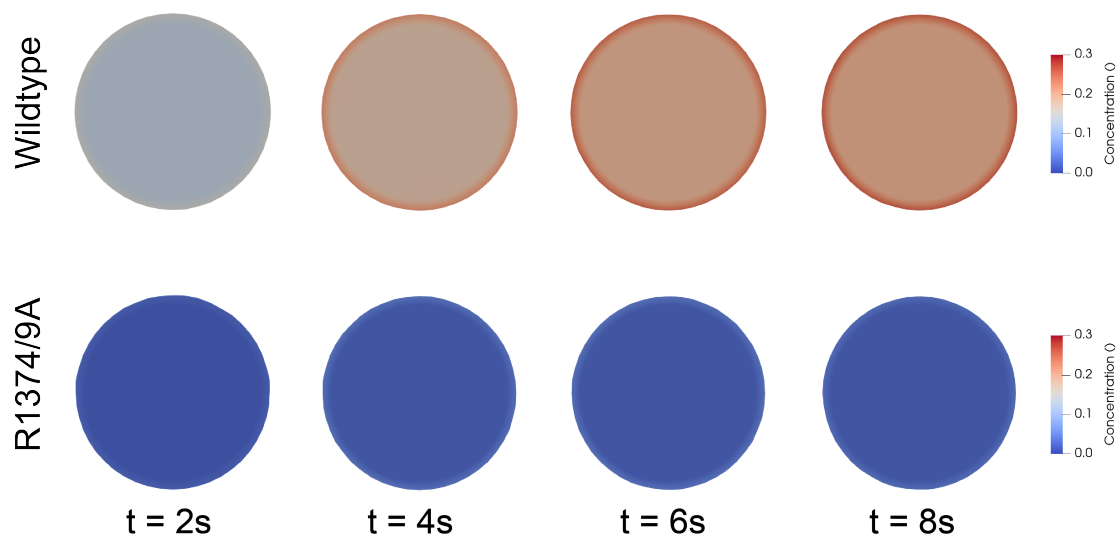
Figure 3.3: Frames at times 2, 4, and 6s indicating the concentration of $\alpha_5\beta_1$-FN bonds across the cell-substrate interface during a 200Pa uniform contraction.
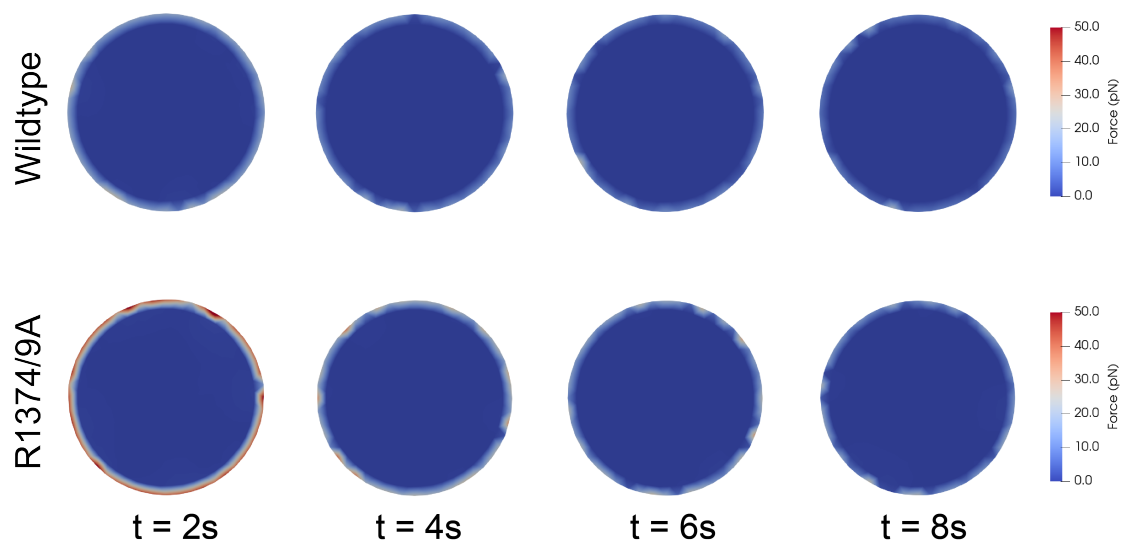
Figure 3.4: Frames at times 2, 4, and 6s indicating the distribution of $\alpha_5\beta_1$-FN bond force across the cell-substrate interface during a 200Pa uniform contraction.

Chapter 4

Bridging Simulations of $\alpha_5\beta_1$-FN Across Scales

Integrin mechanosensing plays an instrumental role in cell behavior, phenotype, and fate by transmitting mechanical signals that trigger downstream molecular and cellular changes. For instance, force transfer along key amino acid residues can mediate cell adhesion. Disrupting key binding sites within $\alpha_5\beta_1$ integrin's binding partner, fibronectin (FN) diminishes adhesive strength. While past studies have shown the importance of these residues in cell adhesion, the relationship between the dynamics of these residues and how integrin distributes force across the cell surface remains less explored. Here, we present a multiscale mechanical model to investigate the mechanical coupling between integrin nanoscale dynamics and whole-cell adhesion mechanics. Our framework leverages molecular dynamics simulations to investigate residues within $\alpha_5\beta_1$-FN during stretching and the finite element method to visualize the whole-cell adhesion mechanics. The forces per integrin across the cell surface of the whole-cell model were consistent with past atomic force microscopy and Förster resonance energy transfer measurements from literature. The molecular dynamics simulations also confirmed past studies that implicate two key sites within FN that maintain cell adhesion: the synergy site and RGD motif. Our study contributed to our understanding of molecular mechanisms by which these sites collaborate to mediate whole-cell integrin adhesion dynamics. Specifically, we showed how FN unfolding, residue binding/unbinding, and molecular structure contribute to $\alpha_5\beta_1$-FN's nonlinear force-extension behavior during stretching. Our computational framework could be used to explain how the dynamics of key residues influence cell differentiation or how uniquely designed protein structures could dynamically limit the spread of metastatic cells.

4.1 Introduction

Cell-matrix junctions, governed in part by macromolecular structures known as focal adhesions (FAs), can alter cell phenotype, behavior, and fate via applied mechanical signals that trigger downstream molecular and cellular changes [64, 66, 147, 59, 107, 126, 92, 33, 76]. At the

heart of FA formation is a transmembrane heterodimer known as integrin containing α- and β- subunits. Normally, nascent FAs initiate with integrin activation, where cytoplasmic proteins bind to the integrin tails and the integrin head extends to an active state with a higher affinity for ligand binding [66, 93]. However, the activation of a particular integrin, $\alpha_5\beta_1$ appears to follow a separate mechanism where an extended conformation may not be required to bind to its primary ligand, fibronectin (FN) [127, 116]. Instead, $\alpha_5\beta_1$ binds to FN before cytoplasmic proteins anchor it to the cytoskeleton and additional integrins cluster together to create a mature FA (Fig. 4.1A).

The connection between $\alpha_5\beta_1$ integrin and FN is a main mechanosensing unit for external forces transmitting along amino acid residues that mediate cell adhesion [116]. The two principal $\alpha_5\beta_1$ binding sites in FN include the 8-amino-acid-long DRVPHSRN synergy site and the RGD motif [96, 139, 116]. Upon mutation of R1374 and R1379 within the synergy site, spinning disk assays showed a reduction in cell-substrate adhesion strength; moreover, a perturbation of FN's RGD motif inhibited adhesion altogether [44]. While the synergy site and RGD motif have been shown to play a role in cell adhesion, their nanoscale dynamics and force transduction pathway are less resolved. Elucidating how these residues maintain cell adhesion during integrin mechanosensing is important because their nanomechanics could be leveraged to control cell phenotype or motility.

Notably, $\alpha_5\beta_1$'s predominant role in mediating cell adhesion lends itself to be instrumental in the progression of various pathologies. For example, imposing a fibrotic microenvironment on cells by depositing fibronectin or collagen-I or by applying biomechanical forces to the cancer cells leads to greater $\alpha_5\beta_1$ integrin-mediated proliferation [6, 71]. Similarly, as a tumor's rigidity increases, mechanosensitive $\alpha_5\beta_1$ integrins are recruited and cluster together, creating larger FAs and stress fibers that promote tumor growth via a positive biochemical and biophysical feedback loop [106, 100]. By understanding the link between nano and micromechanics of the cell, we could influence differentiation or mitigate the uncontrolled spread of metastatic cells through targeted protein or drug design.

Therefore, to uncover the mechanical coupling between the nanoscale dynamics of key residues in $\alpha_5\beta_1$ integrin and whole-cell adhesion dynamics, we built a multiscale model. Specifically, we combined adhesion kinetics, the finite element (FE) method, and molecular dynamics (MD) to demonstrate how key residues contributed to spring-like force-extension behavior which in turn influenced the whole-cell spatial distribution of forces on integrins (Fig. 4.1B). The force per integrin results from our model were within those measured by past atomic force microscopy (AFM) [78] and Förster resonance energy transfer (FRET) measurements [20]. The model indicated localization of $\alpha_5\beta_1$ integrin along the cell periphery, which is consistent with cell-based studies that stain for β_1 integrin and FN fragments [10]. Most importantly, the model contributed an inside look at the molecular dynamics by which the DRVPHSRN synergy site and RGD motif work together to mediate whole-cell adhesion mechanics.
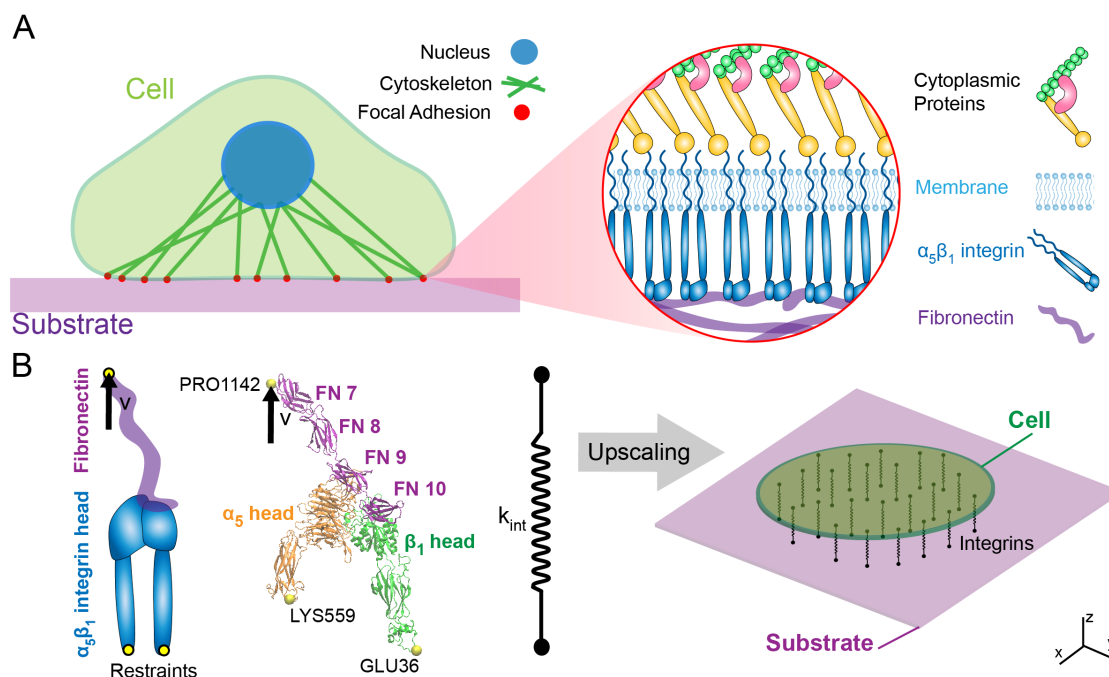
Figure 4.1: Simplified schematic of multiscale cell mechanobiology within cell adhesion mediated by $\alpha_5\beta_1$ integrin (A) The cell attaches to a substrate via FAs which house multiple biomolecules including cytoplasmic proteins that anchor integrins to corresponding ligands. (B) The molecular assembly consisted of $\alpha_5\beta_1$ integrin head bound to fibronectin type III fragment 7-10. For the MD simulations, restraints were placed on GLU36 and LYS559 with an applied velocity at PRO1142. The $\alpha_5\beta_1$-FN's stretching behavior was characterized by a spring that was applied to a 2D continuum model of an elastic cell on a substrate.

4.2 Methods

All-atom Steered Molecular Dynamics

The 7NWL.pdb file containing human $\alpha_5\beta_1$ integrin in complex with FN and TS2/16 Fv-clasp was downloaded from the Protein Data Bank [116]. Schumacher et al. used the TS2/16 Fv-clasp to aid in the crystallization of $\alpha_5\beta_1$-FN and is not naturally occurring and was therefore removed using PyMOL 2.5[115], leaving three protein chains to be analyzed as part of the remaining complex: α_5 integrin, β_1 integrin, and FN type III. We refer to this complex, or system as "$\alpha_5\beta_1$-FN."

All-atom molecular dynamics (MD) simulations were run in GROMACS 2018.3 [1] with the AMBER99SB-ildn force field and periodic boundary conditions. Using the Gromacs built-in function, `gmx editconf`, we rotated the $\alpha_5\beta_1$-FN complex 45 degrees to align the structure inside a 18nm x 45nm x 19nm box. The structure was solvated in a TIP3P water
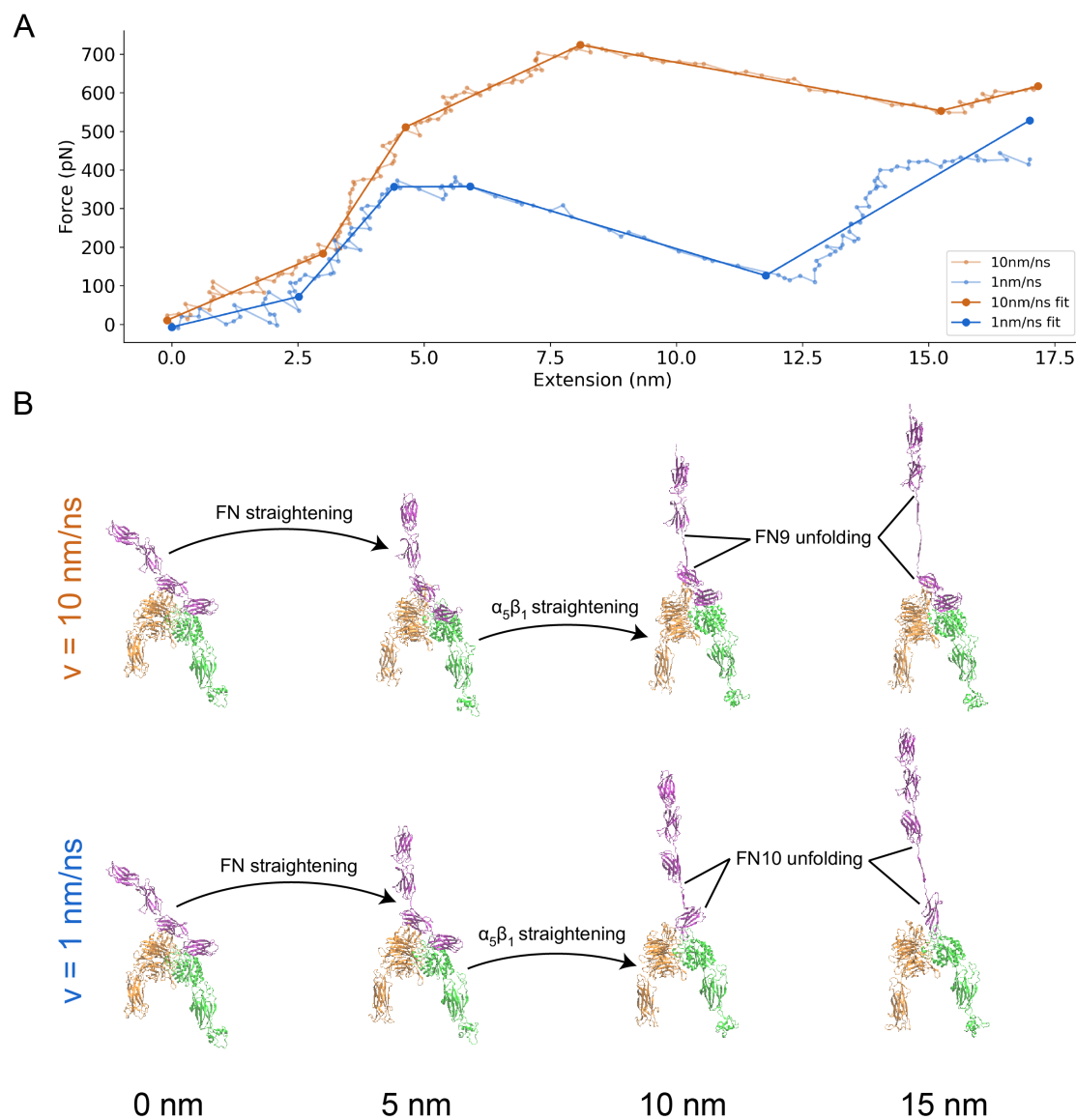
Figure 4.2: (A) Force-extension curve of $\alpha_5\beta_1$-FN stretching at 10 and 1 nm/ns. The raw data are shown in transparent solid lines and the 5-segment piecewise linear fits are shown in opaque solid lines. (B) Frames of $\alpha_5\beta_1$-FN during extension at 10 nm/ns and 1 nm/ns showing distinct stretching configurations at 0, 5, 10, and 15 nm of extension. In both cases, FN and $\alpha_5\beta_1$ straightened before FN unfolded. However, for the 10 nm/ns case, the FN9 subdomain unfolded. Whereas for the 1 nm/ns case, FN10 unfolded.

box with 0.15mM NaCl resulting in a system with 1.5 million atoms.

The energy minimization step was carried out for 15k steps utilizing the steepest gradient

descent algorithm with a step size of 0.005nm (Table 4.2).

Table 4.1: Energy Minimization Parameters

Parameter	Setting
Algorithm	Gradient descent
Energy tolerance	10 kJ/mol/nm
Energy step size	0.005nm
Number of steps	15000
Neighbor list update frequency	1 step
Cutoff scheme	Verlet
Method to determine neighbor list	Grid
Short range force cut-off for neighbor list	1.4nm
Electrostatics	Fast smooth Particle-Mesh Ewald (SPME)
Short-range electrostatic cut-off	1.4nm
Short-range Van der Waals cut-off	1.4nm

Energy over time was extracted using the `gmx energy` command and then plotted in Python. The structure was then equilibrated using a sequential 1ns NVT followed by a 10ns NPT simulation with H-bonds restrained. For the NVT simulation, we used Nose-Hoover temperature coupling at 310K. For the NPT simulation, Parrinello-Rahman pressure coupling at 1 bar was added. After the equilibration runs were completed, we extracted and plotted the root-mean-square deviation (RMSD), temperature, and pressure to confirm system stability. Upon verifying system equilibration, we ran two steered MD simulations. The positions of Lysine (LYS) 559 and glutamic acid (GLU) 36 at the proximal ends of the integrin headpieces were restrained using the `gmx genrestr` command (Fig. 4.1B). Proline (PRO) 1142 at the distal end of the FN chain was pulled vertically at 1 and 10 nm/ns using a 50kJ/mol/nm spring with an umbrella potential for 25 and 3 ns, respectively. Constant force simulations were ran with vertical pulling forces of 300 and 500 pN on PRO1142. The simulations only model the $\alpha_5\beta_1$ integrin headpiece and assume that the lower legs of $\alpha_5\beta_1$ and cell membrane, which are omitted, fix the positions of the headpieces at the proximal end. The model also assumes a completely vertical pulling load stemming from cell and substrate displacement and ignores any shear or rotational loads. The timestep for all steered MD simulations was 2fs. The Molecular Dynamics Parameter (.mdp) files for running the energy minimization, equilibration, and steered MD can be found in `https://github.com/dredremontes/pull_integrinMD`. We used the Gromacs built-in function `gmx gyrate` to measure the radius of gyration of the α_5 and β_1 integrin heads.

Force Distribution Analysis

Protein structures and MD simulation trajectories were visualized in Visual Molecular Dynamics (VMD) 1.9.4a [61]. We then used the Time-Resolved Force Distribution Analysis

(FDA) software package, gromacs-fda (`https://github.com/HITS-MBM/gromacs-fda`) with Gromacs 2020.4 to calculate the punctual stresses at each of the residues along the α_5 and β_1 integrin chains, as well as FN. The punctual stress is the sum of absolute values of scalar pairwise forces exerted on each residue. The parameter settings for the FDA can be found in Table 4.2. The gromacs-fda-vmd plugin overlaid the punctual stress heatmap onto the protein renderings in VMD. Areas of interest for the FDA were the DRVPHSRN synergy site and RGD motif/loop (Fig. 4.3).

Table 4.2: Force Distribution Analysis Parameter Settings

Parameter	Setting
Pairwise forces	Summed
Pairwise groups	Protein
Residue based calculation	Punctual Stress
Pairwise force type	Coulombic interactions only
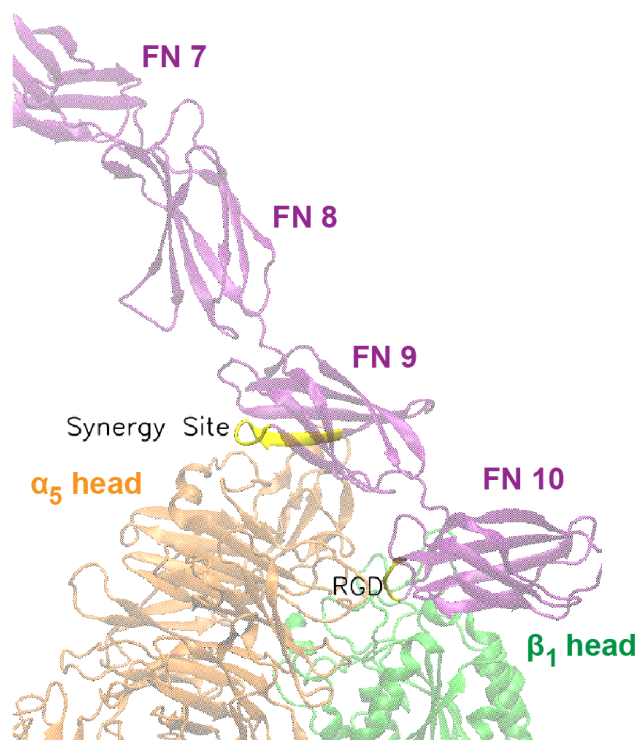
Figure 4.3: Close up view of DRVPHSRN synergy site and RGD motif/loop (shown in yellow) in FN that interact with the α_5 and β_1 heads, respectively.

Whole-Cell Finite Element Model

Building on the model in Chapter 3, the model again represented the cell as a thin elastic disk on top of an elastic substrate. The cell surface was assumed to be a neo-Hookean [132] constitutive material model, but this time considered the substrate as a Neo-Hookean material.

$$\sigma_s^{pas} = \mu_s \mathbf{b}_s - p_s \mathbf{I}, \tag{4.1}$$

$$\sigma_c^{pas} = \mu_c \mathbf{b}_c - p_c \mathbf{I}, \tag{4.2}$$

where σ_s^{pas} and σ_c^{pas} are the passive substrate and cell stress respectively. The shear moduli are denoted μ_s, μ_c (Table 4.3). The deformation is characterized by the left Cauchy-Green tensors $\mathbf{b}_s$, $\mathbf{b}_c$. The pressures p_s, p_c are computed from boundary conditions, in this case for plane stress, ignoring 3D deformations.

Table 4.3: Whole-cell Model Parameter Settings

Parameter	Variable	Setting
Substrate modulus	μ_s	1 MPa
Substrate density	ρ_s	1.0 μg/μm^3
Cell modulus	μ_c	1 kPa
Cell density	ρ_s	1000 kg/m^3
Max $\alpha_5\beta_1$-FN density	$\rho_{i_{max}}$	100μm^{-2}
	K_a	0.004 s^{-1}
Catch-slip bond parameters	K_b	10s^{-1}
	F_a	15pN
	F_b	15pN

To account for cell contractility, an active stress field was applied inside the cell,

$$\sigma_c^{act} = t_{myo} \mathbf{I}, \tag{4.3}$$

where σ_c^{act} is the active cell stress due to the applied actin-myosin traction, t_{myo} (Pa):

$$t_{myo} = \begin{cases} 100t & 0 < t < 2 \\ 200 & 2 \leq t \leq 12 \end{cases} \tag{4.4}$$

where t is the simulation time. We used a previously developed catch-slip bond model of adhesion to determine the number of integrin-substrate bonds per node in the FE mesh in a force dependent manner [52, 25]. This model assumes that the $\alpha_5\beta_1$-FN complexes behave as parallel springs that connect and disconnect to the substrate based on an association constant, K_{on} and on a force dependent dissociation constant, K_{off}, respectively.

$$K_{off} = K_a e^{\frac{f_{int}}{F_a}} + K_b e^{-\frac{f_{int}}{F_b}}, \tag{4.5}$$

where K_a, F_a, K_b, and F_b are fitted parameters (Table 4.3) and f_{int} is the magnitude of the force per $\alpha_5\beta_1$-FN bond. The force vector per bond, ($\mathbf{f}_{int}$), is computed via the $\alpha_5\beta_1$-FN spring constant k_{int} and the spring extension vector $\mathbf{u}_{int}$:

$$\mathbf{f}_{int} = k_{int}\mathbf{u}_{int}. \tag{4.6}$$

The force per node from integrin and is related to the fraction (concentration) of $\alpha_5\beta_1$-FN bonds C with respect to the maximum density $\rho_{i,max}$ (Table 4.3), the local area of the adhesion A (area per node of the FE mesh), at that node,

$$\mathbf{f}_{i,node} = C\rho_{i_{max}}A\mathbf{f}_{int}. \tag{4.7}$$

The fraction of $\alpha_5\beta_1$-FN bonds C needs to be updated in time. For a given node,i given the previous value of the bond concentration, C, the updated bond concentration $C_{t+\Delta t}$ at each subsequent time step is based on the update

$$C_{t+\Delta t} = C(1 - K_{off}\Delta t) + K_{on}\Delta t(1 - C). \tag{4.8}$$

Note that the update eq. (4.8) is based on treating the bond kinetics in the limit of an ordinary differential equation discretized in time with an explicit Euler scheme.

The internal force balance for the cell and substrate include elastic deformation of the cell (σ_c^{pas}), active contractile stress within the cell (σ_c^{act}), and elastic deformation of the substrate (σ_s^{pas}):

$$\nabla \cdot \sigma_c = \rho_c\mathbf{a}_c \tag{4.9}$$
$$\nabla \cdot \sigma_s = \rho_s\mathbf{a}_s \tag{4.10}$$

where $\sigma_\mathbf{c} = \sigma_\mathbf{c}^{\mathbf{pas}} + \sigma_\mathbf{c}^{\mathbf{act}}$ is the total stress in the cell, $\sigma_\mathbf{s} = \sigma_\mathbf{s}^{\mathbf{pas}}$ is the total stress in the substrate, ρ_c, ρ_s are the densities of cell and substrate respectively (Table 4.3), and $\mathbf{a}_c, \mathbf{a}_s$ the corresponding accelerations.

The strong forms of the elastodynamic equations 4.9 and 4.10 have boundary conditions of the form $\sigma \cdot n = t$ on boundary Γ. The strong forms are not directly evaluated. Rather, the internal forces were computed through the weak form. We multiplied both elastodynamic equations separately by test function, ν, integrated over a domain Ω of thickness 1μm, and applied divergence theorem to get the following weak form for the cell (subscript c) and substrate (subscript s), respectively.

$$-\int_{\Omega_c} \sigma_\mathbf{c} : \delta\mathbf{d_c}\, d\Omega_c + \int_{\Gamma_c} \mathbf{t_c} \cdot \delta\nu_\mathbf{c}\, dA_c = -\mathbf{R_c} + \mathbf{f}_{c,ext} = \int_{\Omega_c} \rho\mathbf{a_c}\, d\Omega_c \tag{4.11}$$

$$-\int_{\Omega_s} \sigma_\mathbf{s} : \delta\mathbf{d_s}\, d\Omega_s + \int_{\Gamma_s} \mathbf{t_s} \cdot \delta\nu_\mathbf{s}\, dA_s = -\mathbf{R_s} + \mathbf{f}_{s,ext} = \int_{\Omega_s} \rho\mathbf{a_s}\, d\Omega_s \tag{4.12}$$

The $\delta\mathbf{d}$ is the variation of the symmetric velocity gradient, i.e. virtual work by moving each node by an independent variation $\delta\nu$. $\mathbf{R}$ is the residual and the external force acting at a particular node of the respective cell and substrate meshes is:

$$\mathbf{f}_{c,ext} = \mathbf{f}_{i,node} + \mathbf{f}_d + \mathbf{f}_\kappa + \mathbf{f}_{ac} + \mathbf{f}_A \tag{4.13}$$

$$\mathbf{f}_{s,ext} = -\mathbf{f}_{i,node} + \mathbf{f}_d \tag{4.14}$$

where $\mathbf{f}_{i,node}$ is the force due to $\alpha_5\beta_1$-FN at each node, $\mathbf{f}_d$ is viscous drag, $\mathbf{f}_\kappa$ is curvature regularization, $\mathbf{f}_{ac}$ is a random fluctuation at the cell boundary from actin polymerization, and $\mathbf{f}_A$ is an area penalty to counteract cell contractility. Note that the nodal $\alpha_5\beta_1$-FN force acts on the cell and substrate surfaces in opposite directions. The remaining variables act on the cell border.

Given the force in the cell or the substrate, $\mathbf{f}_{ext}$, the acceleration is updated by:

$$\mathbf{a}_{t+\Delta t} = \mathbf{M}^{-1}(\mathbf{f}_{ext} - D\mathbf{M}\mathbf{v}_{t+0.5\Delta t}) \tag{4.15}$$

with $\mathbf{M}$ being the respective diagonal mass matrix and a damping coefficient of $D = 0.001$ 1/s. Lastly, the velocities are updated

$$\mathbf{v}_{t+\Delta t} = \mathbf{v}_{t+0.5\Delta t} + \frac{\Delta t}{2}\mathbf{a}_{t+\Delta t} \,. \tag{4.16}$$

One additional set of updates in the model is the change of the displacement of the integrin-ligand pair $\mathbf{u}_i$ as the cell and substrate deform. From the cell deformation, the update is

$$\mathbf{u}_i \leftarrow \mathbf{u}_i + \mathbf{u}_{cell} \,, \tag{4.17}$$

where $\mathbf{u}_{cell} = \mathbf{x}_{t+\Delta t} - \mathbf{x}_t$ is the corresponding displacement of the node on the cell. For the substrate, since the $\mathbf{u}_i$ is associated with the nodes of the cell mesh, we first get the triangle in the substrate mesh this corresponds to and then update

$$\mathbf{u}_i \leftarrow \mathbf{u}_i - \mathbf{u}_{subs} \,, \tag{4.18}$$

where $\mathbf{u}_{subs}$ is the interpolated displacement of the substrate at the correct location of the node from the cell mesh. Because when forms break and new bonds form they are not assumed to be pre-strained, there is some dissipation associated with this drift in the reference configuration of the bond stretch, captured by

$$\mathbf{u}_i \leftarrow \mathbf{u}_i(C_t - \Delta t K_{off} C_t)/C \tag{4.19}$$

which reduces the stretch in the $\alpha_5\beta_1$-FN proportional to the number of broken bonds with respect to the previous bond fraction C_t. If $C_t - \Delta t K_{off} C_t \leq 0$ then the stretch of the bonds is set to $\mathbf{0}$.

A dynamic explicit mesh generator, El Topo [16], created and maintained the mesh during the simulation run. Three $\alpha_5\beta_1$-FN stiffness values (k_{int}) were used: 1pN/nm, 31pN/nm, and variable stiffnesses extracted from the MD simulation force-extension curves (MD-driven). The variable stiffness of the $\alpha_5\beta_1$-FN complex within the FE model was modeled as a nonlinear spring by applying piece-wise linear interpolation in Python to the force-extension curves provided by the MD simulations as described in Section 4.2.

The overall sequence of the multiscale model is summarized in Figure 4.7. To summarize, the whole-cell FE model first imports the cell and substrate meshes and calculates the velocities and positions of the nodes. The $\alpha_5\beta_1$-FN bonds are spread out uniformly across the surface of the cell with bond attachment points on the cell and the substrate. The displacement between the cell and substrate attachment points dictate the bond stretch. For the MD-driven case, the bond stiffness, k_{int} is assigned based on the bond stretch. Otherwise, the stiffness is directly assigned according to each constant case (k_{int}=1 or 31 pN/nm). The force per bond is then calculated via Hooke's Law (eq. 4.6). This force is then used to update two things: the force per node (eq. 4.7) and the bond kinetics (eqs. 4.5 and 4.8). Cell contraction (eqs. 4.3 and 4.4) is then applied and the residual is computed via the weak form (eq. 4.11 and 4.12) considering the cell and substrate respective material properties (eq. 4.1 and 4.2), their elastodynamics (eqs. 4.9 and 4.10), and their force balances (eqs. 4.13 and 4.14). The nodal strains, velocities, and positions are updated and lastly, the simulation frame is saved. The whole-cell FE simulation iterates with a 1000-element mesh and a timestep of $dt = 50\mu s$ over the course of an assigned time, $t_{sim} = 12s$. Mesh (Fig. 4.4 - 4.5) and timestep (Fig. 4.6) convergence was run to arrive at these settings. The code to run these simulations is available in: `https://github.com/dredremontes/wholeCellFE`
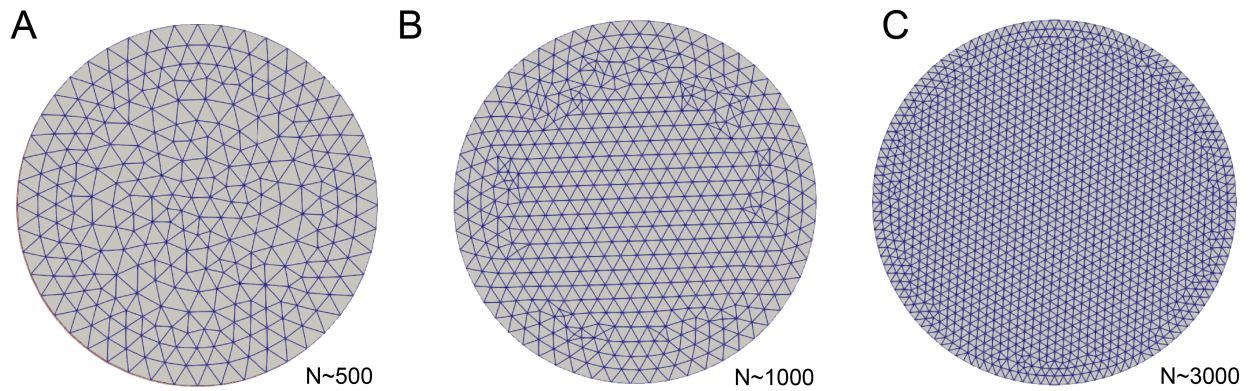
Figure 4.4: A) 500-element mesh. B) 1000-element mesh. C) 3000-element mesh.
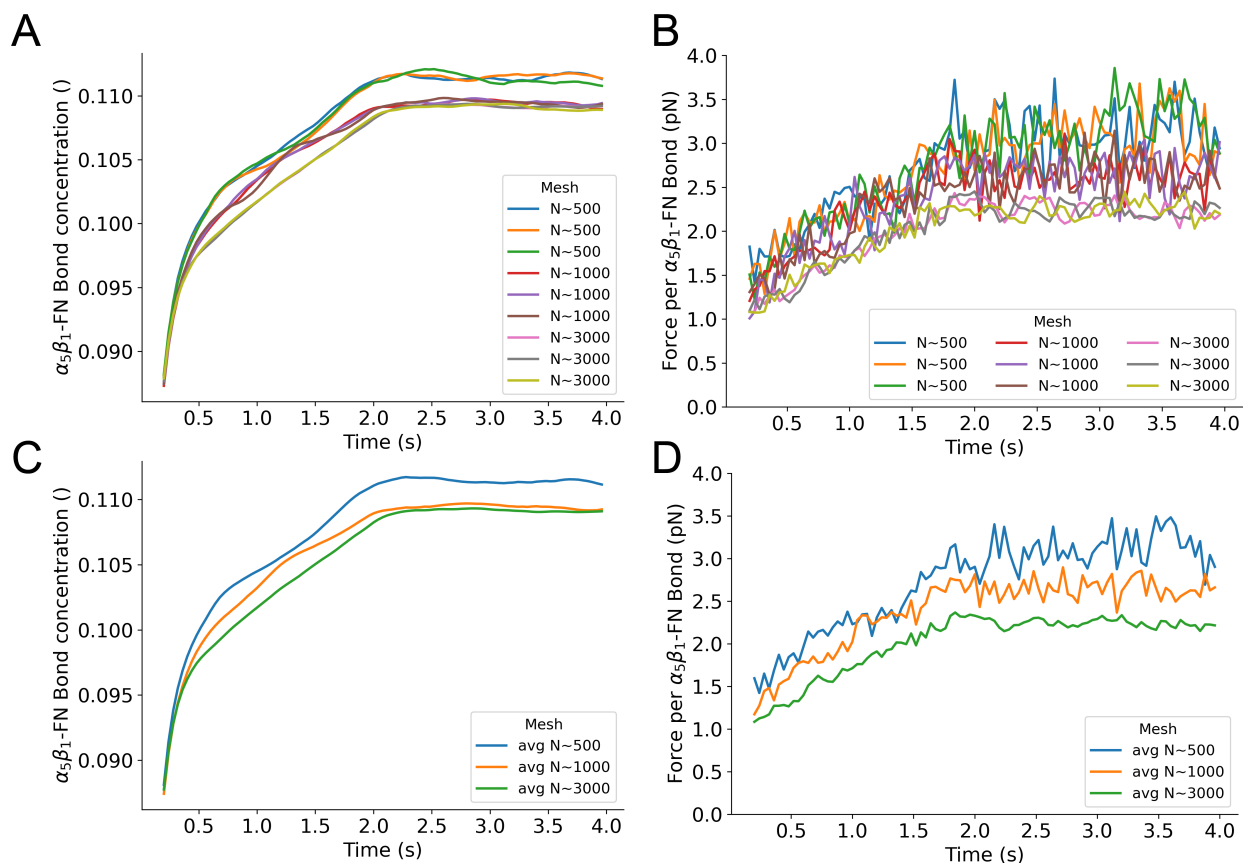
Figure 4.5: Mesh convergence (n=3 runs per mesh) of A) Bond concentration and B) force per bond. Average of C) bond concentration and D) force per bond across three runs. We chose the constant k_{int}=31pN/nm at a timestep of 100μs to run the convergence analysis.

Multiscale Model Coupling

The Gromacs function, `mdrun` outputted the force on the $\alpha_5\beta_1$-FN complex. Furthermore, `gmx trajectory` was used to extract the center-of-mass coordinates of the restraints, LYS559 and GLU36, as well as the pull residue, PRO1142. The $\alpha_5\beta_1$-FN extension length was measured in Python as the average vertical distance between PRO1142 and each of the two restrained residues. The resulting force-extension curve for each simulation run was then plotted. The `optimize` function from the `SciPy` library was used to produce a 5-segment piecewise linear fit on the 1 and 10 nm/ns force-extension curves, respectively. Ultimately, the 1 nm/ns curve-fit was used as a variable displacement-dependent spring constant in the whole-cell model to make up the "MD-driven" $\alpha_5\beta_1$-FN stiffness, k_{int}.
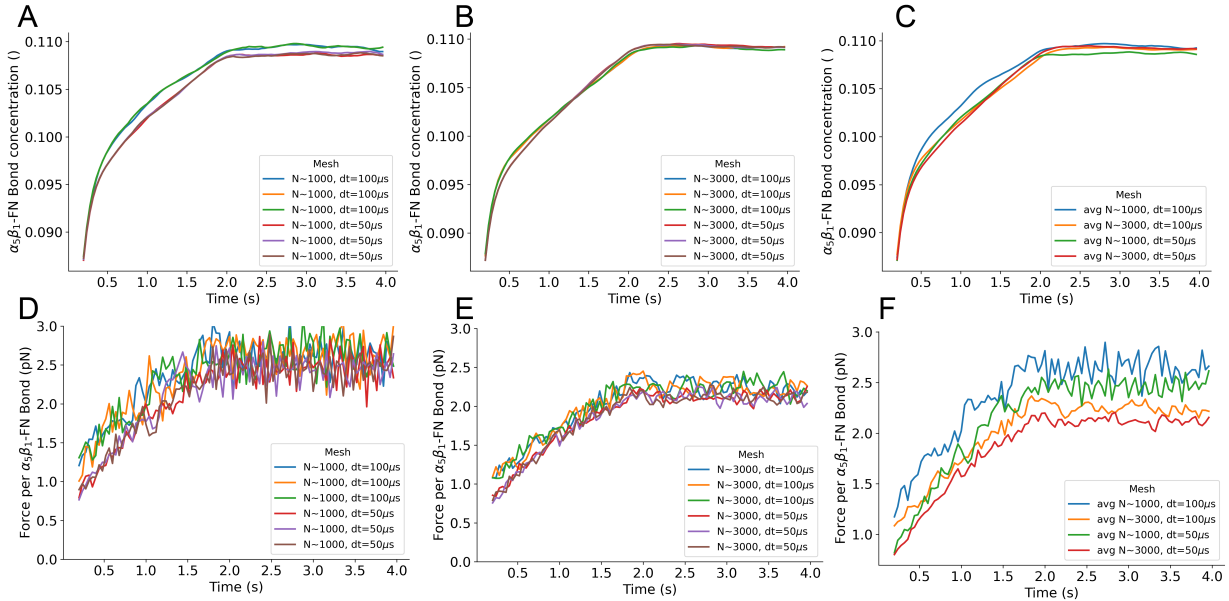
Figure 4.6: Timestep convergence (n=3 runs at $100\mu s$ and $50\mu s$ per 1000-element and 3000-element mesh). Bond concentration from A) three runs of 1000-element mesh at a $100\mu s$ and $50\mu s$ timestep. B) Three runs of 3000-element mesh at a $100\mu s$ and $50\mu s$ timestep. C) Comparison between time-averaged 1000-element and 3000-element mesh runs at a $100\mu s$ and $50\mu s$ timestep. Force per bond from D) three runs of 1000-element mesh at a $100\mu s$ and $50\mu s$ timestep. E) Three runs of 3000-element mesh at a $100\mu s$ and $50\mu s$ timestep. F) Comparison between time-averaged 1000-element and 3000-element mesh runs at a $100\mu s$ and $50\mu s$ timestep. We chose the constant k_{int}=31pN/nm to run the convergence analysis.

4.3   Results and Discussion

$\alpha_5\beta_1$-FN exhibited nonlinear and rate dependent stretching behavior under applied constant velocity

Prior to running the steered MD simulations at two pulling rates, the model's energy minimized to -1.37e7 kJ/mol and the RMSD of the system plateaued during the 1ns NVT simulation (Fig. 4.8). RMSD, pressure, and temperature also remained stable during the 10ns NPT simulation 4.9.

We chose 1 and 10 nm/ns pull rates for the steered MD simulations based on similar rates in other integrin subtypes [23, 73]. As expected, $\alpha_5\beta_1$-FN exhibited rate-dependent stretching behavior, meaning that the $\alpha_5\beta_1$-FN force-displacement curves varied by pull rate (Fig. 4.2 A). The 10 nm/ns simulation reached a higher peak force of 723 pN and greater initial slope of 56 pN/nm compared to 444 pN and 31 pN/nm, respectively for the 1 nm/ns simulation.
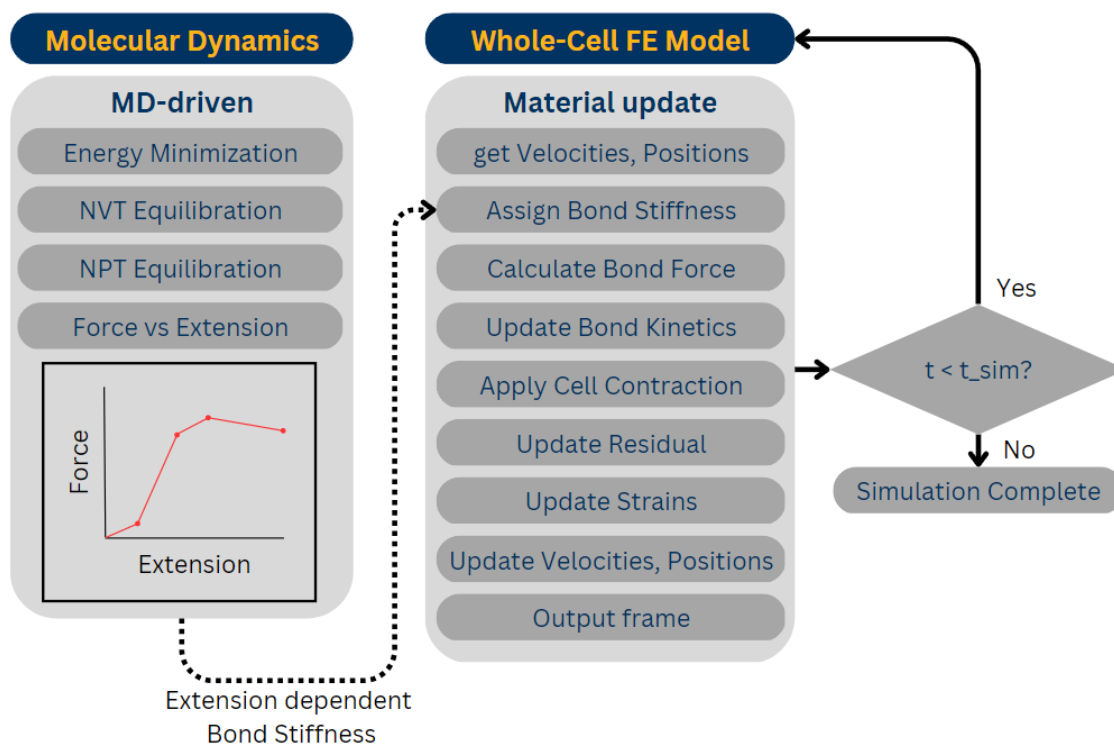
Figure 4.7: Multiscale framework that links the MD model to the FE model via a variable spring constant.

In both cases, the stretching was dominated by FN, while integrin remained mostly rigid with some minor rotation and straightening. Curiously, at the faster 10 nm/ns pull rate, FN9 unraveled first before unbinding from the α_5 head at the synergy site, whereas limited unraveling of FN was observed prior to unbinding for the slower 1 nm/ns pull rate (Fig. 4.2 B). Following the disconnection between FN and α_5 at the synergy site, the force on the whole $\alpha_5\beta_1$ integrin head became biased towards the RGD motif, causing the integrin heads to straighten with elongation of α_5 and β_1. However, the degree of head straightening was not consistent for both pull rates over the course of $\alpha_5\beta_1$-FN extension. We opted to use radius of gyration (R_g) as a proxy for integrin head straightness, with a larger radius indicating a straighter head. Visually, each integrin head started in a more closed positions with a relatively small R_g before opening. Therefore, we believed it was appropriate to assume that a larger R_g corresponded to a straighter molecule. For both rates, we observed an initial increase in the R_g of both integrin heads prior to the unbinding of the salt bridge between arginine (ARG) 1379 in FN9 and aspartic acid (ASP) 154 in α_5 (Fig. 4.10). However, the faster rate showed a sharp increase in R_g of both heads after the salt bridge break at 6.1 nm, indicative of additional bonds pinning FN9 to α_5 that then led to FN9 unfolding and α_5 and β_1 head straightening. In contrast, at the slower rate, we noticed a steady decrease in R_g
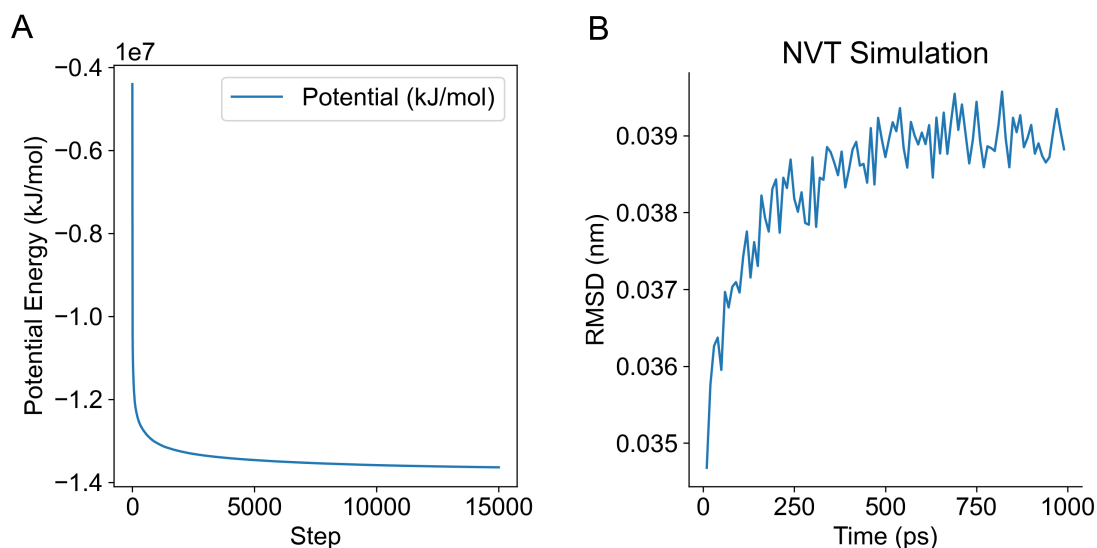
Figure 4.8: A) Energy minimization and B) root-mean-square deviation (RMSD) during 1ns NVT simulation of $\alpha_5\beta_1$-FN
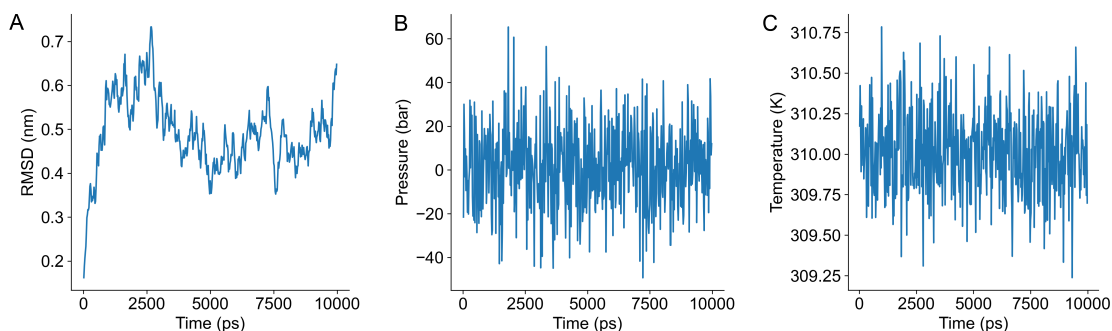
Figure 4.9: A) RMSD, B) Pressure, and C) Temperature of $\alpha_5\beta_1$-FN after 10ns NPT simulation indicative of an equilibrated system

of both heads as FN10 unfolded immediately after the ARG1379-ASP154 break at 5.7 nm, presumably because α_5 was allowed to relax after the departure of FN9. The faster rate elicits a greater reaction force out of $\alpha_5\beta_1$-FN, which were resisted by other bonds between FN9 and α_5 and a straightening of the integrin heads. This result was notable because it provided insight into how integrin may exhibit increased bond lifetime at higher forces, characteristic of previously observed catch bond behavior of integrins [72, 44].

The observed viscoelastic behavior of $\alpha_5\beta_1$ has been shown both experimentally and
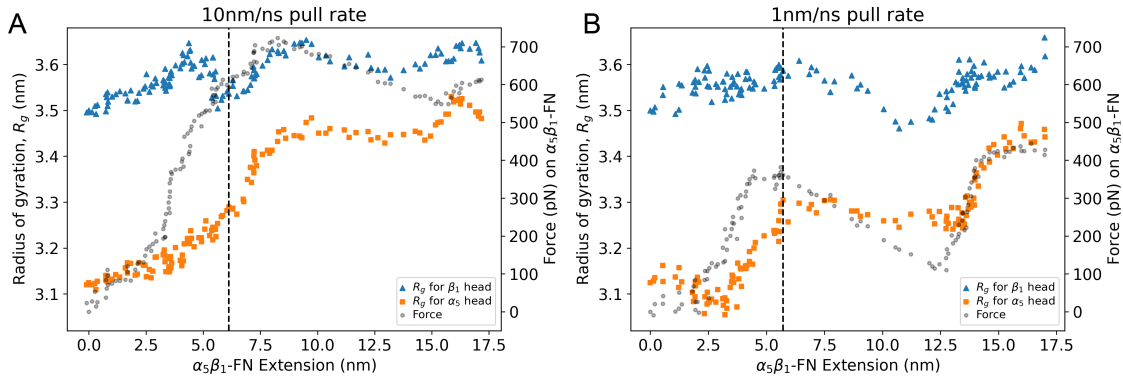
Figure 4.10: Radius of gyration (left vertical axis) of α_5 and β_1 heads and force (right vertical axis) on $\alpha_5\beta_1$-FN during A) 10 nm/ns and B) 1 nm/ns extension. The dashed vertical line on each plot represents the moment the ARG1379-ASP154 salt bridge was broken.

computationally. Single-molecule AFM studies show higher rupture forces at faster pull rates [78] and separate steered MD simulations of integrin [23, 73] and FN [46] showed rate-dependent and force-dependent stretching behavior seen in viscoelastic materials. We expected this viscoelastic behavior to remain when $\alpha_5\beta_1$ and FN are in complex. To confirm, we tested $\alpha_5\beta_1$-FN's viscoelasticity *in silico* via constant force simulations at 300 and 500 pN, similar to what would be done in a mechanical creep test where constant stress is applied (Fig. 4.11). We fit the Bausch viscoelasticity model, which combines a Kelvin model with a dashpot in series [8], to the extension-time plots, supporting the characterization of $\alpha_5\beta_1$-FN's time-dependent stretching and viscoelastic nature.

While our MD simulations and previous literature have demonstrated the nonlinear stretching behavior of $\alpha_5\beta_1$-FN, multiscale models assume a linear integrin stiffness between 0.001-2 pN/nm [25, 52, 14]. Recent multiscale models have used this assumption when analyzing fundamental phenomena such as integrin activation, organization, and clustering at the cell and tissue scales [25, 52, 14]. Most recently, Guo et al. showed a framework that combined adhesion kinetics with the finite element method (FEM) to model stretch-driven mechanosensing at the tissue level by coupling integrin adhesion with the nonlinear tissue mechanics of fibrin and collagen [52]. While these models provide unique insights into multiscale mechanobiology of cell adhesion, for models to account for integrin and FN's nonlinear stretching behavior, a dynamic spring stiffness that adjusts depending on extension is required. For our work, we used our steered MD force-extension plots to inform a dynamically changing spring in a continuum model of the whole cell.

A limitation of our approach is that MD simulations are computationally expensive and runtimes would be unreasonably long if we adopted experimentally relevant 800 nm/s pull rates used by past AFM studies [131, 140]. However, using faster pull rates leads to higher single-molecule forces beyond 300pN as was noticed in our force-extension curves. Moreover,
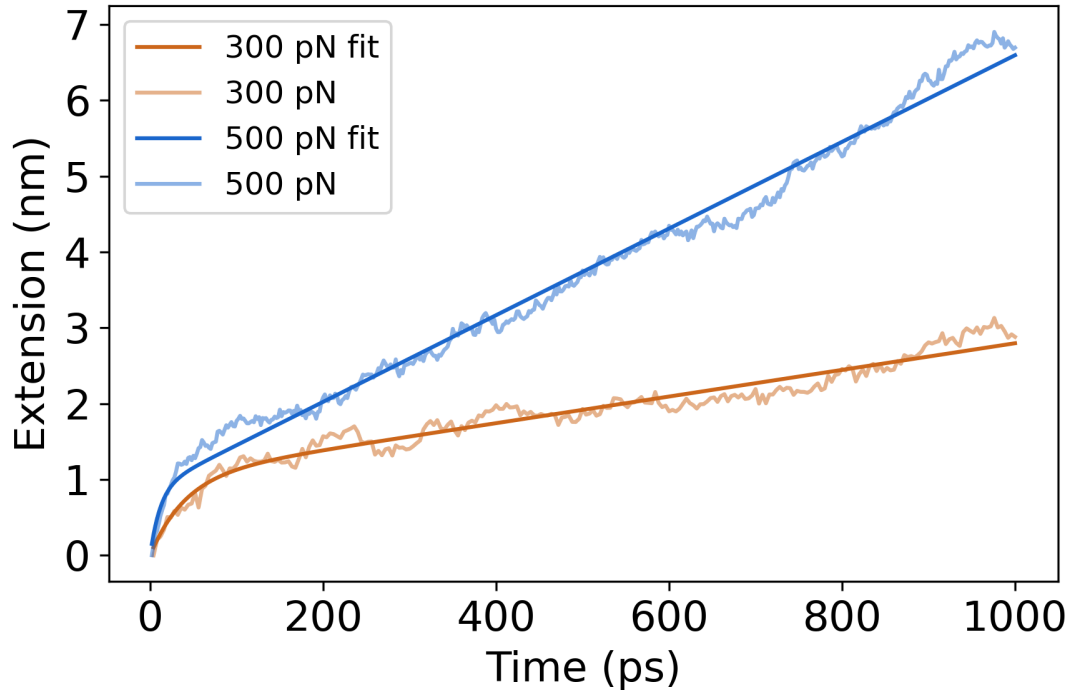
Figure 4.11: Extension plots of constant force simulations at 300pN and 500pN pulling forces. The Bausch [8] viscoelastic model was fit to each of the plots.

the MD model limited the flexibility of the proximal ends of the integrin heads by restraining them with a harmonic spring, potentially contributing to larger measured forces. The heads may have otherwise been more free to move depending on the motion of the integrin legs and tails within the cell membrane, which were not modeled to reduce computational cost and add model stability. Previous studies found average *in situ* rupture forces for $\alpha_5\beta_1$-FN to be 34 [131] and 38.6 pN [140] in endothelial cells and cardiomyocytes, respectively. Single molecule AFM conducted by Li et al. measured a mean rupture force of $\alpha_5\beta_1$-FN of 69 pN at a loading rate of 1800-2000 pN/s, with a peak rupture force of 120 pN at 18,000 pN/s [78]. More recently, FRET-based sensors were used to measure adhesion forces between 1-7 pN on fibroblasts plated on glass [20]. All these measured forces are much lower than those predicted by the MD simulations. Higher forces at much faster pull rates meant that our $\alpha_5\beta_1$-FN stiffness results were significantly larger than what has been observed *in vitro*. However, in all the experiments, the nonlinearity of $\alpha_5\beta_1$-FN's stretching behavior was apparent, challenging the linear stiffness assumption made by previous models [25, 52, 14]. Furthermore, while an average FN stiffness of 0.5 pN/nm has been reported [109, 102], the coupled $\alpha_5\beta_1$-FN stiffness has not. Additionally, our steered MD simulations provided atomic level details that
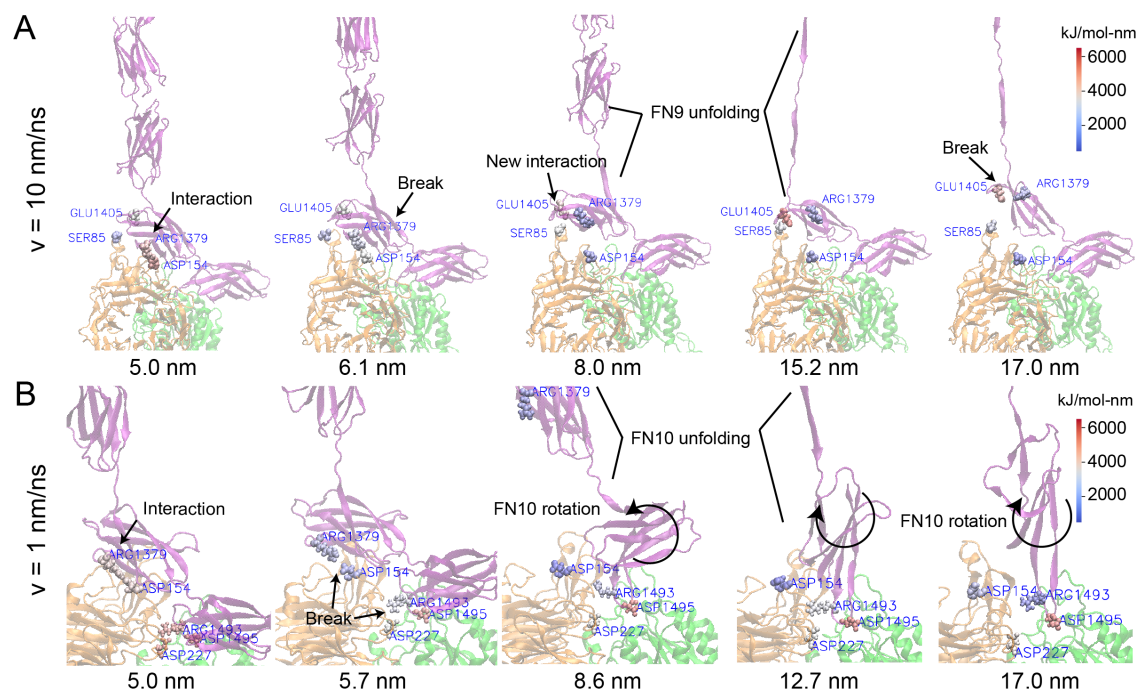
Figure 4.12: Force Distribution Analysis of $\alpha_5\beta_1$-FN for two pull rates at key events. The color map refers to the punctual stress (in kJ/mol-nm) at each residue. (A) At 10 nm/ns, there was a coulombic interaction at the ARG1379-ASP154 salt bridge and no interaction between GLU1405 and SER85. As FN was extended, the salt bridge ruptured and allowed FN to rotate and establish a new interaction between GLU1405 and SER85. FN9 continued to unfold, increasing stress on the GLU1405-SER85 connection, eventually breaking it. (B) At 1 nm/ns, the ARG1379-ASP154 salt bridge, part of the synergy site, together with ARG1493 and ARG1495, part of the RGD motif, maintained a hold on FN. As FN extended, increased stress led to the simultaneous rupture of ARG1493-ASP227 and ARG1379-ASP154. This allowed FN10 to unfold and rotate. ARG1493-ASP227 disconnected and reconnected throughout the remainder of the simulation.

helped explain how key binding sites contributed to pull rate dependent nonlinear stretching.

Force Distribution Analysis of $\alpha_5\beta_1$-FN reveals dynamics of adhesion-mediating residues that contribute to nonlinear force-extension behavior

Visualization of the coulombic interactions via Force Distribution Analysis of the steered MD results demonstrated how key adhesion mediators could contribute to nonlinear, rate-dependent, force-extension of $\alpha_5\beta_1$-FN. Two key mediators are the DRVPHSRN synergy site

and the RGD motif in FN (Fig. 4.3). In our system, the FN synergy site was represented by residues 1373 to 1380 and the RGD motif was represented by residues 1493 to 1495. Spinning disk microscopy has previously shown that mutating one to two select residues on the synergy site leads to a decrease in overall cell adhesion and mutating the RGD motif eliminates cell adhesion force completely [44]. Furthermore, inducing a synergy site mutation or an RGD deletion leads to a reduction in single molecule rupture force of $\alpha_5\beta_1$-FN [78]. Therefore, we looked closely at the dynamics of these adhesion mediators during $\alpha_5\beta_1$-FN stretching at 1 nm/ns and 10 nm/ns.

Interestingly, the $\alpha_5\beta_1$-FN extension showed two modes of stretching depending on the pull rate. Heatmaps overlaid on the molecule illustrated the degree of coulombic interaction, where "hotter" or "redder" zones indicated larger pairwise punctual stresses. For the 10 nm/ns case, the ARG1379-ASP154 salt bridge is broken after 6.1 nm of $\alpha_5\beta_1$-FN extension (Fig. 4.12A). This action then loosens the grip between α_5 and FN9, allowing FN9 to rotate to find a new interaction between glutamic acid (GLU) 1405 and serine (SER) 85. FN9 then unfolded, contributing to the initial decrease in force and most of the extension before GLU1405 and SER85 release. Between 0 and 5 nm, FN began to straighten while simultaneously tugging on the synergy site and RGD. The force-extension response "softened" as the salt bridge was broken and FN9 started to rotate. The large extension and reduction in force past 8 nm (Fig. 4.2) was due to the rapid unfolding of FN9 while GLU1405-SER85 pinned the rest of FN9 in place. After two strands of FN9 are unwound, the applied load became directed at the GLU1405-SER85 pin until it finally separated. Notably, the unfolding pathway with two strands unwound of FN9 has been illustrated before in constant force simulations of FN [46]. Our model corroborates these results while providing new insight into the dynamics of FN unfolding when interacting with $\alpha_5\beta_1$ integrin.

The observed unbinding and unfolding sequence in $\alpha_5\beta_1$-FN was not preserved at 1 nm/ns. The salt bridges, ARG1379-ASP154 and ARG1493-ASP227 simultaneously broke at 5.7 nm of extension after a short force plateau between 4.8-5.7nm, but unlike in the 10nm/ns run, FN9 did not create a new interaction with α_5 (Fig. 4.12B). Rather, FN10 unfolded, leading to the majority of the overall extension and reduction in force from 5.7-12.7nm (Fig. 4.2A). During FN10 unfolding, the interaction between ARG1493 in FN and ASP227 in α_5 alternated between high and low coulombic interactions while ARG1495 maintained adhesion with β_1 integrin. Due to the lack of interaction between the synergy site in FN9 and α_5, FN9 was free to separate from integrin so FN10 could readily unfold. Once one strand had completely unfolded, due to the direction of the pulling force with respect to the orientation of FN10, the force needed to rotate FN10 prior to unwinding the second strand, which led to an increase in force (Fig. 4.2B).

At both pull rates, the synergy site and RGD loop played key roles in maintaining the adhesion between $\alpha_5\beta_1$ and FN. Specifically, the salt bridge between ARG1379 and ASP154 contributed to the molecule's initial "stiff" behavior prior to FN unfolding; and part of the RGD loop between β_1 and FN10 was the only remaining connection between integrin and FN after full extension. Due to their instrumental role, it stands to reason that interfering with these residues via point mutations would reduce adhesion [44] and rupture force [78]. While

measured *in vitro* forces on $\alpha_5\beta_1$-FN have been shown to be much smaller than we have presented due to our model's much faster pulling speed, nonlinear force-extension behavior and rapid jumps in force have been observed [78, 44, 20]. We showed how key residues could contribute to this characteristic behavior during $\alpha_5\beta_1$-FN extension in a pull rate dependent manner. To bridge the nanoscale integrin stretching to cell-scale integrin dynamics, as a proof-of-concept, we modeled the force-extension of $\alpha_5\beta_1$ as a nonlinear spring and used it to scale up to a 2D whole-cell continuum model.

Multiscale integration of $\alpha_5\beta_1$-FN force-extension with whole-cell integrin dynamics

Prior to integrating the force-extension curves from the MD runs, we had ran a baseline simulation of the whole-cell model with similar parameters to those commonly used in literature [52, 25, 14]. In particular, we set the $\alpha_5\beta_1$-FN stiffness, k_{int}, to 1pN/nm. For all simulations, the cell contractility was ramped from 0 to 200Pa within the first 2s and held at 200Pa for the remainder of the 12s simulation. Integrins were recruited to the cell border, achieving maximum concentration and force as the contractility reached 200Pa at 2s (Fig. 4.13).

Integrin's spatial distribution on the cell's leading edge during motion has been previously observed *in vitro* [10], corroborating the results from the model. During contraction, the model's average peak bond concentration reached 10.6% (Fig. 4.14A) with a max peak of 22.5%. The average force per bond followed a similar curve, reaching an average peak of 1.9pN (Fig. 4.14B) with a max peak of 28.6pN at the cell boundary. These bonds had short lifetimes and dissociated quickly, allowing the model to dissipate the contraction and reach equilibrium just before the 6s mark. After reaching this equilibrium point, the mean force was 0.17±0.04pN with max forces reaching 15.9pN at the boundary. The peak bond forces and concentrations occurred on the boundary due to the positive feedback loop of the catch-slip bond dynamics. While the strain across the cell is uniform due to the applied isotropic contractility, the deformation of the bond springs are the greatest at the boundary, leading to higher bond concentrations and forces. Overall, the forces were within the 1-38pN range that has been observed *in vitro* [131, 140, 20] and well within the peak single $\alpha_5\beta_1$-FN rupture forces measured via AFM of 120pN [78].

The baseline simulation provided a control to test against our two simulation conditions derived from the 1 nm/ns MD simulation. We defined a varying, MD-driven $\alpha_5\beta_1$-FN stiffness as the entire 1nm/ns force-extension curve fit. To evaluate how the nonlinearity of the MD-driven integrin spring affected whole-cell adhesion dynamics, we used the slope of the first segment, 31pN/nm, to define a constant $\alpha_5\beta_1$-FN stiffness test condition.

Overall, the $\alpha_5\beta_1$-FN bond concentration for the constant and MD-driven $\alpha_5\beta_1$-FN stiffness conditions followed a similar trend and were both slower to distribute the contraction load (Fig. 4.14) than the 1pN stiffness setting. Past 2s, the mean forces steadied at 2.45±0.18pN and 2.59±0.19pN for the constant and MD-driven runs, respectively. The noise in the the
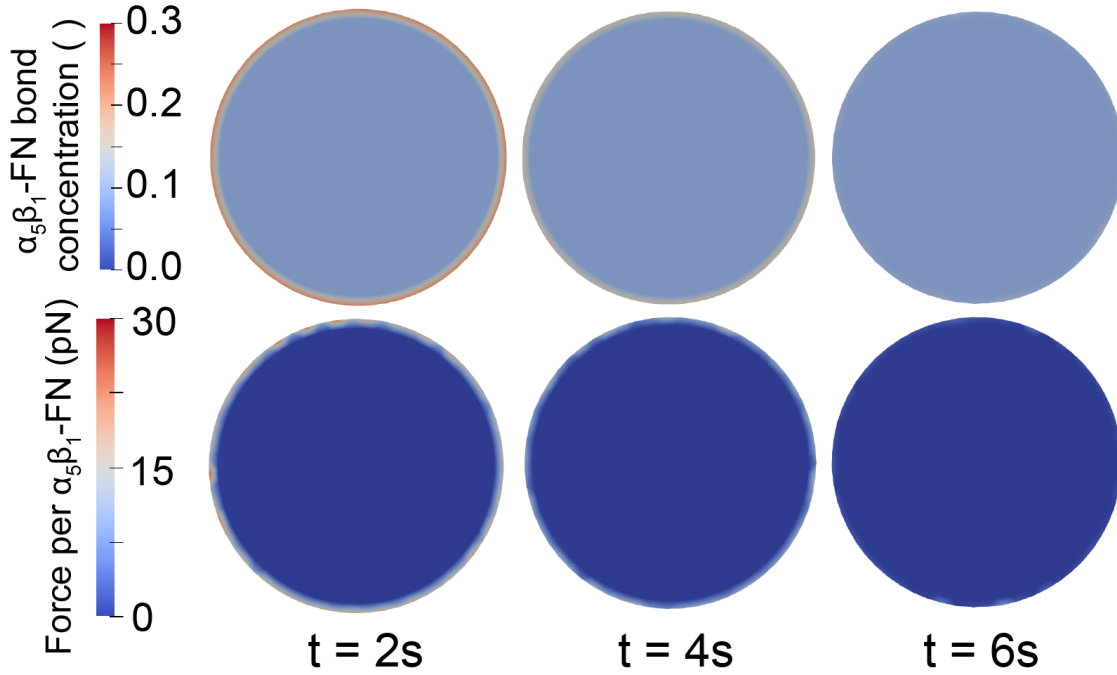
Figure 4.13: The dimensionless $\alpha_5\beta_1$-FN bond concentration (top) and force per $\alpha_5\beta_1$-FN (bottom) results for the baseline whole-cell simulation with $k_{int} = 1$pN/nm. $\alpha_5\beta_1$-FN localization and force dissipation occurred rapidly and no significant changes in distribution were observed past 6s.

bond concentrations and force per bond (Fig. 4.14) were due to the random 5pN actin polymerization force. The results for both cases were similar. The constant 31pN/nm run reached a max average bond concentration of 10.9% and the MD-driven case topped at 11.0%. Max average forces, located at the cell boundary (Fig. 4.15), were 53.5pN and 55.6pN for the 31pN/nm and MD-driven runs, respectively. The positive feedback loop of the catch-slip bond at the boundary continued to drive the peak forces and concentrations across all stiffness settings.

Notably, model predictions surpass *in situ* rupture forces of 34-38.6pN for $\alpha_5\beta_1$-FN [131, 140] and 40pN for another subtype, $\alpha_V\beta_3$ [137]. Chang et al. used FRET-based sensors to measure adhesion forces between 1-7 pN on fibroblasts [20]. Recent work has used leveraged tension gauge tethers to measure single molecule forces on RGD-binding integrins and showed that integrin activation occurs below 12 pN and $\alpha_V\beta_1$ could sustain forces over 54pN in mature FAs [68]. In summary, the models we presented showed estimations towards the upper bounds of measured biophysical forces felt by integrin.

The MD-driven and constant 31pN/nm integrin stiffness models showed similar force and concentration results indicating that linear spring stiffness was sufficient to capture $\alpha_5\beta_1$-FN
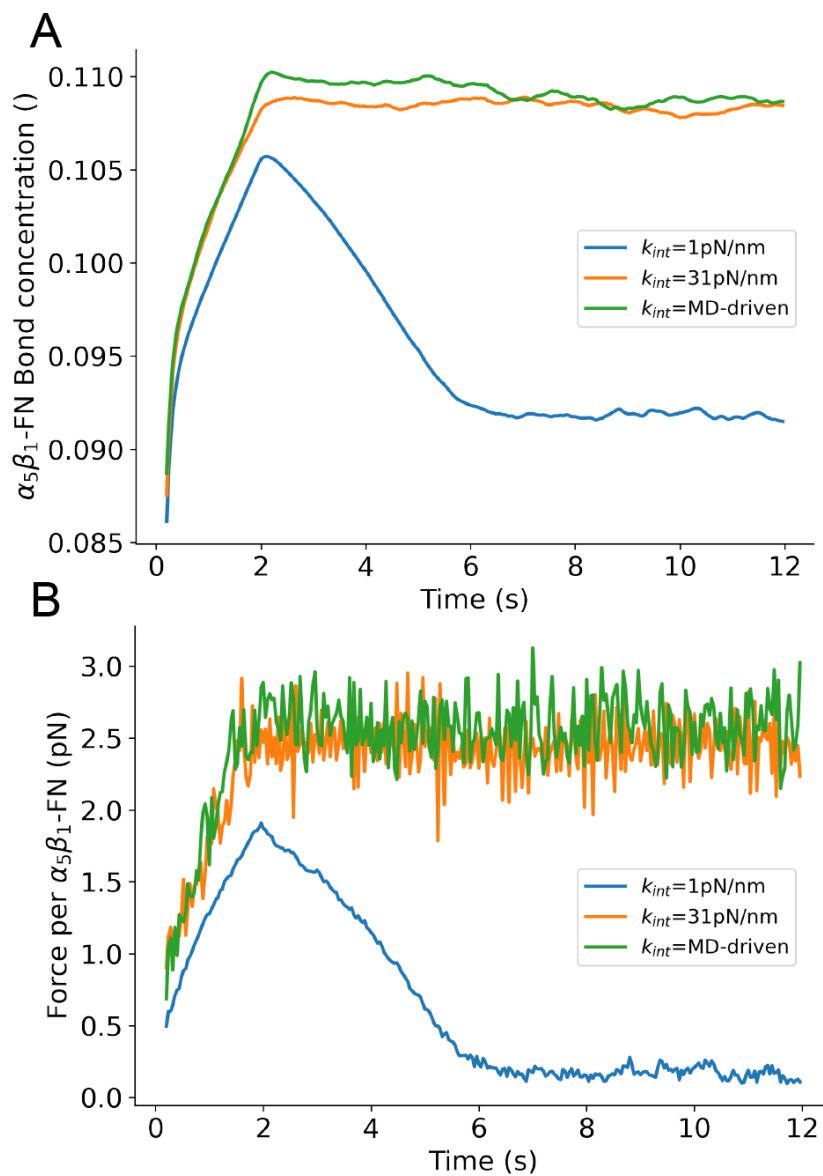
Figure 4.14: Whole-cell average A) $\alpha_5\beta_1$-FN bond concentration (dimensionless) and B) force per $\alpha_5\beta_1$-FN over the simulation run. Three test conditions for $\alpha_5\beta_1$-FN stiffness are shown per plot: 1) constant 1pN/nm baseline from past models [52, 25, 14], 2) constant 31pN/nm based on the first segment of the 1nm/ns force-extension curve fit, and 3) MD-driven stiffness derived from using all segments of the curve fit.

molecular dynamics in this model. Notably, bond lengths were maintained below 2.5nm, where the stiffness jumps to 99.5pN/nm in the MD-driven force-extension curve (Fig. 4.2A).
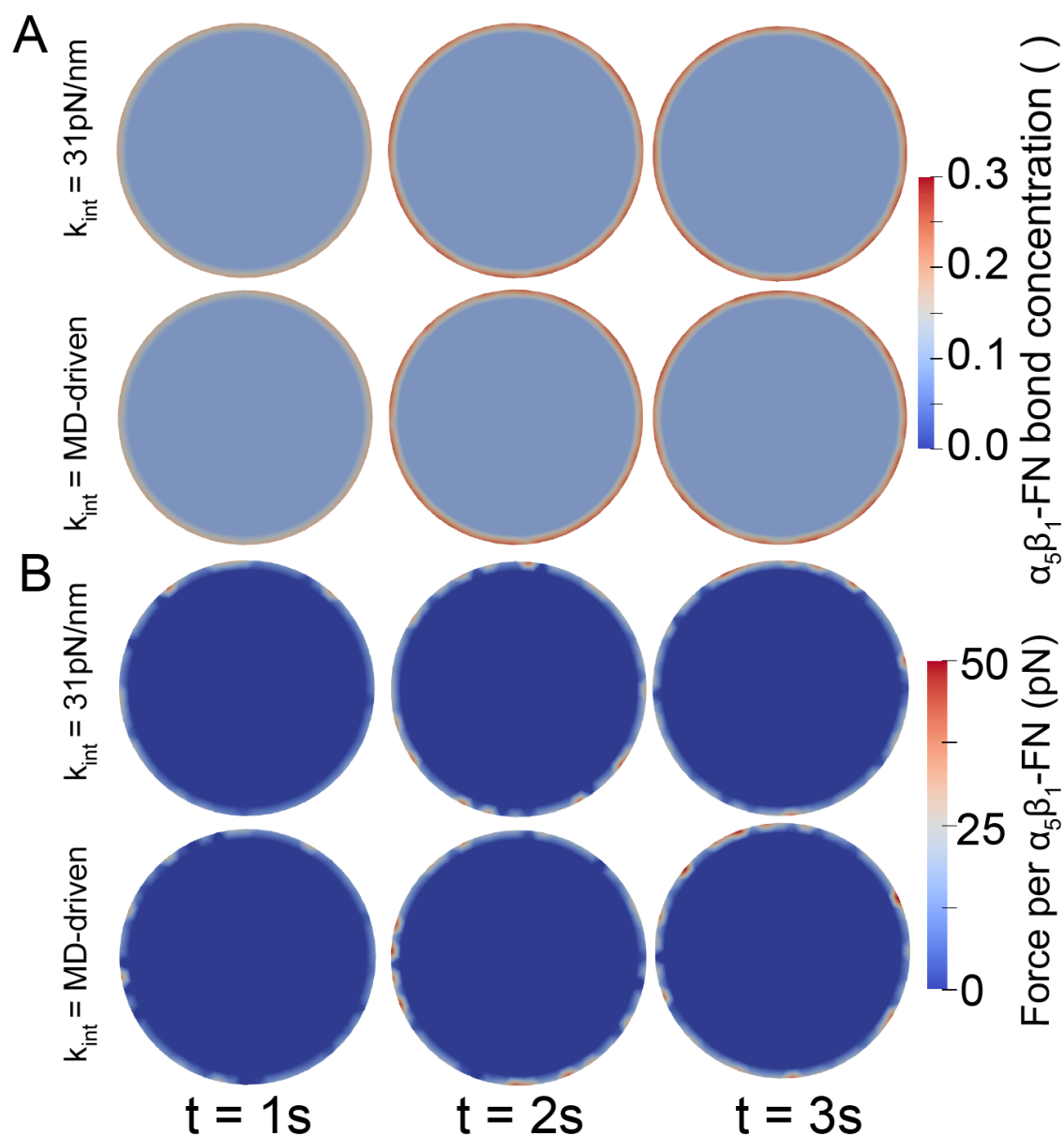
Figure 4.15: Whole-cell simulation results for the constant and MD-driven spring stiffnesses. A) $\alpha_5\beta_1$-FN bond concentration and B) Force per $\alpha_5\beta_1$ integrin at three time frames within the first 3s of the simulation. Dissipation continued past 3s, but the changes were minor.

The main difference observed in the bond force and concentration response was between soft (1pN/nm) and stiff (31pN/nm, MD-driven) integrin models. These differences arose due to the force balance between the cell, the substrate, the integrin, and other random forces
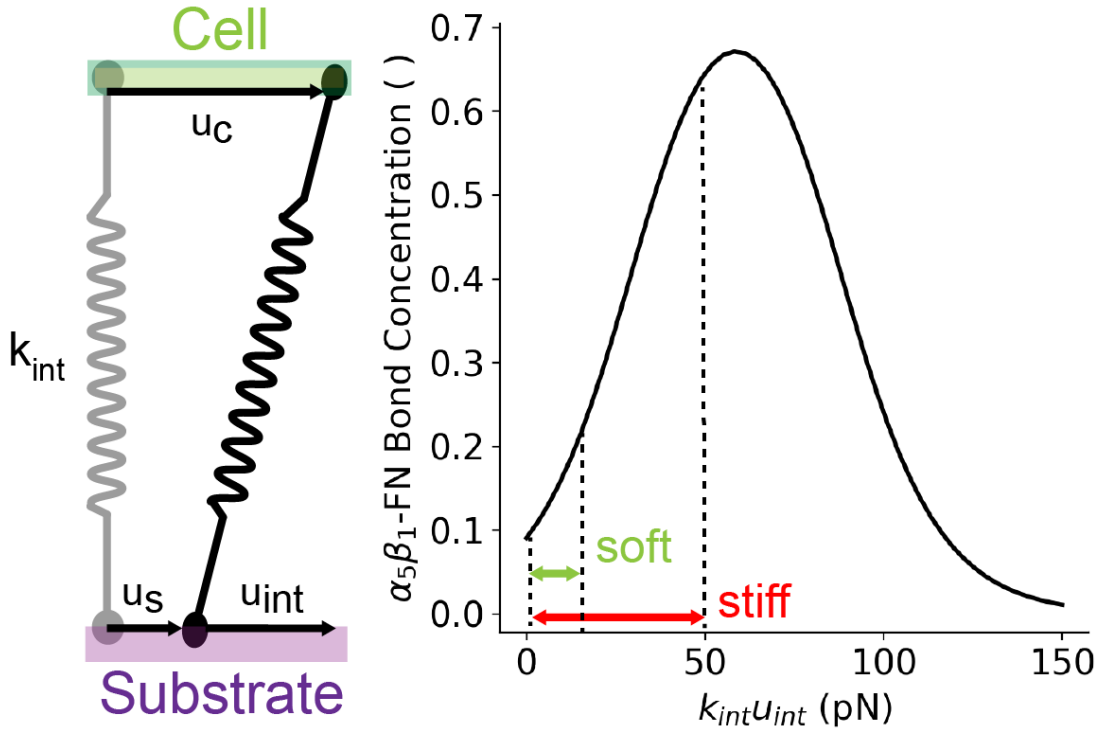
Figure 4.16: Schematic of the balance at an equilibrium state between the cell, substrate, and spring deformations contribute to changing bond concentrations based on the catch-slip bond curve (eq. 4.8).

(eq. 4.13). All these forces contributed to the integrin deformation, u_{int} (Fig. 4.16), which was multiplied by integrin stiffness to calculate force. This bond concentration was updated based on this bond force and catch-slip bond model (Fig. 4.16 and eq. 4.8). In our case, the bond lengths ranged from 0-15.9nm for the soft integrin and 0-1.8nm in the stiff integrin. This led to forces between 0-15.9pN and 0-55.6pN for the soft and stiff integrin, respectively. To summarize, the balance between applied forces, cell/substrate material properties, and integrin stiffness led to varying bond deformation which contributed to alterations in bond concentration due to catch-slip bond dynamics.

4.4   Conclusion

We developed a coupled multiscale model which showed how amino acid interactions at the synergy site in FN contribute to the nonlinear force-extension behavior of $\alpha_5\beta_1$-FN, which leads to unique whole-cell adhesion force landscapes. The model demonstrated whole-cell integrin spatial distribution along the cell membrane, consistent with fibroblasts plated *in*

vitro [10] and forces within the 120pN maximum single molecule rupture force and 1-38 pN *in situ* rupture forces [131, 140, 20].

This study has limitations. We used high pull rates in the MD simulations to maintain reasonable computational runtimes. However, this led to large forces during $\alpha_5\beta_1$-FN extension. While the computational cost is a common drawback of MD, the detailed data and outputs gained from the amino acid dynamics and their connection to whole-cell integrin dynamics would have been otherwise unobservable. Therefore, we believe that it was useful to include this demanding piece of the multiscale model. A combination of slower pull rates and coarse grained MD simulations could be the compromise necessary to investigate the nonlinear mechanics while maintaining some nanoscale details.

Also, we chose $\alpha_5\beta_1$ integrin as the sole surface receptor, but cells have additional subtypes with varying roles [14, 141] and potentially different adhesion strengths [68] and binding kinetics [70, 79]. Given the 24 known subtypes of integrin [125], it is critical to understand which ones are the main contributors to adhesion maintenance in the presence of specific ligands. For example, in the case of fibronectin, a recent single-cell force spectroscopy study indicated that pan integrin knockout fibroblasts only expressing $\alpha_5\beta_1$ and $\alpha_V\beta_3$ transmitted the same amount adhesive force as wildtype fibroblasts on a fibronectin coated surface [122]. Therefore, extending our model to contain these two subtypes may be an appropriate approximation to evaluate integrin adhesion mechanics for fibroblasts on fibronectin. Another key consideration is the dynamics of low-affinity and high-affinity conformations of integrin. For our model, we assumed that $\alpha_5\beta_1$ integrin was in a high affinity, extended-open conformation. However, it has been demonstrated that low-affinity bent-closed and extended-closed conformations of $\alpha_5\beta_1$ and $\alpha_V\beta_3$ can still bind to fibronectin [79, 24]. To include the contributions of varying subtypes, it would be necessary to update to our catch-slip bond model (Fig. 4.16) to include high and low affinity conformational states, manage the population distribution of integrin subtypes as done in other models [14, 25], and expand on existing steered MD characterizations of $\alpha_V\beta_3$ [23, 80] to add to ours of $\alpha_5\beta_1$. Overall, more investigation is needed to evaluate how integrin subtypes collaborate to manage cell adhesion dynamics.

The model assumed a homogeneous substrate. However, tissue microenvironments are spatially heterogeneous and respond to the binding and unbinding dynamics between ECM fibers [86, 21, 94, 82, 37]. This leads to viscoplastic material behavior, or time and frequency dependent force dissipation [111] which mediates cell migration, differentiation, and disease progression [85, 81, 98]. To include these effects, we could represent the substrate viscoplasticity via the Norton-Hoff constitutive model [86, 54], and the cell's myosin-actin engagement via the molecular or motor clutch model [51, 37]. We would expect a heterogeneity to arise in the force and spatial distribution of the integrin bonds, localizing near denser packs of crosslinked fibers. We hypothesize that stiffer integrins would lead to denser packing of ECM fibers due to their slow rate of sustained force compared to softer bonds. However, more investigation is needed to reveal the relationship between cell adhesion and force-mediated ECM fiber mechanics.

Our model focused on cell adhesion mechanics and has the potential to grow into a framework that can investigate cell mechanotransduction across multiple scales. For example,

we could test how unique mutations on integrins affect whole-cell dynamics *in silico*. Additionally, by incorporating the cell nucleus, we could support early evidence to show how its mechanosensitive nature and material properties could govern gene transcription [135, 136, 133]. Key components that have previously been modeled such as the cell membrane, integrin's transmembrane domain, and integrin clustering and diffusion [105, 89, 90, 25, 14] were omitted from our model for simplicity, but could be added as new multiscale mechanobiological questions are posed regarding their mechanics. Lastly, our multiscale framework could be broadened to reveal the nano- and micro- mechanics within nascent engineered tissues and organ-chips that apply controllable biophysical loads at the cell membrane [38, 83, 88, 7, 34, 121].

Chapter 5

Conclusion

5.1 Synopsis

This dissertation created computer simulations to explore the hidden mechanisms that give rise to physiological and pathological effects. In particular, we conducted three studies using steered MD simulations and the FE method to propose how $\alpha_5\beta_1$ integrin mechanosensing is involved in cell adhesion at the atomic level. In these studies, we contributed to the field of cell mechanobiology by showcasing structural changes in $\alpha_5\beta_1$-FN due to force. In **Chapter 2: Molecular Mechanism of $\alpha_5\beta_1$ Mechanosensing** we applied controlled velocities to $\alpha_5\beta_1$-FN complex, which could stem from cell migration, and found a pivot-clip mechanism that works to engage the $\alpha_5\beta_1$ integrin heads through two binding domains in fibronectin known as the RGD and synergy site. We also found that the force transmission was only minimally affected by synergy site mutagenesis. This was a puzzling outcome since in vitro cell adhesion assays show a disruption in adhesion strength. However, the cell in minimally-tensioned state is known to still transmit forces across integrin, even without synergy site engagement [20]. To solve this mystery, we developed the whole-cell adhesion model shown in **Chapter 3: Dynamic $\alpha_5\beta_1$-FN Adhesion Collaboration**. The model results showed that, at modest cell contraction forces seen in vitro, mutated $\alpha_5\beta_1$-FN bonds were able to rebalance their forces to match those seen in wildtype bonds. Taken together, chapters 2 and 3 point to a specific property of the synergy site binding site in $\alpha_5\beta_1$ integrin may be to mediate the degree of mechanosensing and mechanosignaling in to the presence of varying forces. At low to medium forces, synergy site engagement allows for long lasting bonds that would otherwise be ruptured at high forces. Lastly, in **Chapter 4: Bridging Simulations of $\alpha_5\beta_1$-FN Across Scales**, we ventured to inform the whole-cell model via the force-extension behavior of $\alpha_5\beta_1$-FN from the steered MD simulations. While this coupling is indeed challenging due to the technical limitations of running accelerated MD simulations, the multiscale framework has been established to allow for future modification of mechanical and kinetic parameters necessary when studying mechanosensitive mechanisms of cell adhesion. As an example, drug candidates that modify cell-matrix adhesion binding

affinity or integrin mechanical stiffness can be tested in silico prior to in vitro experiments.

5.2 Outlook

Looking ahead, the models developed here can be advanced to answer a variety of questions about cell adhesion at molecular and cellular scales. As mentioned in the Introduction, while many integrin therapeutics have been synthesized and have been proven safe, none have shown to be efficacious in clinical trials. One component that is often overlooked during drug design and development is the forces that the cell resists, which may lead to conformational changes that impact the ability of drug candidates to bind. To screen new and past drug candidates, we could dock small molecules along new sites in $\alpha_5\beta_1$ during long-term, equilibrium MD simulations with a small applied constant force on RGD and the synergy site. Limiting the simulation box size to only the integrin heads and implementing new techniques in coarse-graining and coarse-grain-to-atomistic backmapping may be necessary to achieve physiologically relevant timescales in the micro- to milliseconds. Coarse-grained simulations group together atomic interactions into beads, reducing the model's degrees of freedom, allowing for smaller particle counts, larger step sizes, and longer simulation timescales at the cost of atomic resolution. Alternatively, specialized software and hardware systems have reached microsecond and even millisecond timescales while maintaining all-atom resolution [118] and may be favorable route to elucidating novel mechanosensing mechanisms. In parallel, in vitro methods such as AFM, optical tweezers, or FRET must be considered to test new drug candidates produced from simulations and whether the performance of the new drugs is improved compared to previously tested ones. Binding assays can inform the whole-cell model to predict whether the per-integrin bond forces are sustainable.

Beyond the present work, there remains much to be explored about the mechanosensing properties of integrin in the context of cell mechanobiology and disease. The mechanical and chemical crosstalk between integrin, cytoplasmic proteins, and the nucleus remains an open field of investigation. Recent work highlighting the role of kindlin in promoting integrin activation [65], how the nucleus also plays a role in informing cell adhesion strength through chromatin compaction [17], and how mechanosensitive cytoplasmic proteins aid in nuclear mechanosensing [55] have moved the field to exploring the connection between the cell and the nucleus. The field has also been driving towards physiologically relevant mechanisms by exploring the role of curvature, which is inherent in the body, in cell mechanosensing. A new adhesion modality has been discovered in the form of a curved adhesion, which are composed of curvature sensing proteins and $\alpha_V\beta_5$ integrins that link to the ECM [144], providing another unexplored therapeutic target. Cells sense curvature not only individually, but also collectively. New findings showed that cell monolayers on larger curvatures migrated with less collective coordination and showed a dynamic flow pattern, but the mechanical mechanisms that promote this behavior are unknown [129]. Additionally, the collaboration between single-cell and multicellular curvature sensing remains an open question with implications in physiological development and drug discovery. Overall, the field of cell mechanobiology

is extending towards exciting frontiers that aim to tackle fundamental biological questions while unveiling paths towards promising biotechnology innovations.

Bibliography

[1]   Mark James Abraham et al. "GROMACS: High performance molecular simulations through multi-level parallelism from laptops to supercomputers". In: *SoftwareX* 1 (2015), pp. 19–25.

[2]   Farida B Ahmad and Robert N Anderson. "The leading causes of death in the US for 2020". In: *Jama* 325.18 (2021), pp. 1829–1830.

[3]   Michael P Allen and Dominic J Tildesley. *Computer simulation of liquids*. Oxford university press, 2017.

[4]   Shin-ichi Aota, Motoyoshi Nomizu, and Kenneth M Yamada. "The short amino acid sequence Pro-His-Ser-Arg-Asn in human fibronectin enhances cell-adhesive function." In: *Journal of Biological Chemistry* 269.40 (1994), pp. 24756–24761.

[5]   Michael Bachmann et al. "Cell adhesion by integrins". In: *Physiological reviews* 99.4 (2019), pp. 1655–1699.

[6]   Dalit Barkan et al. "Metastatic Growth from Dormant Cells Induced by a Col-I–Enriched Fibrotic Environment Metastatic Outgrowth from Dormant Tumor Cells". In: *Cancer research* 70.14 (2010), pp. 5706–5716.

[7]   Jeanne E Barthold et al. "Recellularization and integration of dense extracellular matrix by percolation of tissue microparticles". In: *Advanced functional materials* 31.35 (2021), p. 2103355.

[8]   Andreas R Bausch et al. "Local measurements of viscoelastic parameters of adherent cell surfaces by magnetic bead microrheometry". In: *Biophysical journal* 75.4 (1998), pp. 2038–2049.

[9]   George I Bell. "Models for the specific adhesion of cells to cells: a theoretical framework for adhesion mediated by reversible bonds between cell surface molecules." In: *Science* 200.4342 (1978), pp. 618–627.

[10]   Maria Benito-Jardón et al. "The fibronectin synergy site re-enforces cell adhesion and mediates a crosstalk between integrin classes". In: *Elife* 6 (2017), e22264.

[11]   Allison L Berrier and Kenneth M Yamada. "Cell–matrix adhesion". In: *Journal of cellular physiology* 213.3 (2007), pp. 565–573.

[12]   Tamara C Bidone and David J Odde. "Multiscale models of integrins and cellular adhesions". In: *Current Opinion in Structural Biology* 80 (2023), p. 102576.

[13]   Tamara C Bidone et al. "Coarse-grained simulation of full-length integrin activation". In: *Biophysical journal* 116.6 (2019), pp. 1000–1010.

[14]   Tamara C Bidone et al. "Multiscale model of integrin adhesion assembly". In: *PLOS Computational Biology* 15.6 (2019), e1007077.

[15]   E Braun et al. *Best Practices for Foundations in Molecular Simulations*. 2018.

[16]   Tyson Brochu and Robert Bridson. "Robust topological operations for dynamic explicit surfaces". In: *SIAM Journal on Scientific Computing* 31.4 (2009), pp. 2472–2493.

[17]   Julie Buisson et al. "Reverse Mechanotransduction: Driving Chromatin Compaction to Decompaction Increases Cell Adhesion Strength and Contractility". In: *Nano Letters* (2024).

[18]   Alexia Caillier et al. "T cells Use Focal Adhesions to Pull Themselves Through Confined Environments". In: *bioRxiv* (2023). DOI: 10.1101/2023.10.16.562587. eprint: https://www.biorxiv.org/content/early/2023/10/19/2023.10.16.562587.full.pdf. URL: https://www.biorxiv.org/content/early/2023/10/19/2023.10.16.562587.

[19]   Lizhi Cao et al. "Detection of an integrin-binding mechanoswitch within fibronectin during tissue formation and fibrosis". In: *ACS nano* 11.7 (2017), pp. 7110–7117.

[20]   Alice C Chang et al. "Single molecule force measurements in living cells reveal a minimally tensioned integrin state". In: *ACS nano* 10.12 (2016), pp. 10745–10752.

[21]   Ovijit Chaudhuri et al. "Effects of extracellular matrix viscoelasticity on cellular behaviour". In: *Nature* 584.7822 (2020), pp. 535–546.

[22]   Cheng Chen et al. "Substrate stiffness together with soluble factors affects chondrocyte mechanoresponses". In: *ACS applied materials & interfaces* 6.18 (2014), pp. 16106–16116.

[23]   Wei Chen et al. "Molecular dynamics simulations of forced unbending of integrin $\alpha V\beta 3$". In: *PLoS computational biology* 7.2 (2011), e1001086.

[24]   Yunfeng Chen et al. "Force regulated conformational change of integrin $\alpha V\beta 3$". In: *Matrix biology* 60 (2017), pp. 70–85.

[25]   Bo Cheng et al. "Nanoscale integrin cluster dynamics controls cellular mechanosensing via FAKY397 phosphorylation". In: *Science advances* 6.10 (2020), eaax1909.

[26]   Bogdan I Costescu and Frauke Gräter. "Time-resolved force distribution analysis". In: *BMC biophysics* 6.1 (2013), pp. 1–5.

[27]   Dermot Cox, Marian Brennan, and Niamh Moran. "Integrins as therapeutic targets: lessons and opportunities". In: *Nature reviews Drug discovery* 9.10 (2010), pp. 804–820.

[28] Sarah M Cutler and Andrés J García. "Engineering cell adhesive surfaces that direct integrin $\alpha5\beta1$ binding using a recombinant fragment of fibronectin". In: *Biomaterials* 24.10 (2003), pp. 1759–1770.

[29] Jason S Damiano et al. "Cell adhesion mediated drug resistance (CAM-DR): role of integrins and resistance to apoptosis in human myeloma cell lines". In: *Blood, the Journal of the American Society of Hematology* 93.5 (1999), pp. 1658–1667.

[30] Kerim C Dansuk and Sinan Keten. "Self-strengthening biphasic nanoparticle assemblies with intrinsic catch bonds". In: *Nature communications* 12.1 (2021), p. 85.

[31] Kerim C Dansuk, Subhadeep Pal, and Sinan Keten. "A catch bond mechanism with looped adhesive tethers for self-strengthening materials". In: *Communications Materials* 4.1 (2023), p. 60.

[32] Siva Dasetty, Tamara C Bidone, and Andrew L Ferguson. "Data-driven prediction of αIIb$\beta3$ integrin activation paths using manifold learning and deep generative modeling". In: *Biophysical Journal* (2023).

[33] Jie Deng et al. "Nanopatterned adhesive, stretchable hydrogel to control ligand spacing and regulate cell spreading and migration". In: *ACS nano* 11.8 (2017), pp. 8282–8291.

[34] Prachi Dhavalikar et al. "Review of Integrin-Targeting Biomaterials in Tissue Engineering". In: *Advanced healthcare materials* 9.23 (2020), p. 2000795.

[35] Serge Dmitrieff and François Nédélec. "Amplification of actin polymerization forces." In: (2016).

[36] Tristan P Driscoll et al. "Integrin-based mechanosensing through conformational deformation". In: *Biophysical journal* 120.20 (2021), pp. 4349–4359.

[37] Alberto Elosegui-Artola. "The extracellular matrix viscoelasticity as a regulator of cell and tissue dynamics". In: *Current Opinion in Cell Biology* 72 (2021), pp. 10–18.

[38] Alberto Elosegui-Artola et al. "Matrix viscoelasticity controls spatiotemporal tissue organization". In: *Nature Materials* (2022), pp. 1–11.

[39] Begum Erdogan et al. "Cancer-associated fibroblasts promote directional cancer cell migration by aligning fibronectin". In: *Journal of Cell Biology* 216.11 (2017), pp. 3799–3816.

[40] Jacques Ferlay et al. "Cancer statistics for the year 2020: An overview". In: *International journal of cancer* 149.4 (2021), pp. 778–789.

[41] Matthew J Footer et al. "Direct measurement of force generation by actin filament polymerization using an optical trap". In: *Proceedings of the National Academy of Sciences* 104.7 (2007), pp. 2181–2186.

[42] Daan Frenkel and Berend Smit. *Understanding molecular simulation: from algorithms to applications.* Elsevier, 2023.

[43] Peter Friedl and Katarina Wolf. "Tumour-cell invasion and migration: diversity and escape mechanisms". In: *Nature reviews cancer* 3.5 (2003), pp. 362–374.

[44] Julie C Friedland, Mark H Lee, and David Boettiger. "Mechanically activated integrin switch controls $\alpha5\beta1$ function". In: *Science* 323.5914 (2009), pp. 642–644.

[45] Cedric Gaggioli et al. "Fibroblast-led collective invasion of carcinoma cells with differing roles for RhoGTPases in leading and following cells". In: *Nature cell biology* 9.12 (2007), pp. 1392–1400.

[46] Mu Gao et al. "Identifying unfolding intermediates of FN-III10 by steered molecular dynamics". In: *Journal of molecular biology* 323.5 (2002), pp. 939–950.

[47] Andrés J García, Jean E Schwarzbauer, and David Boettiger. "Distinct activation states of $\alpha5\beta1$ integrin show differential binding to RGD and synergy domains of fibronectin". In: *Biochemistry* 41.29 (2002), pp. 9063–9069.

[48] Christianne Gaudet et al. "Influence of type I collagen surface density on fibroblast spreading, motility, and contractility". In: *Biophysical journal* 85.5 (2003), pp. 3329–3335.

[49] Elaine PS Gee et al. "SLLISWD sequence in the 10FNIII domain initiates fibronectin fibrillogenesis". In: *Journal of Biological Chemistry* 288.29 (2013), pp. 21329–21340.

[50] Benjamin Geiger, Joachim P Spatz, and Alexander D Bershadsky. "Environmental sensing through focal adhesions". In: *Nature reviews Molecular cell biology* 10.1 (2009), pp. 21–33.

[51] Ze Gong et al. "Matching material and cellular timescales maximizes cell spreading on viscoelastic substrates". In: *Proceedings of the National Academy of Sciences* 115.12 (2018), E2686–E2695.

[52] Yifan Guo, Sarah Calve, and Adrian Buganza Tepole. "Multiscale mechanobiology: Coupling models of adhesion kinetics and nonlinear tissue mechanics". In: *Biophysical Journal* 121.4 (2022), pp. 525–539.

[53] Hellyeh Hamidi and Johanna Ivaska. "Every step of the way: integrins in cancer progression and metastasis". In: *Nature Reviews Cancer* 18.9 (2018), pp. 533–548.

[54] Nicholas J Hoff. "Approximate analysis of structures in the presence of moderately large creep deformations". In: *Quarterly of Applied Mathematics* 12.1 (1954), pp. 49–55.

[55] Elijah N Holland et al. "FAK, vinculin, and talin control mechanosensitive YAP nuclear localization". In: *Biomaterials* (2024), p. 122542.

[56] Andrew W Holle, Jennifer L Young, and Joachim P Spatz. "In vitro cancer cell–ECM interactions inform in vivo cancer treatment". In: *Advanced drug delivery reviews* 97 (2016), pp. 270–279.

[57] Jianbing Hou et al. "The roles of integrin $\alpha5\beta1$ in human cancer". In: *OncoTargets and therapy* (2020), pp. 13329–13344.

[58] Ping Hu and Bing-Hao Luo. "Integrin bi-directional signaling across the plasma membrane". In: *Journal of cellular physiology* 228.2 (2013), pp. 306–312.

[59] Paul E Hughes et al. "Breaking the Integrin Hinge: A DEFINED STRUCTURAL CONSTRAINT REGULATES INTEGRIN SIGNALING". In: *Journal of Biological Chemistry* 271.12 (1996), pp. 6571–6574.

[60] Jay D Humphrey, Eric R Dufresne, and Martin A Schwartz. "Mechanotransduction and extracellular matrix homeostasis". In: *Nature reviews Molecular cell biology* 15.12 (2014), pp. 802–812.

[61] William Humphrey, Andrew Dalke, and Klaus Schulten. "VMD – Visual Molecular Dynamics". In: *Journal of Molecular Graphics* 14 (1996), pp. 33–38.

[62] William Humphrey, Andrew Dalke, and Klaus Schulten. "VMD: visual molecular dynamics". In: *Journal of molecular graphics* 14.1 (1996), pp. 33–38.

[63] Richard O Hynes. "Integrins: bidirectional, allosteric signaling machines". In: *cell* 110.6 (2002), pp. 673–687.

[64] Donald E Ingber. "Mechanosensation through integrins: cells act locally but think globally". In: *Proceedings of the National Academy of Sciences* 100.4 (2003), pp. 1472–1474.

[65] Zeinab Jahed et al. "Kindlin is mechanosensitive: Force-induced conformational switch mediates cross-talk among integrins". In: *Biophysical journal* 116.6 (2019), pp. 1011–1024.

[66] Zeinab Jahed et al. "Mechanotransduction pathways linking the extracellular matrix to the nucleus". In: *International review of cell and molecular biology* 310 (2014), pp. 171–220.

[67] Yanru Ji, Ying Fang, and Jianhua Wu. "Tension enhances the binding affinity of $\beta 1$ integrin by clamping Talin tightly: an insight from steered molecular dynamics simulations". In: *Journal of Chemical Information and Modeling* 62.22 (2022), pp. 5688–5698.

[68] Myung Hyun Jo et al. "Single-molecule characterization of subtype-specific $\beta 1$ integrin mechanics". In: *Nature communications* 13.1 (2022), p. 7471.

[69] Carol Jurchenko et al. "Integrin-generated forces lead to streptavidin-biotin unbinding in cellular adhesions". In: *Biophysical journal* 106.7 (2014), pp. 1436–1446.

[70] Pakorn Kanchanawong and David A Calderwood. "Organization, dynamics and mechanoregulation of integrin-mediated cell–ECM adhesions". In: *Nature Reviews Molecular Cell Biology* 24.2 (2023), pp. 142–161.

[71] Jenny Z Kechagia, Johanna Ivaska, and Pere Roca-Cusachs. "Integrins as biomechanical sensors of the microenvironment". In: *Nature reviews Molecular cell biology* 20.8 (2019), pp. 457–473.

[72] Fang Kong et al. "Demonstration of catch bonds between an integrin and its ligand". In: *Journal of Cell Biology* 185.7 (2009), pp. 1275–1284.

[73] Martin Kulke and Walter Langel. "Molecular dynamics simulations to the bidirectional adhesion signaling pathway of integrin $\alpha V \beta 3$". In: *Proteins: Structure, Function, and Bioinformatics* 88.5 (2020), pp. 679–688.

[74] Melissa S Kurtis et al. "Integrin-mediated adhesion of human articular chondrocytes to cartilage". In: *Arthritis & Rheumatism* 48.1 (2003), pp. 110–118.

[75] Andrew R Leach. *Molecular modelling: principles and applications*. Pearson education, 2001.

[76] Junmin Lee et al. "Directing stem cell fate on hydrogel substrates by controlling cell geometry, matrix mechanics and adhesion ligand composition". In: *Biomaterials* 34.33 (2013), pp. 8140–8148.

[77] Mark H Lee et al. "Effect of biomaterial surface properties on fibronectin–$\alpha 5 \beta 1$ integrin interaction and cellular attachment". In: *Biomaterials* 27.9 (2006), pp. 1907–1916.

[78] Feiya Li et al. "Force measurements of the $\alpha 5 \beta 1$ integrin–fibronectin interaction". In: *Biophysical journal* 84.2 (2003), pp. 1252–1262.

[79] Jing Li, Jiabin Yan, and Timothy A Springer. "Low-affinity integrin states have faster ligand-binding kinetics than the high-affinity state". In: *Elife* 10 (2021), e73359.

[80] Na Li et al. "Comparison of Linear vs. Cyclic RGD Pentapeptide Interactions with Integrin $\alpha v \beta 3$ by molecular dynamics simulations". In: *Biology* 10.7 (2021), p. 688.

[81] Wenqiang Li et al. "Stress-relaxing double-network hydrogel for chondrogenic differentiation of stem cells". In: *Materials Science and Engineering: C* 107 (2020), p. 110333.

[82] Chang Liu et al. "Self-assembly of mesoscale collagen architectures and applications in 3D cell migration". In: *Acta Biomaterialia* 155 (2023), pp. 167–181.

[83] Gabriel R López-Marcial et al. "Agarose-based hydrogels as suitable bioprinting materials for tissue engineering". In: *ACS Biomaterials Science & Engineering* 4.10 (2018), pp. 3610–3616.

[84] Qing Luo et al. "Cell stiffness determined by atomic force microscopy and its correlation with cell motility". In: *Biochimica et Biophysica Acta (BBA)-General Subjects* 1860.9 (2016), pp. 1953–1960.

[85] Yufei Ma et al. "Viscoelastic cell microenvironment: hydrogel-based strategy for recapitulating dynamic ECM mechanics". In: *Advanced Functional Materials* 31.24 (2021), p. 2100848.

[86] Andrea Malandrino et al. "Dynamic filopodial forces induce accumulation, damage, and plastic remodeling of 3D extracellular matrices". In: *PLoS computational biology* 15.4 (2019), e1006684.

[87] Yong Mao and Jean E Schwarzbauer. "Fibronectin fibrillogenesis, a cell-mediated matrix assembly process". In: *Matrix biology* 24.6 (2005), pp. 389–399.

[88] Jonathan P McKinley et al. "Design of a flexing organ-chip to model in situ loading of the intervertebral disc". In: *Biomicrofluidics* 16.5 (2022), p. 054111.

[89] Mehrdad Mehrbod and Mohammad RK Mofrad. "Localized lipid packing of transmembrane domains impedes integrin clustering". In: *PLoS computational biology* 9.3 (2013), e1002948.

[90] Mehrdad Mehrbod, Stephen Trisno, and Mohammad RK Mofrad. "On the activation of integrin αIIbβ3: outside-in and inside-out pathways". In: *Biophysical journal* 105.6 (2013), pp. 1304–1315.

[91] Andre R. Montes et al. "Multiscale computational framework to investigate integrin mechanosensing and cell adhesion". In: *Journal of Applied Physics* 134.11 (Sept. 2023), p. 114702. ISSN: 0021-8979.

[92] Simon W Moore, Pere Roca-Cusachs, and Michael P Sheetz. "Stretchy proteins on stretchy substrates: the important elements of integrin-mediated rigidity sensing". In: *Developmental cell* 19.2 (2010), pp. 194–206.

[93] Paulina Moreno-Layseca et al. "Integrin trafficking in cells and tissues". In: *Nature cell biology* 21.2 (2019), pp. 122–132.

[94] Stefan Münster et al. "Strain history dependence of the nonlinear stress response of fibrin and collagen networks". In: *Proceedings of the National Academy of Sciences* 110.30 (2013), pp. 12197–12202.

[95] Masamichi Nagae et al. "Crystal structure of α5β1 integrin ectodomain: Atomic details of the fibronectin receptor". In: *Journal of Cell Biology* 197.1 (2012), pp. 131–140.

[96] Toshihiko Nagai et al. "Monoclonal antibody characterization of two distant sites required for function of the central cell-binding domain of fibronectin in cell adhesion, cell migration, and matrix assembly." In: *The Journal of cell biology* 114.6 (1991), pp. 1295–1305.

[97] Gabriel E Neurohr and Angelika Amon. "Relevance and regulation of cell density". In: *Trends in cell biology* 30.3 (2020), pp. 213–225.

[98] Ryan Y Nguyen et al. "Tunable Mesoscopic Collagen Island Architectures Modulate Stem Cell Behavior". In: *Advanced Materials* 35.16 (2023), p. 2207882.

[99] Naoyo Nishida et al. "Angiogenesis in cancer". In: *Vascular health and risk management* 2.3 (2006), pp. 213–219.

[100] Jason J Northey, Laralynne Przybyla, and Valerie M Weaver. "Tissue Force Programs Cell Fate and Tumor Aggression Mechanotransduction in Cell Fate and Cancer Aggression". In: *Cancer discovery* 7.11 (2017), pp. 1224–1237.

[101] Patrick W Oakes et al. "Lamellipodium is a myosin-independent mechanosensor". In: *Proceedings of the National Academy of Sciences* 115.11 (2018), pp. 2646–2651.

[102] Andres F Oberhauser et al. "The mechanical hierarchies of fibronectin observed with single-molecule AFM". In: *Journal of molecular biology* 319.2 (2002), pp. 433–447.

[103] Di Pan and Yuhua Song. "Role of altered sialylation of the I-like domain of $\beta 1$ integrin in the binding of fibronectin to $\beta 1$ integrin: thermodynamics and conformational analyses". In: *Biophysical journal* 99.1 (2010), pp. 208–217.

[104] Roumen Pankov et al. "Integrin dynamics and matrix assembly: tensin-dependent translocation of $\alpha 5 \beta 1$ integrins promotes early fibronectin fibrillogenesis". In: *The Journal of cell biology* 148.5 (2000), pp. 1075–1090.

[105] Matthew J Paszek et al. "Integrin clustering is driven by mechanical resistance from the glycocalyx and the substrate". In: *PLoS computational biology* 5.12 (2009), e1000604.

[106] Matthew J Paszek et al. "Tensional homeostasis and the malignant phenotype". In: *Cancer cell* 8.3 (2005), pp. 241–254.

[107] Eileen Puklin-Faucher and Michael P Sheetz. "The mechanical integrin cycle". In: *Journal of cell science* 122.2 (2009), pp. 179–186.

[108] Sambra D Redick et al. "Defining fibronectin's cell adhesion synergy site by site-directed mutagenesis". In: *The Journal of cell biology* 149.2 (2000), pp. 521–527.

[109] Pere Roca-Cusachs, Thomas Iskratsch, and Michael P Sheetz. "Finding the weakest link–exploring integrin-mediated mechanical molecular pathways". In: *Journal of cell science* 125.13 (2012), pp. 3025–3038.

[110] Tyler D Ross et al. "Integrins in mechanotransduction". In: *Current opinion in cell biology* 25.5 (2013), pp. 613–618.

[111] Pasquale Sacco et al. "Regulation of Substrate Dissipation via Tunable Linear Elasticity Controls Cell Activity". In: *Advanced Functional Materials* 32.29 (2022), p. 2200309.

[112] Florence Schaffner, Anne Marie Ray, and Monique Dontenwill. "Integrin $\alpha 5 \beta 1$, the fibronectin receptor, as a pertinent therapeutic target in solid tumors". In: *Cancers* 5.1 (2013), pp. 27–47.

[113] David A Scheiblin et al. "Beta-1 integrin is important for the structural maintenance and homeostasis of differentiating fiber cells". In: *The international journal of biochemistry & cell biology* 50 (2014), pp. 132–145.

[114] Nicolas Schierbaum, Johannes Rheinlaender, and Tilman E Schäffer. "Combined atomic force microscopy (AFM) and traction force microscopy (TFM) reveals a correlation between viscoelastic material properties and contractile prestress of living cells". In: *Soft Matter* 15.8 (2019), pp. 1721–1729.

[115] LLC Schrödinger. "The PyMOL Molecular Graphics System, Version 1.8". 2015.

[116] Stephanie Schumacher et al. "Structural insights into integrin $\alpha 5 \beta 1$ opening by fibronectin ligand". In: *Science Advances* 7.19 (2021), eabe9716.

[117] Sanford J Shattil, Chungho Kim, and Mark H Ginsberg. "The final steps of integrin activation: the end game". In: *Nature reviews Molecular cell biology* 11.4 (2010), pp. 288–300.

[118] David E Shaw et al. "Anton 3: twenty microseconds of molecular dynamics simulation before lunch". In: *Proceedings of the International Conference for High Performance Computing, Networking, Storage and Analysis*. 2021, pp. 1–11.

[119] Adrian C Shieh. "Biomechanical forces shape the tumor microenvironment". In: *Annals of biomedical engineering* 39 (2011), pp. 1379–1389.

[120] RJ Slack et al. "Emerging therapeutic opportunities for integrin inhibitors". In: *Nature Reviews Drug Discovery* 21.1 (2022), pp. 60–78.

[121] Alexandra Sontheimer-Phelps, Bryan A Hassell, and Donald E Ingber. "Modelling cancer in microfluidic human organs-on-chips". In: *Nature Reviews Cancer* 19.2 (2019), pp. 65–81.

[122] Nico Strohmeyer et al. "Fibronectin-bound $\alpha 5 \beta 1$ integrins sense load and signal to reinforce adhesion in less than a second". In: *Nature Materials* 16.12 (2017), pp. 1262–1270.

[123] Shuixiu Su et al. "Force-enhanced biophysical connectivity of platelet $\beta 3$ integrin signaling through Talin is predicted by steered molecular dynamics simulations". In: *Scientific reports* 12.1 (2022), p. 4605.

[124] Subra Suresh. "Biomechanics and biophysics of cancer cells". In: *Acta biomaterialia* 3.4 (2007), pp. 413–438.

[125] Yoshikazu Takada, Xiaojing Ye, and Scott Simon. "The integrins". In: *Genome biology* 8 (2007), pp. 1–9.

[126] Junichi Takagi et al. "Global conformational rearrangements in integrin extracellular domains in outside-in and inside-out signaling". In: *Cell* 110.5 (2002), pp. 599–611.

[127] Junichi Takagi et al. "Structure of integrin $\alpha 5 \beta 1$ in complex with fibronectin". In: *The EMBO journal* (2003).

[128] Steven J Tan et al. "Regulation and dynamics of force transmission at individual cell-matrix adhesion bonds". In: *Science Advances* 6.20 (2020), eaax0317.

[129] Wenhui Tang et al. "Collective curvature sensing and fluidity in three-dimensional multicellular systems". In: *Nature Physics* 18.11 (2022), pp. 1371–1378.

[130] Dudu Tong et al. "Integrin αIIb$\beta 3$ intermediates: From molecular dynamics to adhesion assembly". In: *Biophysical Journal* 122.3 (2023), pp. 533–543.

[131] Andreea Trache et al. "Histamine effects on endothelial cell fibronectin interaction studied by atomic force microscopy". In: *Biophysical journal* 89.4 (2005), pp. 2888–2898.

[132] LRG Treloar. "The elasticity and related properties of rubbers". In: *Reports on progress in physics* 36.7 (1973), p. 755.

[133] Shingo Tsukamoto et al. "Intranuclear strain in living cells subjected to substrate stretching: A combined experimental and computational study". In: *Journal of Biomechanics* 119 (2021), p. 110292.

[134] Dimitrios Vavylonis, Qingbo Yang, and Ben O'Shaughnessy. "Actin polymerization kinetics, cap structure, and fluctuations". In: *Proceedings of the National Academy of Sciences* 102.24 (2005), pp. 8543–8548.

[135] Ning Wang, Jessica D Tytell, and Donald E Ingber. "Mechanotransduction at a distance: mechanically coupling the extracellular matrix with the nucleus". In: *Nature reviews Molecular cell biology* 10.1 (2009), pp. 75–82.

[136] Shuoshuo Wang et al. "Mechanotransduction via the LINC complex regulates DNA replication in myonuclei". In: *Journal of Cell Biology* 217.6 (2018), pp. 2005–2018.

[137] Xuefeng Wang and Taekjip Ha. "Defining single molecular forces required to activate integrin and notch signaling". In: *Science* 340.6135 (2013), pp. 991–994.

[138] Benjamin Webb and Andrej Sali. "Comparative protein structure modeling using MODELLER". In: *Current protocols in bioinformatics* 54.1 (2016), pp. 5–6.

[139] Iwona Wierzbicka-Patynowski and Jean E Schwarzbauer. "The ins and outs of fibronectin matrix assembly". In: *Journal of cell science* 116.16 (2003), pp. 3269–3276.

[140] Xin Wu et al. "Cardiomyocyte contractile status is associated with differences in fibronectin and integrin interactions". In: *American Journal of Physiology-Heart and Circulatory Physiology* 298.6 (2010), H2071–H2081.

[141] Jennifer L Young et al. "Integrin subtypes and nanoscale ligand presentation influence drug sensitivity in cancer cells". In: *Nano Letters* 20.2 (2020), pp. 1183–1191.

[142] Zuoying Yuan et al. "Catch bond-inspired hydrogels with repeatable and loading rate-sensitive specific adhesion". In: *Bioactive Materials* 21 (2023), pp. 566–575.

[143] Xiaowei Zeng and Shaofan Li. "Multiscale modeling and simulation of soft adhesion and contact of stem cells". In: *Journal of the mechanical behavior of biomedical materials* 4.2 (2011), pp. 180–189.

[144] Wei Zhang et al. "Curved adhesions mediate cell attachment to soft matrix fibres in three dimensions". In: *Nature Cell Biology* 25.10 (2023), pp. 1453–1464.

[145] Xue-Ke Zhao et al. "Focal adhesion kinase regulates fibroblast migration via integrin beta-1 and plays a central role in fibrosis". In: *Scientific reports* 6.1 (2016), p. 19276.

[146] Dennis W Zhou et al. "Force-FAK signaling coupling at individual focal adhesions coordinates mechanosensing and microtissue repair". In: *Nature communications* 12.1 (2021), p. 2359.

[147] Jieqing Zhu et al. "Requirement of α and β subunit transmembrane helix separation for integrin outside-in signaling". In: *Blood, The Journal of the American Society of Hematology* 110.7 (2007), pp. 2475–2483.